The effect of dynamic operation and incoming flow on the wake of a utility-scale wind turbine

A DISSERTATION
SUBMITTED TO THE FACULTY OF THE GRADUATE SCHOOL
OF THE UNIVERSITY OF MINNESOTA
BY

Aliza Opila Abraham

IN PARTIAL FULFILLMENT OF THE REQUIREMENTS
FOR THE DEGREE OF
Doctor of Philosophy

Jiarong Hong

July, 2021

Acknowledgements

First I would like to thank my advisor, Professor Jiarong Hong, for his guidance throughout my PhD. His vision and investment in our work motivated me to aim high and accomplish my goals, instilling in me the confidence to ask difficult questions and push to find the answers.

I am indebted to the National Science Foundation, IonE of the University of Minnesota, Xcel Energy, and the Doctoral Dissertation Fellowship for providing funding for my PhD work. This project would not have been possible without their support.

I would also like to thank my lab mates for providing feedback and support during every stage of my research. In the experience of pursuing a PhD, nothing can replace the understanding of people who know exactly what you're going through.

I had the privilege of meeting many excellent people during my time at NREL. I sincerely appreciate their excitement about my work and their enthusiasm about wind energy research. We had highly fruitful collaborations, and I look forward to continuing to work with them in the future.

Thank you to my friends who reminded me that there is life outside of research. The trivia nights, boat days, murder mystery parties, escape rooms, brewery visits, game nights, and more kept me sane, especially during the pandemic.

I am grateful to my family and their constant support. My parents instilled in me a strong sense of scientific curiosity, and have always encouraged me to follow my passion. Elana and Joel are continuous sources of inspiration and steadfast friends, always eager to talk about whatever is going on in our lives.

Finally, I want to express my gratitude to Grace, who believed in me every step of the way. Thanks for being along for the ride.

Abstract

Wind turbine wakes, the regions of slower and more turbulent air behind turbines, lead to power losses up to 40% and increased structural loading on downwind turbines within a wind farm. To mitigate these detrimental effects, improved understanding of wake behavior is required. However, modeling wind turbine flows in the laboratory or in simulations is hindered by the wide range of relevant scales and the complexity of atmospheric flow and turbine operation. Because of these limitations, field scale studies are essential. Conventional field scale flow measurement techniques such as lidar and anemometers have limited spatio-temporal resolution, inhibiting their ability to capture the highly dynamic and heterogeneous behaviors characteristic of wind turbine wakes. To address these shortcomings, super-large-scale flow imaging with natural snowfall is used to analyze the flow in the wake of utility-scale wind turbine.

The current work focuses on the impact of constantly-changing atmospheric conditions and dynamic turbine operation on the near wake, the region within four rotor diameters downstream of the turbine. The flow in this region significantly impacts wake development downstream, including meandering, mixing, and recovery. The current research investigates the effect of coherent vortical structures in the inflow, the impact of the turbine nacelle and support tower on the near wake, dynamic wake modulation, and the interaction between the wake and the ground surface. Dynamic wake modulation, the large-scale motion of the wake in response to changes in incoming flow and turbine operation, is shown to substantially enhance mixing between the wake and the surrounding flow.

The findings of this research have important implications for wind farm design, layout, and controls. New understanding of wind turbine wake behaviors can be incorporated into simplified models used to optimize wind farms and evaluate their impacts on their surroundings. Improving the accuracy of these models can increase efficiency and reduce power production uncertainty. Additionally, advanced control algorithms to minimize wake losses can be designed based on the presented relationships between turbine operational parameters readily available to the controller and wake behaviors.

These direct connections pave the way for more precise wake prediction and control under real operating conditions.

Contents

List of Tables

List of Figures

Chapter 1

Introduction

1.1 Motivation

Wind energy installation has experienced rapid growth in recent years and continued growth is expected, with demand and deployment projected to increase tenfold by the year 2050 [8]. To facilitate such growth, the levelized cost of wind energy must continue to decrease, requiring additional improvements in wind farm efficiency. Currently, one of the primary sources of energy losses within a wind farm is wakes, with maximum recorded wake losses reaching 40% [9]. As turbines extract energy from the wind, they leave slower, more turbulent air behind them, i.e., wakes. When these wakes impinge on downstream turbines within the farm, less energy is available in the wind for power production. Furthermore, the additional turbulence in the wake leads to increased fatigue loading on the downstream turbines, causing premature structural failure [10, 11]. To mitigate these detrimental wake effects, improved understanding of utility-scale wind turbine wake behaviors is required.

1.2 Modelling challenges

As utility-scale wind turbines are some of the largest dynamic structures in the world, investigation into their interactions with atmospheric flow pose several unique challenges. First, utility-scale turbines typically extend over 100 m tall, making them difficult to model in laboratory scale wind tunnels, which typically have cross-sections of only a few

meters. This discrepancy in scales prevents the accurate reproduction of all relevant dimensionless parameters such as the Reynolds number and tip speed ratio in laboratory experiments [12]. In addition to their large maximum dimension, the minimum relevant wind turbine scale (i.e., the thickness of the blade) is a few centimeters, several orders of magnitude smaller than the turbine height. This wide range of scales makes computational fluid dynamics simulations of fully-resolved wind turbines prohibitively expensive. Instead, simulations must use simplifications and assumptions that sacrifice the accurate reproduction of real-world phenomena [13].

Utility-scale wind turbines also operate in a complex atmospheric environment. Driven by the Coriolis force caused by Earth's rotation and temperature changes across the land surface, atmospheric flow is highly dynamic, changing seasonally and diurnally. Furthermore, local topography and obstructions such as trees and buildings influence wind behavior. These interacting factors lead to wind turbine inflow conditions that are constantly changing over a wide range of timescales. Accurately modelling such flow is an ongoing area of research, and considered one of the grand challenges in wind energy science [8].

Finally, wind turbines are highly dynamic structures that interact with the wind both passively and actively. As larger and larger turbines are designed and built, the structural components become lighter and more flexible, subjecting the turbine to constant passive aeroelastic deformation. On the active side, the rotor spins at varying speeds, the blade pitch angle changes, and the rotor yaws to face the wind. Significantly, the turbine implements these operational changes in response to the dynamic wind conditions discussed above, resulting in complex interactions between the flow and the turbine structure. Operational changes are dictated by the turbine controller, which can be simulated computationally [14], but is typically not included in laboratory scale models.

1.3 Existing field-scale methods

Because of these substantial modelling limitations, field-scale studies of wind turbine flows are essential. The two most commonly used field-scale flow measurement tools are lidar and anemometers. Lidar (Doppler wind light detection and ranging) uses

a laser beam to measure wind speed. The light from the laser scatters off particles in the atmosphere, and the Doppler shift is used to calculate the velocity component parallel to the laser beam. To obtain two- or three-dimensional velocity fields using a single lidar, the beam can be scanned over an area. However, this method assumes the velocity stays constant during the scanning time, which is not the case for flows around wind turbines [15]. Arrays of anemometers are also used to probe the atmospheric flow. Sonic anemometers in particular can measure high temporal resolutions (e.g., 50 Hz [16]), but their spatial resolution is limited as they only measure single points. These limitations in spatio-temporal resolution impede the measurement of highly dynamic and heterogeneous atmospheric and utility-scale turbine wake flow.

1.4 Super-large-scale particle image velocimetry

To address these limitations, Hong et al. [17] introduced a flow field visualization and quantification technique using natural snowflakes as flow tracers, termed super-large-scale particle image velocimetry (SLPIV). SLPIV is capable of measuring atmospheric and wind turbine wake flows at high spatio-temporal resolution, as first demonstrated with a 36 m $\times$ 36 m area in the near wake of a 2.5 MW wind turbine [17]. Since then it has been applied to the discovery of novel wind turbine wake behaviors [18, 5], atmospheric boundary layer measurements [4, 19], snow settling behavior characterization [20, 21]. In particular, Dasari et al. [5] extended the technique to span the entire height of the wake, on the order of 100 m. This study revealed multiple previously unobserved wind turbine wake phenomena, including intermittent periods of wake contraction caused by interactions between the turbine and its own wake in response to changes in blade pitch.

1.5 Thesis objectives and overview

The focus of the current research is to characterize the effect of dynamic turbine operation and inflow on the wake of a utility-scale wind turbine. The majority of the work will discuss the near wake of the turbine, i.e., the region within four rotor diameters of the turbine [22, 23]. This region is dominated by coherent flow structures shed

from the turbine, particularly the vortices shed from the tips of the blades, and the results of the interaction between the turbine and the inflow can be observed clearly here. Farther downstream, interactions with the flow around the wake complicates the direct observation of these phenomena. Significantly, near wake behavior impacts wake development downstream, as tip vortex behavior affects wake breakdown and recovery [24] and interactions between coherent structures influence large-scale wake meandering [25].

First, an overview of the methodology, including the field measurement site and SLPIV technique, is presented in Chapter 2. In Chapter 3, coherent vortical structures in the atmosphere are characterized and their impact on the turbine and wake is evaluated. In Chapter 4, the impact of the support tower and nacelle (housing for the gearbox and controller that connects the rotor to the tower) on the wake is discussed. The next four chapters pertain to dynamic wake modulation, or the active modulation of the wake flow by changes in turbine operation and inflow conditions. This phenomenon is introduced in Chapter 5 and investigated in more detail in Chapter 6. Its propagation downstream is explored in Chapter 7, and its incorporation into wind farm power prediction models is discussed in Chapter 8. Interactions between the wake and the ground surface are discussed in Chapter 9. Finally, Chapter 10 provides conclusions and some additional discussion about the presented research.

Chapter 2

Methodology

2.1 Eolos site

All field experiments were conducted at the University of Minnesota Eolos Wind Energy Research Field Station in Rosemount, Minnesota. As shown in figure 2.1(a), the site consists of a fully instrumented 2.5 MW Clipper Liberty C96 wind turbine and a 130 m meteorological tower (met tower). The turbine is a three-bladed, horizontal-axis, pitch-regulated, variable speed machine with a 96 m rotor diameter (D) mounted atop an 80 m support tower. The turbine tower has a cylindrical cross section with a constant diameter of 4.1 m up to a height of 26 m and a conical cross section above, tapering gradually to a diameter of 3 m at 78 m elevation. The nacelle of the turbine is near cuboidal in shape with dimensions of 5.3 m $\times$ 4.7 m $\times$ 5.5 m. The supervisory control and data acquisition (SCADA) system located on the nacelle records incoming wind speed and direction at a frequency of 1 Hz and hub speed, blade pitch, power generated, and rotor direction at 20 Hz. Strain gauges and accelerometers are installed along each blade and strain gauges are mounted around the base of the tower to record the turbine structural response at 20 Hz. The met tower, located 170 m south of the turbine (as the predominant wind direction is from the south) is designed to characterize the atmospheric conditions at the Eolos site. It consists of wind speed, wind direction, temperature, and humidity sensors at several elevations ranging from 7 m to 129 m (figure 2.1b). Four of these elevations (10 m, 30 m, 80m, and 129 m, corresponding to the standard atmospheric measurement height, bottom blade tip, turbine hub height, and top blade

tip, respectively) are instrumented with high resolution Campbell Scientific CSAT3 3D sonic anemometers with a sampling rate of 20 Hz. Cup and vane anemometers and temperature and relative humidity sensors located at 7 m, 27 m, 55 m, 77 m, 105 m, and 126 m record at 1 Hz. All data recorded at the Eolos site is sampled continuously 24 hours a day and stored on backed up servers. Detailed information about the Eolos facility is provided in the supplemental material for Hong et al. [17].

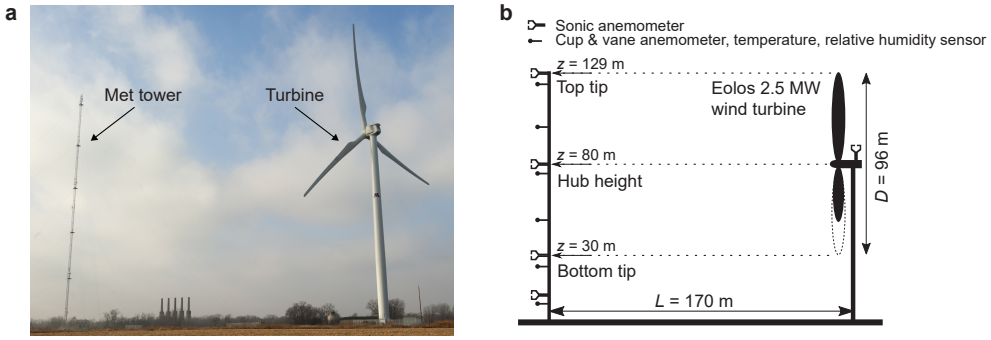

Figure 2.1: (a) Photograph of the Eolos field site with the met tower and turbine labeled in the image. (b) Schematic of the met tower and turbine. The met tower has sonic anemometers at 10 m, 30 m, 80 m, and 129 m. There are cup and vane anemometers, temperature sensors, and relative humidity sensors at 7 m, 27 m, 52 m, 77 m, 102 m, and 126 m.

2.2 Flow visualization using natural snowfall

The flow visualization technique using natural snowfall and super-large-scale particle image velocimetry (SLPIV) were first employed by Hong et al. [17] to investigate the near-wake of the Eolos turbine with a field of view (FOV) of $\sim$ 36 m $\times$ 36 m. They have since been extended to much larger FOVs on the order of 100 m to capture the full wake of the turbine (e.g., [5, 26]). The SLPIV technique is based on conventional particle image velocimetry (PIV), which tracks the displacement of tracer particles within an illuminated flow field at high spatio-temporal resolution relative to other conventional flow measurement techniques [27, 28]. PIV is typically applied to relatively small FOVs (a few square meters) due to the difficulty of seeding large flow fields with uniformly distributed tracers. To overcome this challenge, natural snowflakes are used

as environmentally benign flow tracers to characterize atmospheric flows. SLPIV data is collected during snowstorms that occur at night to provide contrast between the illuminated snowflakes and the dark background.

The setup for the snow-powered flow visualization experiments is comprised of an optical assembly to illuminate the snowflakes and two cameras to capture videos of the snowflake motion. The optical assembly includes a 5 kW highly collimated search light with a 300 mm beam diameter and a curved mirror to project the beam into a light sheet (figure 2.2). The expansion angle of the light sheet can be adjusted by changing the curvature of the mirror, and the light sheet can be directed vertically or horizontally, depending on the desired FOV. The illumination system is mounted on a trailer, allowing it to be positioned in different locations relative to the turbine and aligned with the wind direction. Two cameras record the motion of the snowflakes within the light sheet from different locations and angles to capture different FOVs. The Sony-A7RII camera can capture 4K-resolution videos at 30 Hz, and is typically used to record a smaller FOV at higher resolution. The Nikon D600 camera captures HD videos at 30 Hz, and is used to record the larger FOV (see sample snowflake image in figure 2.3a).

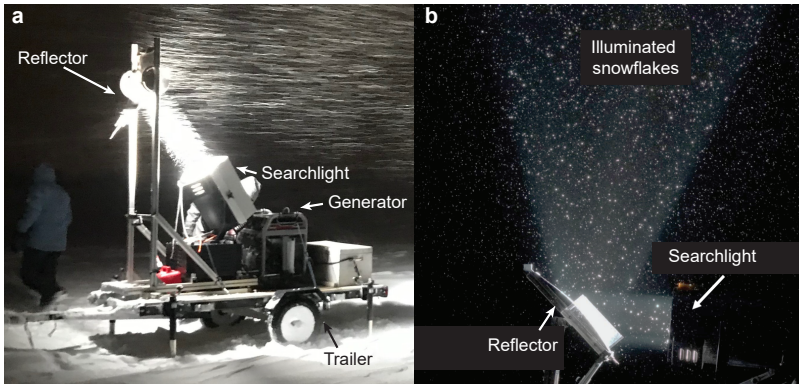

Figure 2.2: (a) Photograph of the optical assembly, including the generator to power the search light, the curved reflector, the search light, and the trailer. The horizontal light sheet orientation is shown here. (b) Image showing snowflakes illuminated by the light sheet. The vertical light sheet orientation is shown here.

Though data processing techniques differ slightly for each dataset, some common procedures are used, discussed herewith. First, as the cameras are mounted on tripods placed on the ground and the center of the FOV is typically $\sim$ 50 m in elevation,

significant camera tilt angles are required to capture the full FOV. These tilt angles induce some distortion in the images. To correct for this image distortion, the method described by Toloui et al. [4] is employed. The local magnification is calculated using the thin lens equation, $M(i,j) = 1/[L(i,j)/f - 1]$, where $M(i,j)$ is the magnification at point (i,j) in the image, $L(i,j)$ is the distance between the lens and (i,j), and f is the focal length of the lens. This equation provides the resolution for each pixel, which can then be used to generate undistorted (de-warped) images (figure 2.3b). These images are then enhanced by calculating the mean intensity of the video, then subtracting this background from all images, thereby increasing the contrast (figure 2.3c).

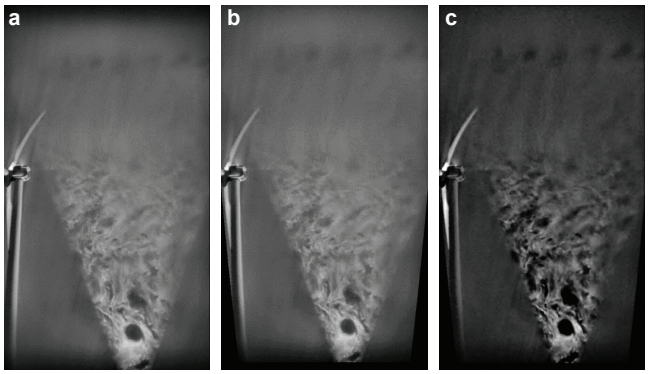

Figure 2.3: Sample snowflake image capturing the whole vertical extent of the wind turbine near wake, including (a) the raw image, (b) the de-warped image, and (c) the image after the background is subtracted.

To capture the full extent of the turbine wake ($\sim$ 100 m), the FOV is extended beyond that used by Hong et al. [17]. For such a large FOV, individual snowflakes cannot be resolved, even in the enhanced images. Therefore, the correlation between large-scale snow patterns in adjacent video frames are used to provide the correlation signal for SLPIV, rather than individual particles as in traditional PIV (first implemented by Dasari et al. [5]). These snow patterns result from the preferential concentration of the snowflakes in a turbulent flow field due to the inertia of the particles and variations in strain rate and vorticity in the flow. This preferential concentration phenomenon also reveals coherent vortical structures in the flow. These vortices appear as voids in the images, as the rotation of the flow expels snowflakes from the center of the vortex, leaving a region of lower concentration in the center. Some of these voids, indicating

vortices shed from the turbine tower and blades, are visible in figure 2.3.

Chapter 3

Characterization of atmospheric coherent structures and their impact on a utility-scale wind turbine

The content of this chapter is under review for publication by the author in *Flow*.

3.1 Introduction

Wind turbines operate in a complex atmospheric environment subject to constantly changing turbulent wind conditions that are influenced by a broad range of scales [8]. Previous works have established the significant impacts of atmospheric turbulence on wind turbines, showing that higher levels of turbulence lead to increased structural loading [29, 30] and accelerated breakdown of the wake, the region of slower air behind the turbine [31, 32]. Moreover, turbulent wind speed fluctuations lead to power production deviations from the expected power curve, contributing to uncertainty in wind farm energy production and increased financial risk for energy contractors [9]. However, the impact of atmospheric coherent structures, characteristic features of turbulence, has not been thoroughly explored.

Coherent structures in the atmospheric boundary layer (ABL) have been observed to exhibit similar properties to those of canonical turbulent boundary layers observed in laboratory experiments. In particular, signatures of hairpin vortex packets have been consistently identified in the ABL within $\sim 10 - 20$ m elevations [33, 34, 35, 19]. These structures are more difficult to detect at higher elevations where they could interact with wind turbines due to limitations in the spatial resolution of conventional measurement techniques such as sonic anemometers. However, some recent studies have used lidar to detect intermittent coherent structures at elevations up to 200 m. Träumner, et al. [36] observed large-scale coherent regions of velocity, or "streaks", with 100-200 m vertical extent that are interpreted as indicators of groups of hairpin vortices, with insufficient resolution to detect individual vortex cores. By qualitatively classifying hourly intervals as "with structures" or "homogeneous", they determined that the mean wind speed is higher for periods with structures than for homogeneous periods (4.5-6.3 m/s vs. 2.2-3.8 m/s, respectively). Cheliotis et al. [37] identified similar velocity streaks in lidar data at an elevation of 75 m. Using an automated classification method, they detected coherent streaks on 25% of the lidar scans over a period of 2 months. These streaks were found to occur more frequently at night than during the day. Alcayaga et al. [38] directly quantified the vertical component of vorticity from lidar scans taken at 200 m of elevation and found that positive-divergence streaks (indicative of vertical ejections of low-momentum flow) are bounded by counter-rotating vortices. These features are characteristic of canonical hairpin vortex packets found in turbulent boundary layers at a wide range of Reynolds numbers, which have been shown to extend beyond the logarithmic layer even up to the edge of the boundary layer [39].

Very few works have investigated the impact of coherent structures on wind turbines. One such study simulated a Kelvin Helmholtz billow, which generates coherent structures in the atmosphere, interacting with a wind turbine. Using large eddy simulations supplemented with a short example from field data, they found that coherent structures cause high frequency structural vibrations and strong impulsive loading events, both of which can lead to structural damage [40]. A more recent investigation used cylinders of different sizes to generate turbulence upstream of a hydrokinetic turbine in open-channel flow. This study showed that cylinders placed farther upstream cause the turbine wake to breakdown faster than those placed closer to the turbine, because the

upstream placement allows longer time for coherent structures to develop. In addition, the slope of the turbine power spectrum is steeper when in the wake of a cylinder in the same intermediate frequency range that scales with the cylinder diameter and flow speed due to von Kármán vortex shedding [41]. Though these studies provide important insights into the interactions between wind turbines and coherent structures, they were not conducted under an extended period of real atmospheric conditions.

Previous works have had limited success directly characterizing atmospheric coherent structures over a range of scales and determining their impact on wind turbines due to limitations in spatio-temporal resolution. Of the studies discussed above, only Alcayaga et al. [38] directly identified individual vortices at high enough elevations to interact with wind turbines, and even they were constrained by their use of scanning lidar, which requires 45 seconds to obtain a full scan of the measurement region [42]. On the other hand, several field-scale investigations have explored the interaction between wind turbines and different ranges of atmospheric turbulent length scales. Chamorro et al. [43] conducted a field study using a meteorological tower to characterize the inflow experienced by the 2.5 MW wind turbine at the Eolos Wind Energy Research Station, and investigated the modulation of power generation and foundation strain. They identified three frequency regions that influence power and strain differently: subrotor length scales have no effect on power but directly influence strain, power and strain both exhibit a damped response to intermediate length scales, and the largest length scales (on the order of the boundary layer thickness) directly influence strain and power. Heisel, Hong, and Guala [44] quantified the modulation of turbulent length scales between the inflow, probed using a meteorological tower, and the wake, measured with lidar. They observed a reduction of low-frequency energy and an increase in high-frequency energy in the wake relative to the inflow, suggesting a breakdown of large turbulent scales into smaller scales. This sheltering effect is only observed when the turbine is operating in the optimal regime. Both aforementioned studies use frequency spectra to analyse the turbulent flow scales, but they do not directly detect coherent structures. However, frequency spectra do not fully capture the complexity of the ABL, including the coherent structures discussed above.

To summarize, direct characterization of atmospheric coherent structures has been hindered by the low spatio-temporal resolution of conventional field-scale measurement

techniques. Furthermore, investigations into the impact of such structures on wind turbines have been limited to the laboratory and simulations where the stochasticity of atmospheric flow is difficult to replicate. Therefore, the goal of the current investigation is to 1) provide a more detailed characterization of atmospheric coherent structures, including their intermittency and stochasticity, and 2) quantify the impact of these structures on utility-scale wind turbine loading, power generation, and wake behaviour under real atmospheric conditions. These aims are achieved using snow-powered super-large-scale particle image velocimetry, a high-resolution field scale measurement technique that has proven successful in quantifying flows (including coherent vortical structures) around utility-scale wind turbines [26]. Previous studies have used this method to characterize the incoming flow approaching the 2.5 MW turbine at the Eolos site [45] and to identify previously unobserved wake behaviours including wake contraction in response to changing turbine blade pitch [5]. This technique has also been used to characterize the ABL flow at the Eolos site [4] and to provide insight into the structure of very high Reynolds number turbulent boundary layers [19]. In the current study, we extend this technique to identify coherent structures in the inflow and to quantify the turbine and wake response.

3.2 Methodology

3.2.1 Experimental setup

In addition to the data collected by the turbine (section 2.1), flow visualization data is recorded using super-large-scale particle image velocimetry (SLPIV), with natural snowflakes serving as flow tracers [26]. A collimated searchlight is projected into a sheet to illuminate the snowflakes in the field of view (FOV), which spans the inflow and near wake of the turbine (figure 3.1*a*). A Nikon D600 camera, fitted with a 50 mm f/1.2 lens, is used to record videos of the snowflake motion at 30 Hz. Three flow visualization datasets were recorded during snowstorms that occurred during the hours of darkness, one on April 9, 2018, and two on February 24, 2019 two hours apart (figure 3.1*b*). The conditions of each dataset vary in mean wind speed at hub height (U_∞), region of turbine operation, and atmospheric conditions (table 3.1). The atmospheric stability of each dataset is quantified using the Bulk Richardson Number, $R_B = \frac{g\Delta\overline{\theta_v}\Delta z}{\overline{\theta_v}\left[(\Delta\overline{U})^2+(\Delta\overline{V})^2\right]}$,

where g is gravitational acceleration, θ_v is the virtual potential temperature, z is the elevation, U is the northerly wind component, and V is the westerly wind component [46]. All parameters are calculated using the cup and vane anemometers at the 126 m and 7 m elevations of the met tower. We also calculate the Monin-Obukhov length for each dataset as $L_{OB} = -U_\tau^3 \overline{\theta_v} / \kappa g \overline{w'\theta_v'}$, where U_τ is the friction velocity, κ is the von Kármán constant, and $\overline{w'\theta_v'}$ is the vertical heat flux calculated using temperature and vertical wind speed fluctuations from the 10 m sonic anemometer on the met tower. The friction velocity is estimated using the Reynolds stresses [46], as follows: $U_\tau = \left(\overline{u'w'}^2 + \overline{v'w'}^2\right)^{1/4}$, where u', v', and w' are the fluctuating streamwise, spanwise, and vertical velocity components, respectively, also measured at the 10 m sonic anemometer. The ABL during both Feb 2019 datasets can be considered neutral, as R_B is less than the critical value of 0.25 but greater than 0, and $z/L_{OB} << 0.1$. The Apr 2018 dataset is slightly stable. The ABL is typically near-neutral during snow storms, but the snow was relatively weak on the night the Apr 2018 data was collected, leading to a shift towards the more stable night-time stratification. Though capturing approximately the same area, the dimensions of the FOVs ($H_{\text{FOV}} \times W_{\text{FOV}}$) for each dataset vary slightly as well. The Apr 2018 dataset is slightly shorter than the other two, though the turbine is producing power for a substantially lower percentage of the time. Therefore, this dataset is primarily used for inflow characterization and contributes very little to the analysis of coherent structure impact on turbine operation.

Table 3.1: Parameters for each of the three datasets included in the current study.

	Apr 2018	Feb 2019a	Feb 2019b
U_∞ (m/s)	2.6	7.0	11.4
Region of turbine operation	1-1.5	1.5-2	2.5-3
R_B	0.45	0.12	0.04
L_{OB} (m)	35	1550	-2260
U_τ (m/s)	0.07	0.41	0.73
$H_{\text{FOV}} \times W_{\text{FOV}}$ (m $\times$ m)	87×49	105×59	93×52
Duration	18 min 30 sec	20 min	20 min
Percentage of time turbine is producing power	3%	100%	100%

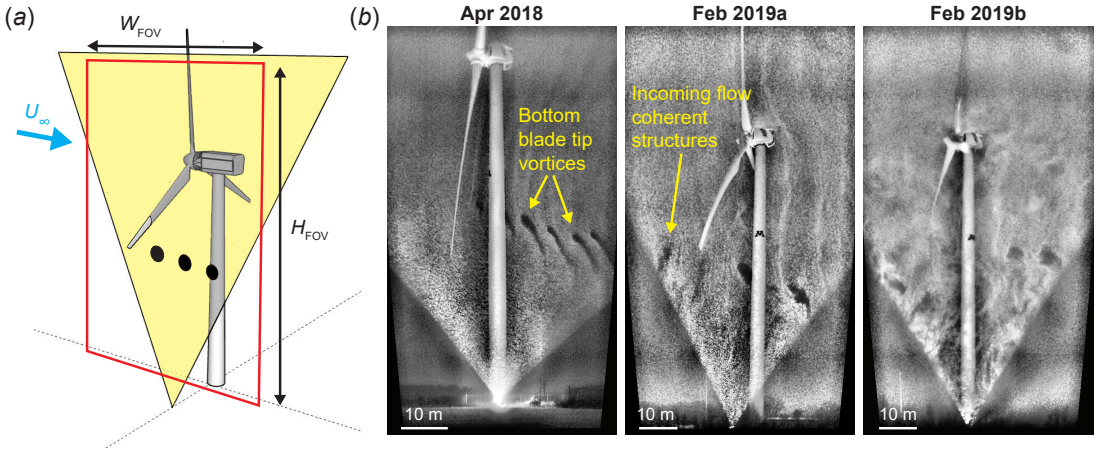

Figure 3.1: (a) Schematic showing the flow visualization FOV for the experiments. (b) Sample enhanced and de-warped flow visualization images for each of the three datasets. Arrows indicate vortices shed from the bottom blade tips in the near wake and coherent structures in the inflow, both seen as voids in the snow images.

3.2.2 Inflow coherent structure identification

In the flow visualization images, regions of strong vorticity are visible as dark voids where the snowflake concentration is significantly reduced (see figure 3.1a). These voids are caused by the rotating fluid expelling snowflakes from the centre of the vortex. In previous studies, these voids have been used to characterize the behaviour of vortices shed from the tips of the turbine blades [17, 5, 3, 47]. In the current study, we also analyse these voids to characterize the level of coherent vortical structures in the inflow approaching the turbine. There are many types of coherent structures in a turbulent boundary layer, but here we focus on coherent structures that leave signatures of vortices on our measurement plane such as the hairpin vortex packets reported the literature [33, 34, 35, 19, 38], as mentioned in the introduction. Note that the voids visible in the snow visualization images only capture a cross-section of the coherent structures as determined by the illuminated plane of the light sheet, so their three-dimensional structure (e.g., if they are true hairpin vortices) cannot be characterized.

First, the images are enhanced using wavelet denoising and adaptive histogram equalization to strengthen the void signature over the background noise. Next, they are de-warped to correct for distortion caused by the inclination angle of the camera

relative to the ground [4, 5]. From the enhanced and de-warped images, a region located 15 m upstream of the turbine and ranging from 35 m to 80 m in elevation is selected, angled such that the turbine blades are excluded (figure 3.2). Several video frames where coherent structures are clearly seen within this window (figure 3.2*a*) and several more where no coherent structures are visible (figure 3.2*b*) are manually identified for all three datasets. These manually selected frames are then used to train a machine learning-based image classifier, which labels every frame with a 0 for no visible coherent structures or 1 for coherent structures observed in the inflow (figure 3.2*c* shows a gallery of these images). A manual check was performed on several segments of automatically classified frames to ensure the accuracy of the classifier. It is worth noting that previous studies (i.e., [36, 37]) have used manual visual identification to classify periods as with or without coherent structures, and Cheliotis et al. [37] also used this manual classification method to train a machine learning-based classifier. With every frame of all three datasets classified, periods with a strong presence of coherent structures can be compared to those without structures in the inflow.

3.2.3 Particle image velocimetry with blade skipping

Particle image velocimetry (PIV) processing is conducted using PIVlab, an open-source Matlab-based PIV software [48]. As with previous studies investigating such a large FOV, the snowflake patterns in the enhanced images provide the signal for the PIV correlation rather than individual snowflakes [49, 5, 47]. In the current study, an interrogation window of 64 $\times$ 64 pixels with 50% overlap is used for the first pass, and a second pass is conducted with an interrogation window of 48 $\times$ 48 pixels with 50% overlap.

The PIV code is modified to account for the turbine blades passing through the analysed FOV, as the motion of the blades would interfere with the flow field calculation. First, the blades are detected in each frame by computing the correlation between all images in a sequence. As the blades are the strongest feature in the images, the frames with the highest correlation have the blades in the same location. These frames are averaged and converted to binary images that only contain masks of the blades, which are used to determine if a blade is within a PIV interrogation window. For each interrogation window, the frames with a blade detected are skipped during the PIV

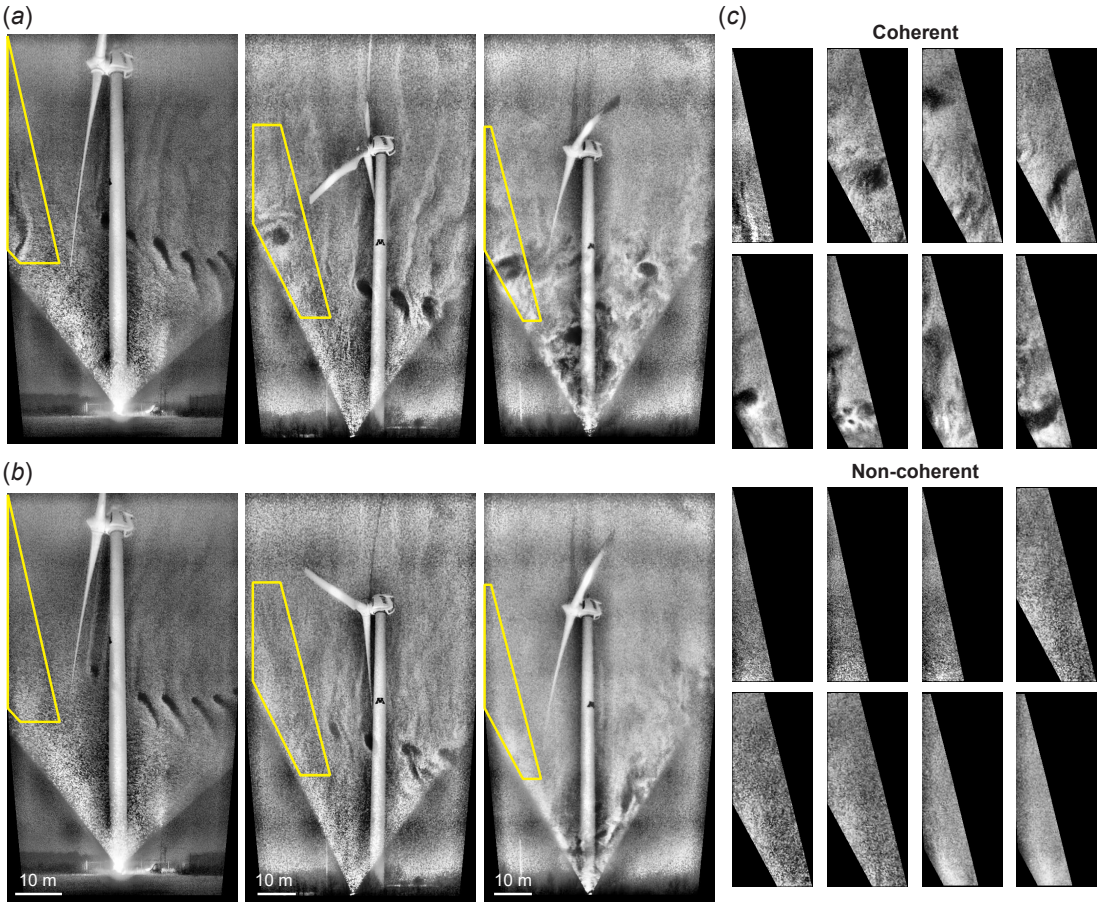

Figure 3.2: Sample frames for each of the three datasets (a) with coherent structures and (b) without coherent structures in the inflow. The yellow outline indicates the region used for the machine learning classification. Note that the physical locations of these sampling regions are the same for all three datasets, though they appear different due to the differences in the FOVs. (c) A gallery of example coherent and non-coherent images used to train the classifier.

correlation step (figure 3.3a), and the velocity vector at that location is calculated by correlating the frames before and after the blade passes through (figure 3.3b). The magnitude of this vector is divided by the number of frames skipped to account for the additional displacement that occurred during those frames. Note that the snowflake patterns persist with a clear enough signature to yield a strong correlation despite the skipped frames (figure 3.3c).

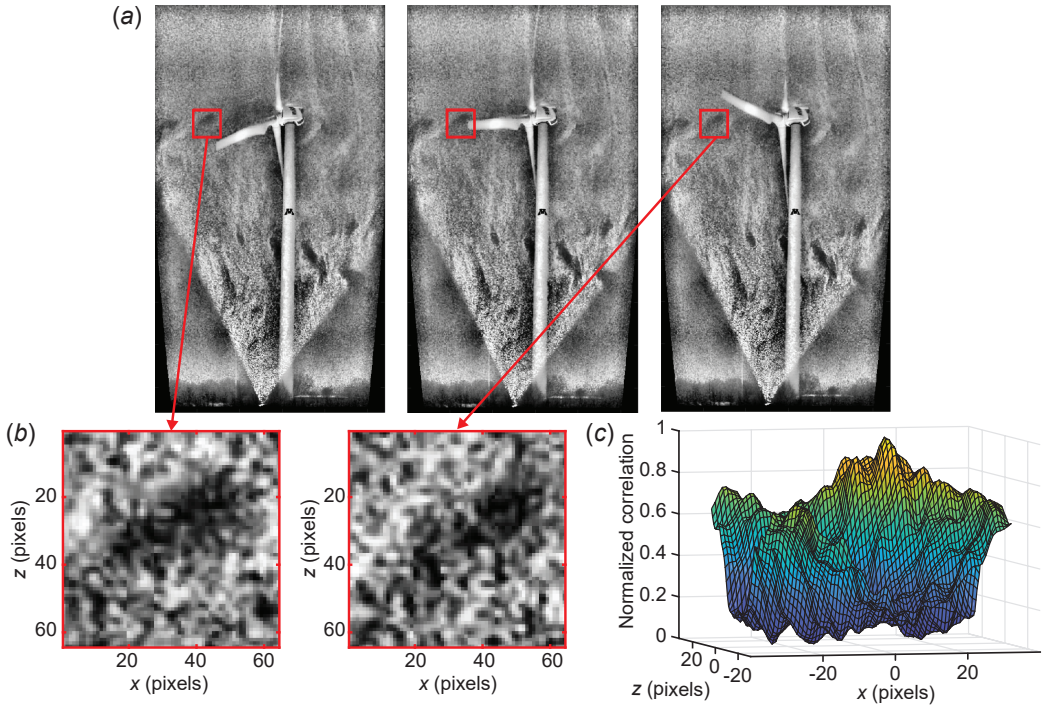

Figure 3.3: Demonstration of the PIV blade-skipping algorithm, including (a) sample images with one PIV window (64 $\times$ 64 pixels) outlined in red. The first image is the frame before the blade enters the window, the second is a frame with the blade inside the window, and the third is the frame just after the blade moves outside the window. The windows from the first and third images, exhibiting a clear pattern persisting across the frames, are shown in (b), and their correlation is shown in (c).

3.3 Results

3.3.1 Atmospheric coherent structure characterization

The image classification process shows that vortical coherent structures appear frequently at an elevation where they can interact with wind turbines (figure 3.4a). Furthermore, these coherent structures are highly intermittent, with the amount depending on wind speed (figure 3.4b). In the Apr 2018 dataset with a mean wind speed of $\overline{U}_\infty = 2.6$ m/s, coherent structures occur 3% of the time (percent of frames labeled with 1 by the classifier). In Feb 2019a, which has a higher mean wind speed of $\overline{U}_\infty = 7.0$ m/s, the percentage of frames with coherent structures increases to 50%. The Feb 2019b dataset has the highest wind speed of the three, $\overline{U}_\infty = 11.4$ m/s, leading to the highest percent of coherent structures: 71%. The level of coherent structures also increases with instantaneous wind speed, as shown in figure 3.4(c). These findings are comparable to those presented by Träumner et al. [36], who observed significantly fewer atmospheric coherent structures at wind speeds below 4 m/s. Note that the level of coherent structures does not necessarily correspond to the turbulence intensity of the inflow calculated using the nacelle anemometer. The average turbulence intensity of all periods with coherent structures observed is 0.16, very close to that of the periods without structures (i.e., 0.15).

In addition to characterizing the intermittency of atmospheric coherent structures, we also quantify two different structure scales which we term the "packet length" and the "vortex size". The packet length approximates the streamwise length of a group of vortical coherent structures in the ABL at the elevation of the region of interest shown in figure 3.2, i.e., 35 m to 80 m. This scale is calculated using the amount of time that coherent structures are consistently in the inflow, determined by the time the coherent structure classification label stays above 0.5 (figure 3.5a). The time scale is converted to length using the mean wind speed of each dataset, per Taylor's frozen turbulence hypothesis (figure 3.5b). Under the conditions presented here, coherent structure packets can extend beyond 600 m, with an increase in the number of long packets at higher wind speeds. Figure 3.5(c) shows the probability distribution function (PDF) of the packet length scale, which peaks at the smallest detectable packet scale, and decreases monotonically with increasing packet length. These results are consistent with the findings of

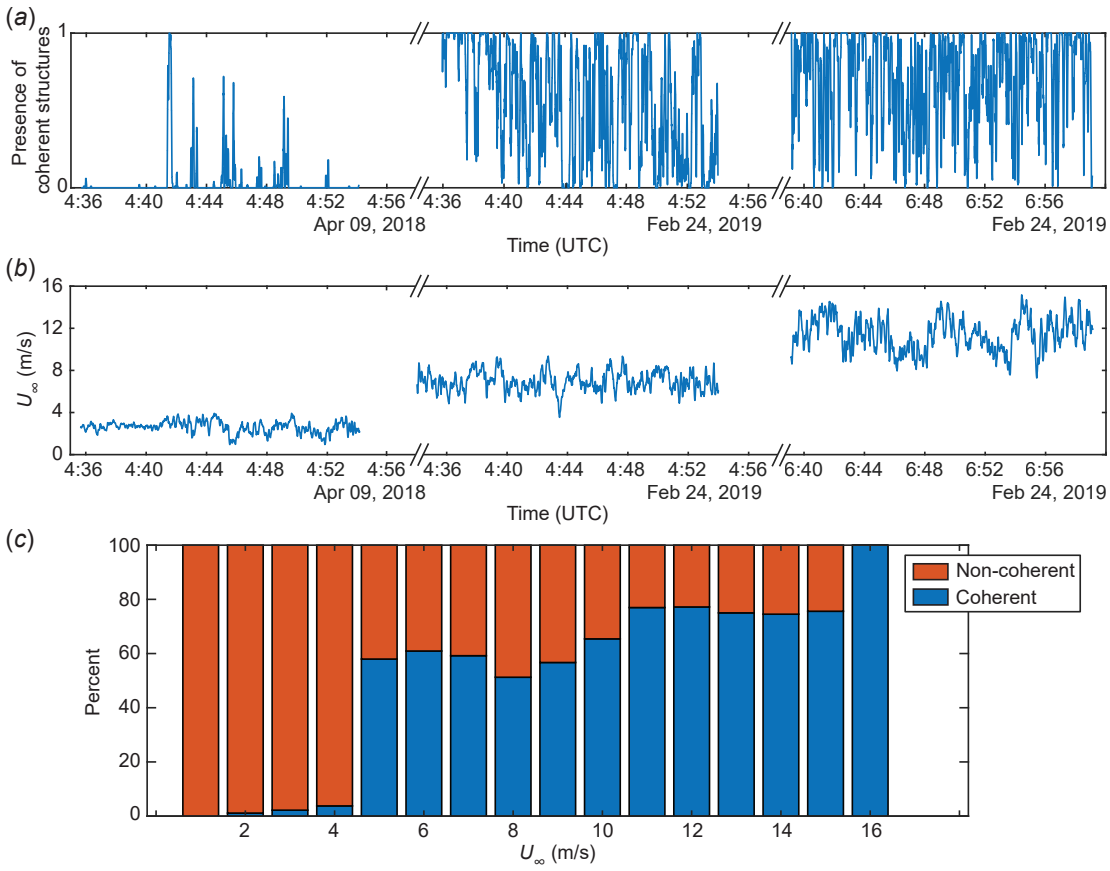

Figure 3.4: Relationship between wind speed and the level of atmospheric vortical coherent structures observed, with (a) a time series of the level of coherent structures, as determined by the image classification method, for all three datasets (smoothed with a timescale of 3 s to facilitate visualization) and (b) a time series of wind speed at turbine hub height for all three datasets. (c) Percentage of frames labelled as coherent or non-coherent by the image classifier for each instantaneous wind speed. Note that non-coherent indicates a lack of vortical coherent structures. Other types of structures may be present.

Lee and Sung [50], who investigated very-large-scale coherent structures in a canonical turbulent boundary layer using direct numerical simulation and Ganapathisubramani, Longmire, and Marusic [51], who observed hairpin vortex packets extending up to twice the boundary layer thickness in length. The long tail of the distribution indicates the presence of analogous long packets in the ABL. Previous studies have observed these structures extending up to 1500 m in the streamwise direction [36]. Such packet lengths are not observed here, though this discrepancy is likely caused by out-of-plane motions that would make very long structures appear as multiple separate structures. The organization of vortical coherent structures into packets and the shape of the packet length distribution suggest the structures observed here are signatures of canonical turbulent boundary layer structures, which originate from a disturbance at the wall and grow outwards [52]. As we will show in section 3.3.2, the packet length scale is also an important factor in determining the impact of coherent structures on turbine structural loading.

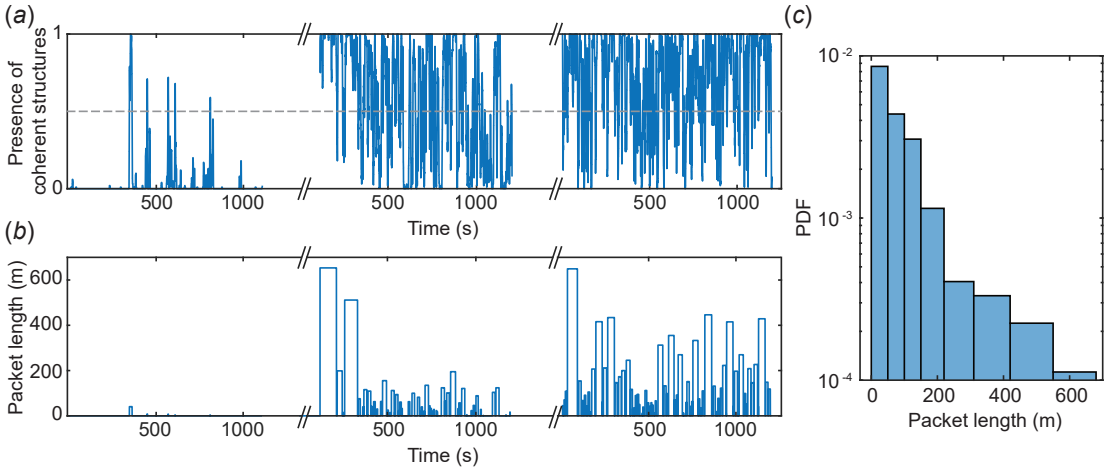

Figure 3.5: (a) The level of coherent structures from image classification, with a dashed gray line indicating the threshold, used to determine (b) the coherent structure packet length scale. (c) Probability distribution function (PDF) of the packet length for all three datasets. Note that the bin size is gradually increased for events with larger packet lengths to ensure sufficient statistical convergence for events with lower probability of occurrence.

The vortex size is estimated based on the void properties in the atmospheric flow images. The voids are extracted from the inflow region of the images using a combination of image intensity thresholding and edge detection. This image processing method is

described in detail in Abraham and Hong [3]. The cross-sectional area (A) of the largest atmospheric coherent structure in each frame is determined by the number of pixels, and an equivalent diameter of the structure is calculated using $d_{\text{eq}} = \sqrt{4A/\pi}$ (figure 3.6a). Because of the centrifugal effect of the fluid rotation on the snow particles, the edges of the voids are determined by the Stokes number, $St = \tau_p/\tau_f$, where τ_p is the particle time scale and τ_f is the flow time scale [53]. As τ_f is determined by the strength (i.e., circulation, Γ) of the vortex causing the snow particle void, the diameter of the void is directly related to the vortex strength. Therefore, the void boundaries represent a circulation threshold that is approximately equal to that determined by Hong et al. [17], i.e., $\Gamma \approx 6\text{m}^2/\text{s}$. Here, we use d_{eq} to investigate the vortex size for all three datasets (figure 3.6b). As evidenced by the size distributions shown in figure 3.6(c), the Apr 2018 dataset exhibits the fewest and smallest vortices, with $\overline{d_{\text{eq}}} = 1.0$ m, where the overbar denotes the mean. The vortices in the Feb 2019a dataset have $\overline{d_{\text{eq}}} = 1.6$ m, and Feb 2019b includes the most vortices with the largest size ($\overline{d_{\text{eq}}} = 2.3$ m). The vortex size discrepancy between the three datasets is attributed to their different values of friction velocity, U_τ. Previous studies have shown that the vortex diameter increases with distance from the wall, normalized by the viscous length scale, i.e., $z^+ = zU_\tau/\nu$ [54]. Therefore, though all three FOVs are located at the same elevation, they capture different parts of the boundary layer, with larger vortices occurring at larger values of z^+ (figure 3.6d). These findings are also consistent with the results of Ganapathisubramani et al. [51] for a canonical turbulent boundary layer. They show that the minimum vortex packet length, which corresponds to a single hairpin vortex, increases with increasing values of z^+. As we will show in section 3.3.3, vortex size is also related to the impact of inflow coherent structures on wind turbine power production and wake behaviour.

3.3.2 Impact on structural loading

We now investigate the impact of inflow coherent structures on the structural loading of the utility-scale wind turbine. As mentioned in section 2.1, 20 strain gauges are mounted around the base of the Eolos turbine support tower. In the current study, we focus on the lateral strain, i.e., the strain gauge located perpendicular to the wind direction, as we observed the strongest relationship between inflow turbulence and strain in this direction. Because of symmetry, all analysis is conducted on a single strain gauge

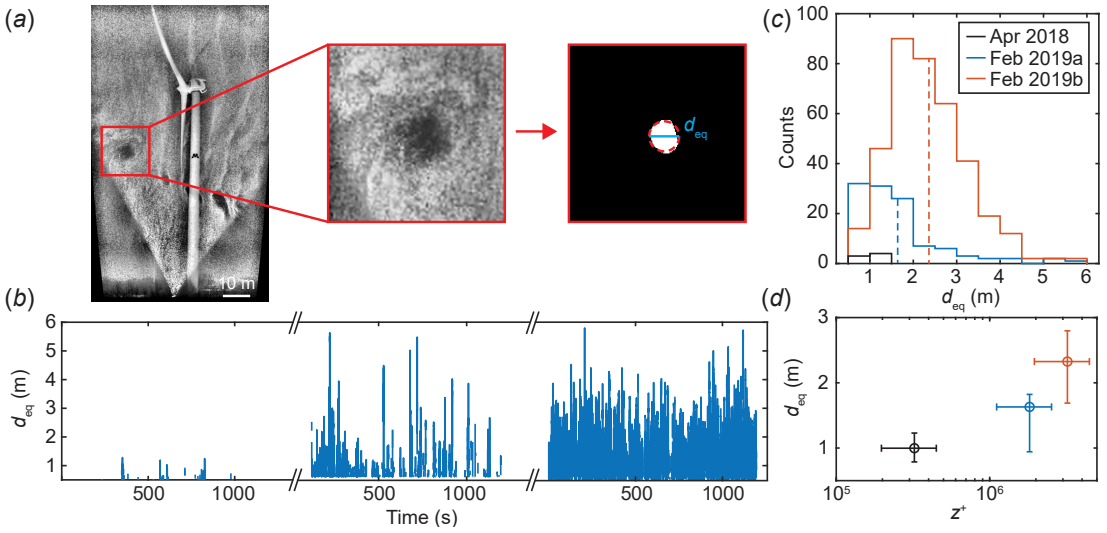

Figure 3.6: Vortex size characterization, including (a) a sample image with a coherent structure in the inflow, and the resulting extracted void. The equivalent diameter (d_{eq}) of the void is indicated by the blue line bisecting the red dashed circle. (b) A time series of d_{eq} over all three datasets. (c) Histogram of d_{eq} for each dataset, with dashed vertical lines representing the mean. (d) Relationship between z^+ and d_{eq}, with the circles indicating the mean values and the error bars representing the standard deviations. A log scale is used for z^+, as ABL quantities typically vary with the log of the elevation.

located 90° anticlockwise from the incoming wind for both Feb 2019 datasets – Apr 2018 is removed from the analysis, as the turbine is not producing power for 97% of the recorded period, and the remaining data is insufficient to derive meaningful conclusions with statistical significance (figure 3.7a). In figure 3.7(b), we show that the standard deviation of lateral strain (σ_s) and the square of the standard deviation of spanwise velocity (σ_v^2) follow similar large-scale trends. We propose this relationship is caused by fluctuations in the spanwise component of the wind exciting fluctuations in the tower strain due to the drag force exerted by the wind. Indeed, the drag force of a fluid on a cantilevered beam (like the turbine support tower) is proportional to the square of the velocity and directly proportional to the strain at the base of the beam.

However, some periods are observed where σ_s does not follow σ_v^2. One example of this deviation is exhibited in figure 3.8(a), where a strong increase in σ_s is observed, while σ_v^2 stays relatively constant. In figure 3.8(b), a proposed explanation for this increase is demonstrated with several flow visualization images from this time period.

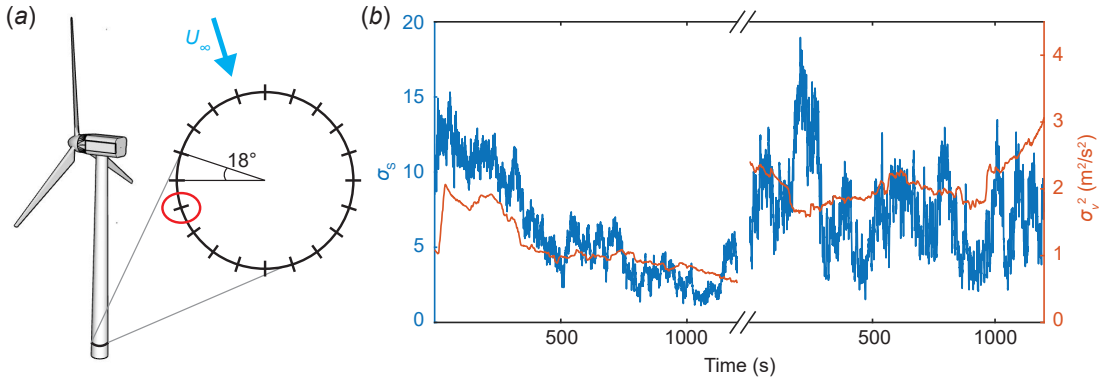

Figure 3.7: (a) Schematic showing the strain gauges located around the base of the Eolos turbine tower. The strain gauge used for the following analysis is circled in red and the wind direction is indicated by a blue arrow. (b) Time series of the standard deviation of strain (σ_s) and the square of the standard deviation of the spanwise wind component (σ_v^2) for all three datasets. Note that the Apr 2018 dataset has been removed, as the turbine is not producing power for 97% of the recorded period.

These images clearly show a strong atmospheric coherent structure entering the FOV and interacting with the turbine tower, which induces fluctuating loads on the tower. Several such coherent structures are observed during this period of increasing σ_s, though only the clearest is shown here. This example suggests that coherent structures generate additional structural loading on the turbine beyond that induced by velocity fluctuations, consistent with the findings of Kelley et al. [40].

Our results further show that tower strain fluctuations increase with increasing coherent structure packet length (figure 3.9). Once again, the Apr 2018 dataset is not included in the analysis due to the limited amount of data where the turbine is operating (only 3% of the time). However, both Feb 2019 datasets clearly exhibit the presence of long packets coinciding with peaks in σ_s (figure 3.9a). Binning σ_s by packet length shows that the general positive relationship between packet length and σ_s is consistent throughout the entirety of the data collected (figure 3.9b). These findings are consistent with the understanding developed in the study of lower Reynolds-number turbulent boundary layers that longer packets contribute significantly more turbulence production and momentum transport than shorter packets [51]. In interacting with a utility-scale wind turbine, this additional turbulence and momentum leads to increased fluctuating

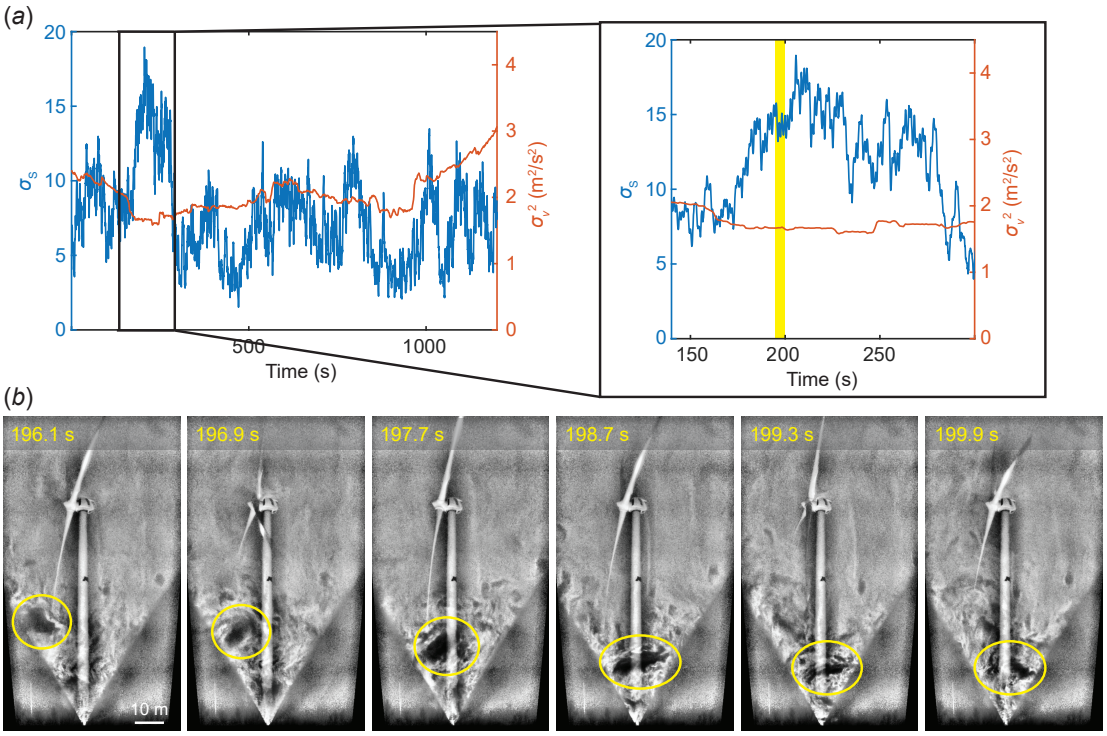

Figure 3.8: Effect of coherent structures on tower strain, including (a) an example of σ_s deviating from σ_v^2. The yellow bar indicates the time range of the images shown in (b), which highlight an atmospheric coherent structure (circled in yellow) impinging on the turbine tower. Several such structures were observed during this period of increased σ_s, though only the clearest is shown here.

loads on the structure. This phenomenon has not been previously observed at such high Reynolds numbers as those investigated in the current study ($Re \sim 10^7$). This finding also has important implications for wind farm siting decisions, as landscape features or buildings that generate large coherent structures can lead to additional structural fatigue loading.

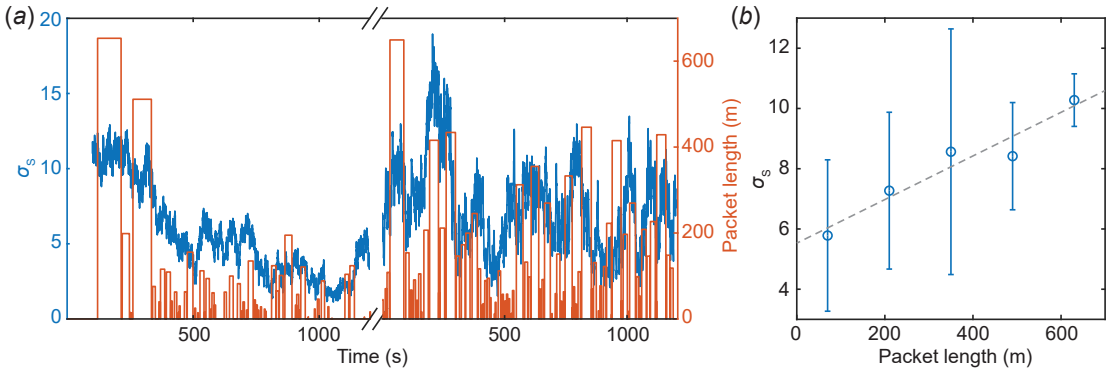

Figure 3.9: Relationship between coherent structure packet length and standard deviation of lateral tower strain (σ_s), including (a) a time series across all three datasets, and (b) a scatter plot with the σ_s data points binned by packet length. The circles indicate the mean value of σ_s for each value of packet length, and the error bars indicate the standard deviation. Once again, the Apr 2018 dataset has been removed due to the limited duration of turbine operation (3%).

3.3.3 Impact on power production and wake behaviour

We next explore the effect of coherent structures on turbine power production and wake behaviour. When the turbine is producing power and extracting energy from the wind, the wake typically expands as the air slows down due to mass and momentum conservation. Previous studies have observed some periods of wake contraction caused by changes in the pitch of the turbine blades [3, 5]. These blade pitch changes occur when the turbine is operating above the rated wind speed (region 3), and the turbine reduces the angle of attack of the blades to regulate loading on the turbine. In the current study, we focus on periods when the turbine is operating in region 2 and the blade pitch is not changing. Instances of wake contraction are also observed under these

conditions, suggesting the existence of an additional mechanism leading to wake contraction. Closer investigation reveals that these contraction periods occur when there are coherent structures in the inflow that interact with the turbine (figure 3.10a). Furthermore, they coincide with a reduction in power generation compared to the expected performance based on the turbine power curve (figure 3.10b).

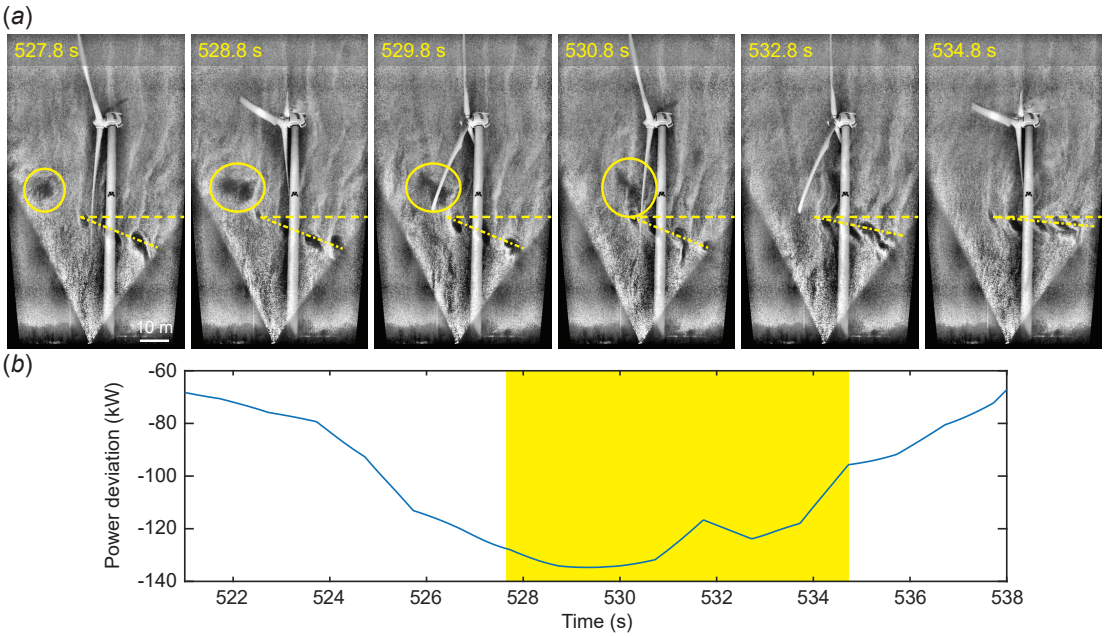

Figure 3.10: Example of a coherent structure interacting with the turbine and inducing (a) a reduction in wake expansion and (b) a reduction in power generation. In (a), the coherent structure is circled in yellow, and the wake expansion angle is indicated by the yellow lines. The dashed line represents the bottom blade tip elevation, and the dot-dashed line shows the position of the tip vortices. The yellow region marked in (b) indicates the time period shown in the images. Power deviation is defined as the expected power production at the given wind speed based on the power curve, subtracted from the actual power produced.

To characterize this wake contraction behaviour, we develop a method to quantify the wake expansion angle. Using an image processing technique similar to that described in section 3.3.1, binary images of the tip vortices are extracted from the enhanced snow images. The centroid of the tip vortex nearest the turbine is determined from the binary image, and the angle of the centroid from the elevation of the bottom turbine

blade tip (φ_w) is calculated (figure 3.11). The wake expansion angle is quantified for the entire Feb 2019a dataset, where the turbine operates in region 1.5-2. Any periods of wake contraction observed while the turbine is operating in these regions cannot be attributed to changes in blade pitch, which is fixed to a minimal value of 1° to maximize power generation.

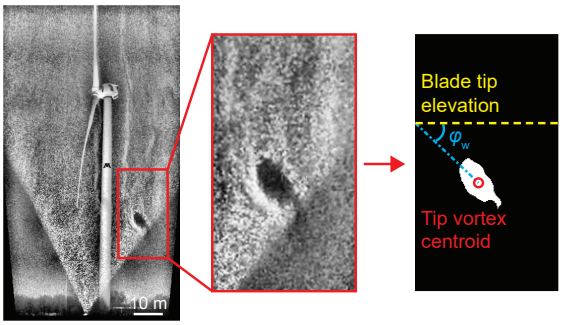

Figure 3.11: Definition of wake expansion angle, φ_w, as determined using the centroid of the bottom blade tip vortex and the elevation of the tip of the bottom turbine blade.

Figure 3.12 shows a time series of φ_w, power deviation, and vortex size (d_{eq}). Power deviation is defined as expected power subtracted from actual power, where expected power is determined using the Eolos turbine power curve and the instantaneous hub-height wind speed. The expected power is filtered and shifted in time to maximize the correlation with the actual power. A negative value of power deviation indicates the turbine is under-producing, while a positive value indicates the turbine is producing more power than expected. Vortex strength, as defined in section 3.3.1, is determined based on incoming coherent structure size. Five periods are highlighted in figure 3.12 where a large power deviation is observed. For the three periods where this power deviation is negative (marked in blue), φ_w is also negative, indicating wake contraction. All five periods also coincide with above-average values of d_{eq}. The images showing the spanwise vorticity (ω_y) and vector fields superimposed on the snow visualization images for each period provide further insight into the cause of the power surpluses and deficits observed. For the power deficit periods, large coherent structures with negative vorticity are observed in the inflow. For the power surplus periods (marked in yellow), large structures with positive vorticity are detected. We attribute this dependence on rotation direction to lift generation on the turbine blades. Lift is directly proportional

to the circulation around the blade cross-sections per the Kutta-Joukowsky equation [55]. The positive vorticity of the vortices shed from the blade tips indicates that the bound circulation on the blades is also positive. Therefore, negative vorticity in the inflow neutralizes some of the lift, reducing the power generation and inducing wake contraction, while positive vorticity enhances the lift, increasing power generation.

Not every period with a large power surplus or deficit demonstrates this clear relationship with inflow coherent structure vorticity because of the complex nature of field data. In the field, turbine and wake behaviour are influenced by many different variables, making it difficult to establish a clear one-to-one correspondence between variables. In particular, the FOV of the flow visualization data only captures a cross-section of the inflow, so the three-dimensionality or structures appearing outside of the visualized plane cannot be detected. Some of the large power deviations are likely caused by structures outside of the FOV plane. Still, a statistically robust relationship between power deviation and vortex size is observed (figure 3.13). The histogram of power deviation magnitude conditionally sampled by inflow vortex size shows a clear separation between vortices that are below and above the mean value of d_{eq}. This separation is further strengthened when comparing vortices from the bottom and top quartile of d_{eq}, which correspond to the smallest and largest quarter, respectively, of all vortices detected in the inflow while the turbine is operating in region 2.

3.4 Conclusion

In this study, we characterize turbulent coherent structures in the atmospheric boundary layer and investigate their impact on utility-scale wind turbine loading, power generation, and wake behaviour. This investigation is conducted using flow visualization with natural snowfall with a field of view spanning the inflow and near wake of a 2.5 MW turbine. Coherent vortical structures in the inflow are detected using a manually trained image classifier and the flow field is quantified with SLPIV. Three datasets with different conditions reveal the substantial increase in inflow coherent structures with increasing wind speed. The coherent structure packet length, determined by the duration with coherent structures consistently in the inflow, exhibits a long-tailed distribution similar to that observed for hairpin vortex packets in canonical turbulent boundary layers.

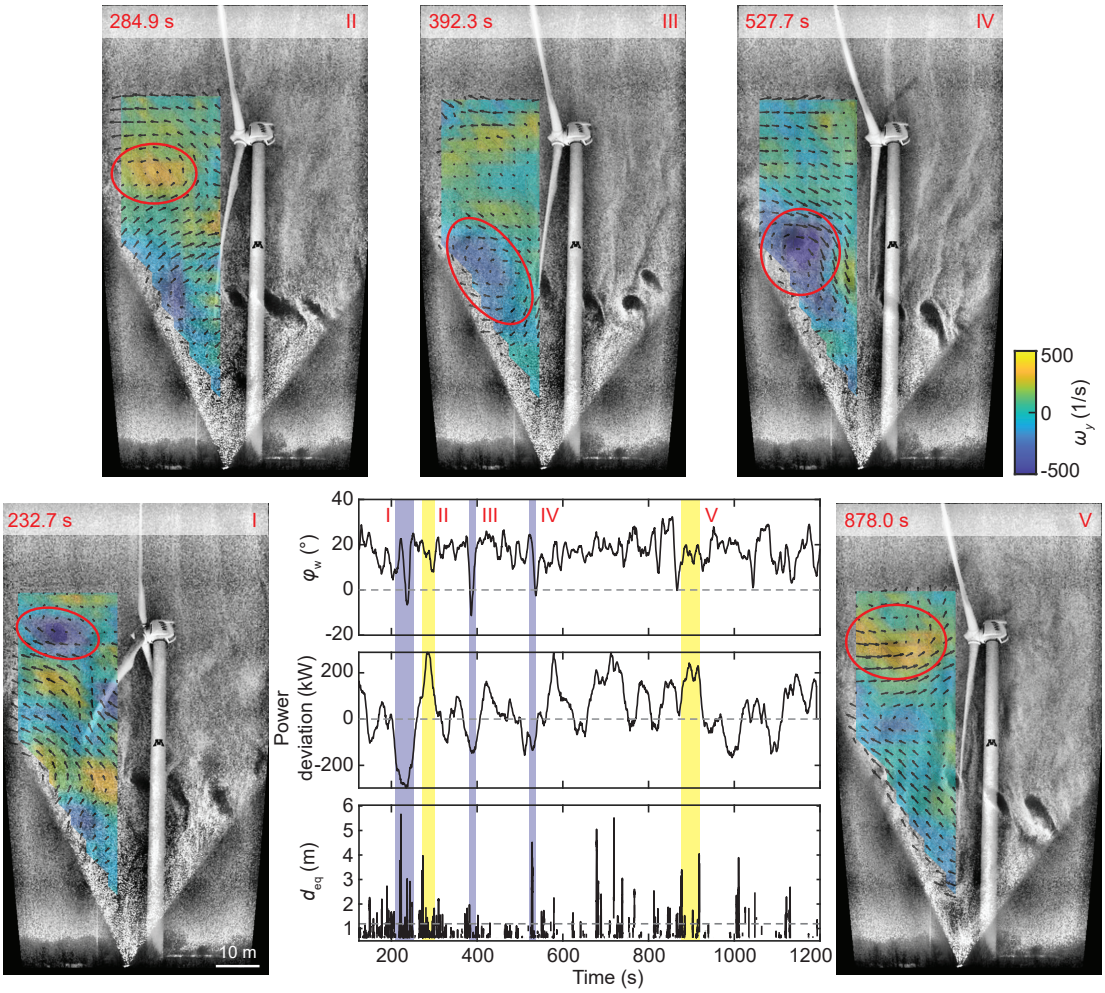

Figure 3.12: Time series of wake expansion angle (φ_w), power deviation (expected power subtracted from actual power), and vortex strength. The blue and yellow bars indicate periods with strong power deficits and surpluses, respectively. The red numbers correspond to the images show around the plot, which are sample enhanced snow particle images superimposed with spanwise vorticity and vector fields from each highlighted time period. The vector fields represent the fluid velocity with the mean subtracted. Note that the region of positive vorticity around the bottom blade tip in some images is caused by recently generated tip vortices.

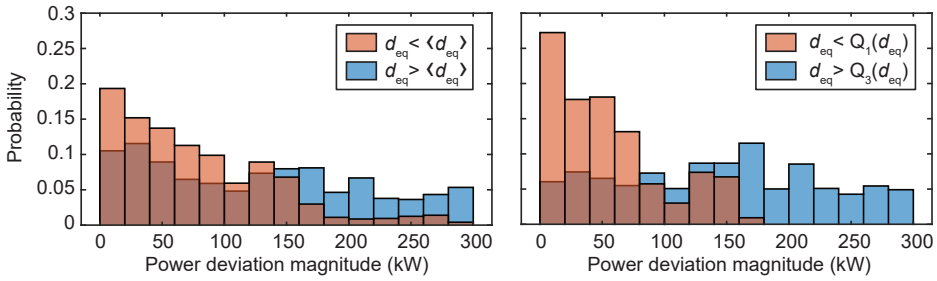

Figure 3.13: Magnitude of power deviation magnitude conditionally sampled by vortex size. The plot on the left compares the vortices below and above the mean value of vortex size ($\langle d_{\mathrm{eq}} \rangle$), while the plot on the right compares vortices in the bottom and top quartile of vortex size ($\mathrm{Q}_1(d_{\mathrm{eq}})$ and $\mathrm{Q}_3(d_{\mathrm{eq}})$, respectively).

Meanwhile, the inflow vortex size distribution varies between the three datasets due to differences in the friction velocity. Turbine structural loading is shown to depend on spanwise wind speed fluctuations, though some periods exhibit disproportionately high tower strain fluctuations due to interaction with coherent structures. Tower strain fluctuations also increase significantly with increases in coherent structure packet length. Finally, we observe a relationship between large vortical coherent structures in the inflow and deviations in turbine power production from the expected value based on the power curve. These deviations are attributed to rotation direction of the atmospheric structures, with positive vorticity leading to a power surplus, and negative vorticity leading to a power deficit along with wake contraction.

These findings have implications for wind turbine design and siting decisions. On the one hand, coherent structures tend to induce increased structural loading and deviations from expected turbine performance, both of which increase the cost and uncertainty of wind farm operation. On the other hand, our findings suggest that coherent structures with the same rotation direction as the blade circulation have the potential to boost power generation on short timescales. Consequently, the size, rotation direction, and frequency of occurrence of vortical coherent structures should be evaluated alongside mean wind conditions at prospective wind farm sites. These factors should then be included in considerations for turbine design and layout decisions. In particular, because of the direction of shear in the ABL, large structures with negative vorticity are more common than those with positive vorticity [19]. Consequently, it may be beneficial to

select turbine rotation direction such that blade circulation is negative as well. Finally, we reveal an additional mechanism leading to turbine wake contraction. Dasari et al. [5] showed that wake contraction occurs in region > 2 when the blade pitch changes and the turbine is deflected into its own wake. In the current study, we further show that wake contraction can also be induced in region ≤ 2 by coherent vortical structures in the inflow reducing the lift generated by the blades. This near-wake behaviour can significantly impact wake development downstream, including wake length, recovery, and mixing.

One limitation of this study has already been mentioned, i.e., a single plane of visualization data which does not allow us to observe the entire three-dimensional shape of the coherent structures or detect structures outside of the plane. The current study also focuses exclusively on vortical coherent structures, as they can be easily visualised using natural snowfall. However, the impact of other boundary layer coherent structures (e.g., streaks, rolls) has not been evaluated. In addition, all three datasets were collected at the same site, which has a relatively uniform surface roughness. Surface roughness is expected to affect the properties of the coherent structures appearing in the ABL, but we do not expect the main trends presented here to be significantly modified. Finally, the turbine geometry (e.g., rotor diameter, height, blade profile, etc.) will influence the magnitude of the coherent structure impact on loading, power, and wake. However, the physical mechanisms described here will remain relevant regardless of turbine design.

Chapter 4

Effect of turbine nacelle and tower on the near wake of a utility-scale wind turbine

The content of this chapter has been published by the author in *Journal of Wind Engineering and Industrial Aerodynamics* [49]. Content has been reprinted here with permission.

4.1 Introduction

A thorough understanding of the wind turbine wake is critical for improving the efficiency of individual turbines and overall power production of a wind farm [56, 57]. In the near wake, i.e., the region within $1-4D$ downstream of a turbine, where D is the rotor diameter [22, 23], coherent structures emanating from different portions of the turbine, including tip and trailing sheet vortices from the blades as well as the vortical structures from the nacelle and tower, interact strongly to affect general characteristics and stability of the wake flow and its evolution downstream [58]. Up to date, a large number of studies have examined in detail the behavior of blade-generated structures, particularly the tip vortices [59, 60, 61, 62, 63, 64, 65], but only very few studies focused on the coherent structures produced from the turbine nacelle and tower and their effect

on near-wake flows.

Nevertheless, from a series of experiments conducted by NREL on a full scale two bladed wind turbine (a diameter of 10 m, hub height of 12.2 m and a rated power of 20 kW) using the NASA Ames wind tunnel [66, 67], it was revealed that the turbine tower induces significant reduction of loading (e.g. aerodynamic torque) on the blades as they pass in front of the tower. Following these experiments, several numerical studies using different simulation methods, including unsteady RANS, Reynolds averaged Navier-Stokes [**?**, 68, 69, 70] and finite element ALE-VMS (arbitrary Lagrangian-Eulerian-variational multiscale formulation) methods [71], provided further evidence of the unsteady loading effect associated with the presence of the turbine tower. In particular, using RANS on a downwind turbine, Zahle et al. [**?**] captured the tower wake and its interaction with the rotor blades, which introduces highly transient loading on the blade. The study further noted that the axial induction caused by the rotor can considerably alter the tower vortex shedding and at times introduced a state of lock-in, a phenomenon where the natural frequency of a system is altered and synchronized with a forcing frequency, i.e. the blade passage frequency in this case. Other studies using RANS and Large Eddy Simulation (LES) have observed a velocity deficit in the near wake caused by the presence of the tower [72, 73, 74]. However, none of these numerical studies have systematically characterized the behaviors of these flow structures (tower and nacelle structures) and their effect on the near wake velocity and turbulence. In wind tunnel studies of model wind turbines [75, 76] and follow-up LES simulations of the same turbines [77, 78], a peak in turbulence intensity was observed in the near wake caused by the presence of the nacelle. In a water tunnel flow visualization experiment on a marine propeller model, Felli, Camussi, and Di Felice [79] observed that the vortical structure produced from the rotor nacelle, a nacelle vortex, meanders at a frequency equal to the rotational frequency of the rotor. Such meandering behavior of the nacelle vortex was also observed from hot wire measurements on a model turbine in a wind tunnel by Iungo et al. [80]. However, the meandering frequency was found to be one third of the rotor frequency, consistent with the stability analysis conducted in their study. Viola et al. [81] further improved on the stability analysis by incorporating effects of the Reynolds stresses through eddy-viscosity models, and provided further evidence for

the meandering frequency obtained in Iungo et al. [80]. Applying particle image velocimetry (PIV) along a wall-parallel plane on a model wind turbine wake, Howard et al. [82] also investigated the meandering motion of the nacelle vortex. The nacelle vortex signature was identified as a two-dimensional meandering line connecting the velocity minima at each streamwise location downwind of the turbine. They showed that the wavelength and amplitude of the meandering line vary with wake velocity representing a weak compressing or stretching mechanism, and are also correlated to the turbine loading. They also observed a second, lower far wake meandering frequency attributed to the rotor blockage effect. Following the same method of identifying nacelle vortex meandering as employed by Howard et al. [82], Foti et al. [83] conducted large eddy simulations (LES) on a miniature turbine and showed that the nacelle vortex exhibits a slow precessing motion immediately downstream of the nacelle opposite to the turbine rotation direction, resembling a spiral vortex breakdown. The helical meandering motion of the nacelle vortex further downstream was found to arise from this precessing motion. Using actuator disk, actuator line and turbine resolving LES techniques on a hydrokinetic turbine, Kang, Yang, and Sotiropoulos [25] conducted a systematic investigation of wake meandering and pointed out that the interaction between turbine nacelle and blade-tip vortices in the near wake augments wake meandering.

Only recently, a number of numerical studies have started looking into the effect of nacelle and tower on wind turbine wake flows. Specifically, using novel actuator surface models for the turbine blades and nacelle, Yang and Sotiropoulos [84] showed that the turbine nacelle increases turbulent kinetic energy (TKE) significantly in the near wake. Wang et al. [85] conducted LES on model-scale turbines with fully-resolved turbine geometry using an immersed boundary method, and demonstrated the pronounced effect of both nacelle and tower on the near wake characteristics. Specifically, the nacelle and tower were found to generate substantial amounts of turbulence, which in turn enhanced downstream flow mixing. However, the authors suggested that the pronounced effects of nacelle and tower are caused by the relatively larger nacelle and tower sizes of the model turbines employed in the study in comparison to those in utility-scale wind turbines. Similarly, Santoni et al. [86] applied LES to a scaled-down turbine with well-resolved tower and nacelle geometries, and showed that the tower and nacelle cause a substantial velocity deficit and affect TKE and associated fluxes, especially in the portion of the

wake with tower influence. The tower wake was also found to interfere with the turbine blade wake, promoting tip vortex breakdown.

Despite these recent studies mentioned above, no field study has ever been performed on utility-scale wind turbines to investigate the behavior of the flow structures generated from turbine tower and nacelle and determine their effect on near-wake characteristics. Considering the significant discrepancy between field and laboratory conditions, including Reynolds number, atmospheric conditions, turbine characteristics, etc., such a study is necessary for validating the observations derived from laboratory and numerical work, and can potentially reveal new and important physics occurring at utility-scale settings. Needless to say, the measurements required for such study are very difficult to obtain with conventional field measurement tools (e.g., lidar, sodar and radar, etc.), which do not yield sufficient spatial and temporal resolution to effectively capture the dynamics of near-wake coherent structures and their interactions.

Nonetheless, by taking advantage of natural snowflakes as flow tracers, a recent study by Toloui et al. [4] first introduced super-large-scale particle image velocimetry (SLPIV) for flow measurements in the atmospheric boundary layer (ABL) over large fields of view. Specifically, they implemented SLPIV to characterize the ABL through a pilot experiment in an area of $\sim$ 22 m $\times$ 52 m with a spatial resolution of 0.34 m and a temporal resolution of 15 Hz, which was validated by comparing with sonic anemometer measurements from a meteorological tower nearby. Successively, Hong et al. [17] applied the same technique along with flow visualization to study the complex flow field and coherent structures in the near wake of a 2.5 MW wind turbine. This work quantified a flow field of $\sim$ 36 m $\times$ 36 m at $\sim 0.3D$ downstream of the turbine, and further demonstrated correlations between the turbine operation and the coherent structures in the near wake. Moreover, Dasari et al. [5] further implemented SLPIV to quantify a larger flow field 115 m $\times$ 66 m at $\sim 0.4D$ downstream of the turbine and $0.19D$ offset from the central tower plane, and compared the wake velocity deficit with a number of existing wake models. Owing to the high spatiotemporal resolution of SLPIV, the study revealed an intermittent wake contraction behavior (about 25% of time) which was found to be correlated with the rate of change of blade pitch. In addition, the study showed correlations between the tip vortex behavioral patterns and turbine operation and response characteristics like power, tower strain, blade pitch, angle of attack, and

their fluctuations which opens up avenues to predict the wake behavior based on readily available turbine operational parameters. However, as the study was conducted on a plane offset from the tower plane, the coherent structures emanating from the nacelle and tower could not be visualized and their potential implications on the near wake could not be studied.

Following Dasari et al. [5] and using similar flow visualization and SLPIV techniques with natural snowflakes, the current paper focuses on investigating the flow structures produced by the tower and nacelle of a utility-scale turbine and their impact on near-wake mean flow and turbulence characteristics. The study is based on a field campaign conducted in March 2017 at the symmetry plane behind the tower in the near wake of the 2.5 MW turbine used in Hong et al. [17] and Dasari et al. [5]. This chapter is structured as follows: Section 4.2 provides a brief description of the experimental methods, field campaign and data processing procedures. Section 4.3 focuses on the dynamic behaviours of the coherent structures shed from the nacelle and tower. Section 4.4 provides a summary and discussion of the results.

4.2 Methodology

The current study investigates 1 hour of data obtained from a deployment conducted on March 12th, 2017 in the wake of the Eolos turbine. The details regarding the dataset are summarized in tables 4.1 and 4.2 with a schematic presented in figure 4.1 illustrating the key parameters for the measurement setup. Specifically, as shown in table 4.1 and figure 4.1, the location of the field of view (FOV) for each dataset is characterized by its downstream distance from the tower (x_{FOV}), its offset from the central tower plane (y_{FOV}) and the elevation of the FOV center above the ground level (z_{FOV}). The dimension of the FOV is characterized by its height (H_{FOV}) and width (W_{FOV}). The distance between the camera and the light sheet is represented by the LCL with θ indicating the tilt angle of the camera. The FOV is located very close to the central tower plane ($0.06D$ offset from the tower plane). This dataset is exclusively used for quantitative examination of the near-wake turbulent flow field. Table 4.2 summarizes the detailed meteorological information as well as the turbine operational conditions. The wind speed and direction are measured by the sonic anemometer at the nacelle of the Eolos

turbine. Temperature and humidity are measured at the met tower. The turbulence intensity and Obukhov length are calculated from the acquired data accordingly.

Table 4.1: A summary of the key parameters of the measurement setup for the deployment dataset used in the present study.

Date	Duration	FOV location (x_{FOV}, y_{FOV})	FOV elevation (z_{FOV})	FOV size ($H_{\mathrm{FOV}} \times W_{\mathrm{FOV}}$)	Camera-to-light distance (L_{CL})	Tilt angle (θ)
March 12th, 2017	62 min	$0.35D$, $0.06D$	80 m	125 m × 70 m	171 m	24.5°

Table 4.2: A summary of the key parameters of the atmospheric and turbine operational conditions.

Mean wind speed at hub height	Mean wind direction	Turb. intensity	Mean temperature	Relative humidity	Obukhov length	Turbine operational region	Tip speed ratio
5.9 m/s	58°	0.18	-8.1°C	93%	131 m	1.5-2	8-11.5

It is to be noted that conditions related to the experimental setup orientation (viz. wind direction, turbine nacelle direction) change continuously during the deployment. Figure 4.2 provides a time series of these parameters during the night of March 12th, 2017. The figure also showcases the 3 data collection periods, which together constitute 62 minutes of visualization data. From this plot it is clear that there is considerable misalignment up to 25° between the light sheet direction (dashed line in the figure) and the wind direction (solid line) during this period. Such misalignment results in up to 9% reduction in the mean velocity magnitude measured at the tower plane, and more importantly, a disappearance of nacelle and tower flow structures in the sample plane at high degrees of misalignment. To account for this, conditional sampling is applied based on the misalignment angle, $\gamma_{\mathrm{L,W}}$, which is the magnitude of the difference between the wind direction and the light sheet direction. When $\gamma_{\mathrm{L,W}} \leq 10°$, the data is considered aligned, and when $\gamma_{\mathrm{L,W}} \geq 20°$, the data is considered misaligned. These cut-off values were selected to ensure the tower wake always intersects the light sheet in the aligned

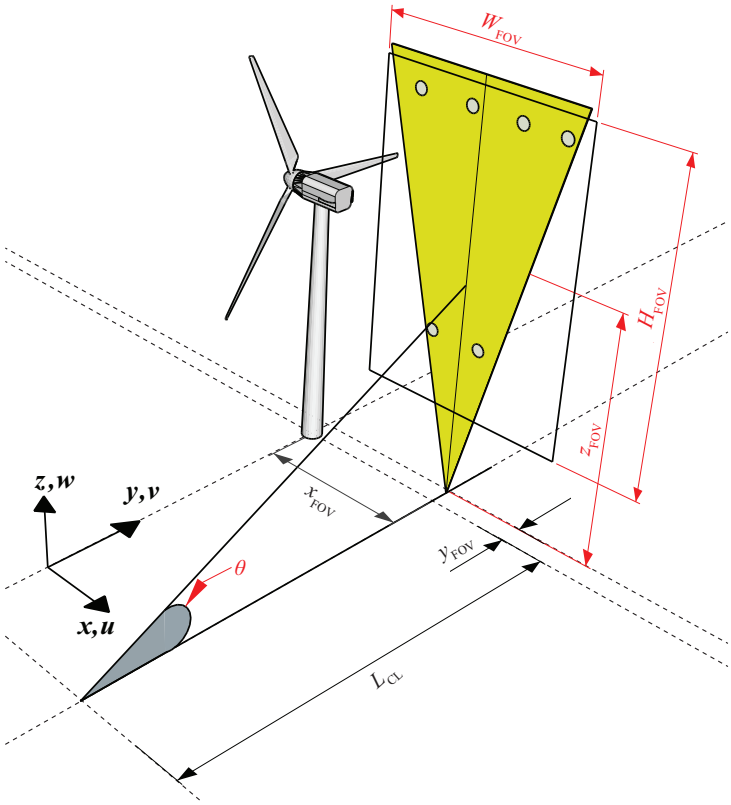

Figure 4.1: Schematic of the measurement setup used in the deployment.

condition and to ensure sufficient data in each category (600 seconds and 16% of the data is included in each category).

The velocity vectors are calculated using the adaptive multi-pass cross correlation algorithm from LaVision Davis 8. The cross correlation was first conducted using an initial interrogation window of 128 × 128 pixels which was then reduced to 32 × 32 pixels with 50% overlap, providing a spatial resolution of 4.2 m/vector ($\sim 0.04D$/vector). The cross correlation is also applied to image pairs with 5 frame skip in a time sequence of images to ensure sufficient displacement of snow patterns between the two images within a pair, resulting in temporal resolution of 6 Hz. In terms of the mean rotational frequency of the rotor, $\overline{\Omega} = 23$ Hz, this temporal resolution corresponds to $\sim 26\overline{\Omega}$.

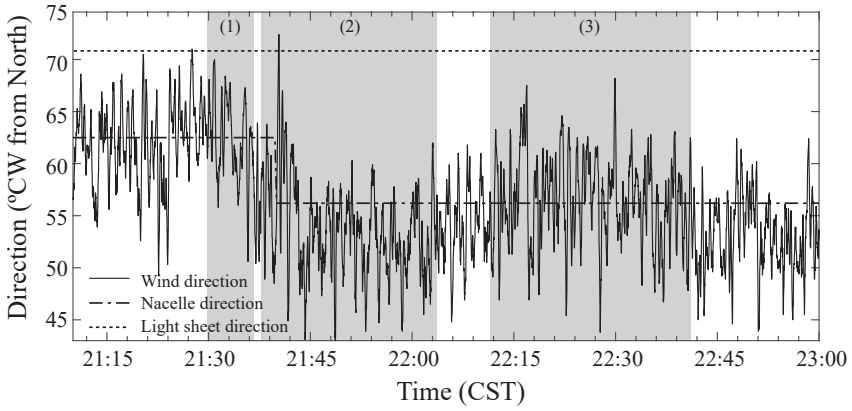

Figure 4.2: Time series of wind, nacelle, and light sheet direction on March 12th, 2017 marked with video data collection periods, indicated by gray bars.

4.3 Dynamic behavior of coherent structures

Coherent structures in the near wake are visualized as regions of low snowflake concentration, or voids. These voids are the result of particle inertia in regions of high vorticity in the turbulent flow, as described in detail by Hong et al. [17] and Dasari et al. [5]. Previous studies have observed blade tip vortices and trailing sheet vortices, but the alignment of the field of view in the current study with the tower plane enables the visualization of the vortices shed from the blade roots, nacelle, and tower. A sample video frame exhibiting all of these structures is shown in figure 4.3. The most apparent feature of this image is the contrast between the bottom and top halves of the wake. The top half (above the hub) shows regular tip, root, and trailing sheet vortices shed periodically from the turbine blades. In the bottom half, however, the structures are much more chaotic as a result of the interaction between vortices shed from the blades and those shed from the tower. In the region behind the tower, tip and sheet vortices are still visible, but they are heavily distorted. The nacelle vortex, distinct from the blade root vortices, is visible in the region directly behind the nacelle.

4.3.1 Nacelle wake

The dynamic characteristics of the nacelle wake are first investigated using the method introduced in Howard et al. [82] and Foti et al. [83] for quantifying the wavelength of

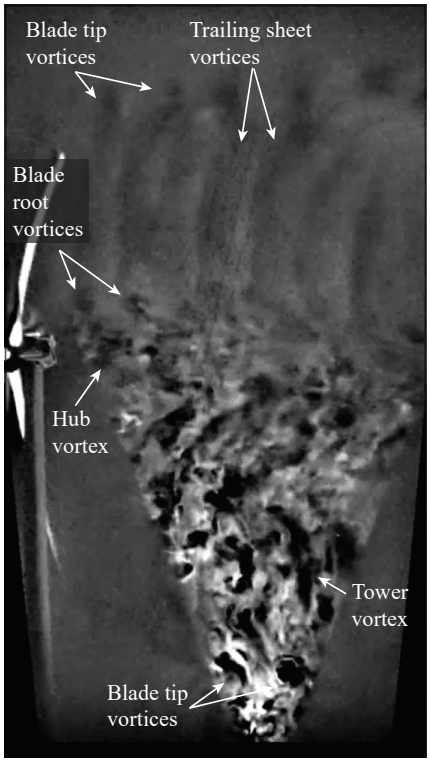

Figure 4.3: Coherent structures in the near wake of the turbine, visualized as regions of snowflake voids.

nacelle wake meandering. The steps of this process are shown in figure 4.4. A region of the velocity profile around the nacelle between $-0.2 < (z-H)/D < 0.2$ at a downstream location of $x/D = 0.41$ is selected (figure 4.4*a*). The elevation corresponding to the center of the nacelle wake is identified for each time step as the local velocity maximum within this region, defined as z_{NW} (figure 4.4*b*), and Taylor's hypothesis using the mean convection velocity in the nacelle region of the wake is applied to convert the time sequence to a spatial meandering signature. A sample sequence of the nacelle wake center position is shown as the light gray line in figure 4.4(*c*). Note that Howard et al. [82] and Foti et al. [83] defined the nacelle wake center as the velocity minimum because they did not observe a region of flow acceleration around the nacelle. Their wake velocity profile did not have a peak behind the nacelle because the blades of the model turbine used in both studies did not have the circular cross-sections at the roots seen on utility-scale turbine blades, including the Eolos turbine, that cause the reduction in axial

induction near the hub. Additionally, the nacelle diameter of the model turbines was 10% of the rotor diameter, significantly larger than that of a utility-scale turbine ($0.05D$ for the Eolos turbine), causing increased blockage around the nacelle. The nacelle wake position sequence is then low-pass filtered with a cutoff frequency equal to the average hub rotation frequency to focus the analysis on larger-scale behaviors. The filtered signal is the black line in figure 4.4(c). The wavelength is calculated as the distance between adjacent peaks and adjacent troughs, as shown in figure 4.4(c). Wavelengths from the entire dataset are compiled into a probability distribution function (PDF) and fit with a normal distribution using the method of maximum likelihood estimation, providing a mean wavelength of $\langle \lambda_{\mathrm{NW}}/D \rangle = 0.55$ and a standard deviation of 0.19 (figure 4.4d). This mean value is consistent with that observed by Foti et al. [83] in the extreme near wake of a model turbine ($x < D$). Calculating a Strouhal number for nacelle wake meandering based on the rotor diameter leads to $St_{\mathrm{D}} = \frac{f_{\mathrm{NW}} D}{U_{\mathrm{nacelle}}} = \frac{U_c D}{\lambda_{\mathrm{NW}} U_{\mathrm{nacelle}}} = 1.7$, a value significantly higher than that observed by previous laboratory-scale studies: $St_D = 0.7$ [82, 83]. This discrepancy could be related to the reduced velocity deficit around the nacelle, not observed in the aforementioned studies, which would affect the ratio U_c/U_{nacelle}. However, calculating the nacelle wake Strouhal number based on the nacelle dimension gives $St_{\mathrm{n}} = 0.06$, a value consistent with Howard et al. [82] who reported $St_{\mathrm{n}} = 0.06$, and close to the range of $St_{\mathrm{n}} = 0.03 - 0.05$, calculated from the frequency, velocity, and geometry provided by Iungo et al. [80] for a different laboratory-scale model turbine. This value of St_{n} is also consistent with studies investigating vortex shedding from an Ahmed body, a roughly cuboidal bluff body with a similar shape to the nacelle, used to model automobile aerodynamics [87, 88]). These studies have shown that vortices shed from the upper and lower surfaces of the body interact to form a ring vortex which moves back and forth, generating a low frequency pumping motion that sheds vortices from the back of the separation bubble. The Strouhal number of this pumping is in the range of 0.059 to 0.069, matching the Strouhal number observed in the current study in the near wake of the nacelle. This suggests the nacelle wake behavior is influenced by both the rotor dynamics and bluff body shedding from the nacelle. The rotor generates the region of accelerated flow around the nacelle, and the nacelle sheds coherent structures at the frequency governed by the interaction between vortices generated by the shear on its surfaces. Both of these effects are difficult to

model on the laboratory scale due to discrepancies in blade shape and relative nacelle size compared to utility-scale turbines. At this extreme near-wake position, the nacelle wake has not yet expanded enough to be influenced by the coherent structures shed from the blades, which has been shown to occur further downstream [83, 84].

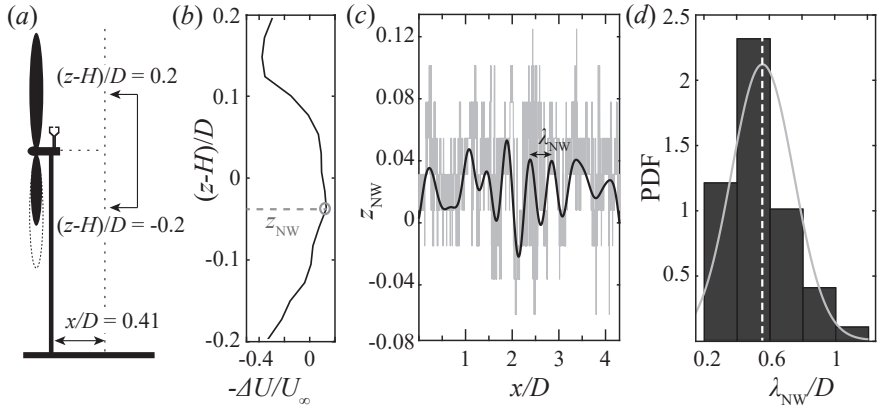

Figure 4.4: (a) Schematic illustrating the region of the velocity profile selected for the investigation of hub wake meandering. (b) Sample velocity profile section with the location of the nacelle wake center, z_{NW}, defined by the maximum velocity within this region, indicated by a gray circle and a horizontal dashed line. (c) A sample unfiltered (light gray) and filtered (black) sequence of nacelle wake position as a function of downstream distance as calculated using Taylor's hypothesis. The distance between adjacent peaks and troughs defines the local wavelength, λ_{NW}. (d) The PDF of the nacelle wake meandering wavelength over the entire dataset, fitted with a normal distribution (light gray line). The mean value is $\langle \lambda_{\mathrm{NW}}/D \rangle = 0.55$, indicated by a vertical dashed line, and the standard deviation is 0.19.

In addition, as shown in figure 4.5, the entire nacelle wake has been observed to shift upward and downward for persistent periods of time during our measurement. This phenomenon, referred to as nacelle wake deflection, is characterized using the time variation of z_{NW}, filtered using a 30-second moving average (the filtered signal is defined as $\widetilde{z}_{\mathrm{NW}}$). The filter is applied to remove the meandering effect described above and to reflect the persistence of the deflection throughout the streamwise span of the FOV. Figure 4.6 shows the relationship between nacelle wake deflection and turbine yaw error, defined as the difference between incoming wind direction and nacelle direction. The nacelle wake deflection is positively correlated with yaw error, with a correlation value of $R = 0.3$ (figure 4.6a). The correlation is weakened by constantly

changing conditions in the field, i.e., incoming wind speed, misalignment angle, incoming turbulence, etc. However, when conditions are stable, the correlation is clearly visible in a sample time series (figure 4.6b). In the three-minute sequence in figure 4.6(b), the solid line represents the smoothed vertical nacelle wake position, defined by the location of the velocity maximum as in figure 4.4(b). When this is greater than 0, the nacelle wake is above the nacelle, and when this is less than 0, the nacelle wake is below the nacelle. The dashed line in figure 4.6(b) represents the yaw error. The relationship between yaw error and vertical nacelle wake position can again be explained by the nacelle's geometric resemblance to an Ahmed body. Wind tunnel studies of Ahmed bodies have shown that, under yawed conditions, the pressure distribution across the body causes the vortices shed behind the body to be deflected upwards on the leeward side and downwards on the windward side [89, 90]. The light sheet in the current study is on the leeward side when yaw error is positive, causing an upward nacelle wake deflection, and on the windward side when yaw error is negative, causing a downward deflection.

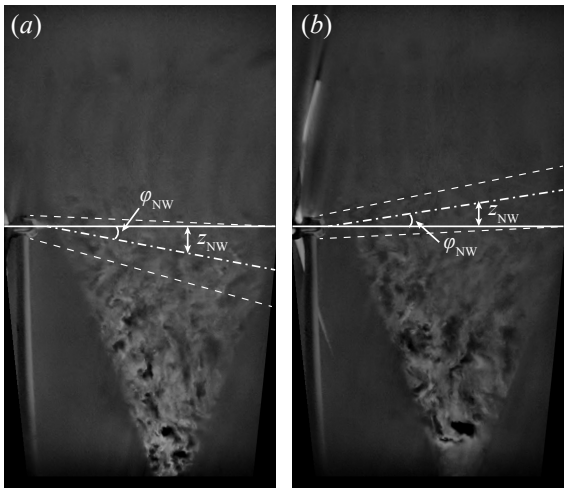

Figure 4.5: Sample snapshots of the snow void patterns in the turbine near wake showing the (a) downward and (b) upward deflection of the nacelle wake with respect to the elevation of the turbine nacelle. The approximate centerline (dash-dotted line) and the boundary (dashed lines) of the nacelle wake are highlighted in the figure, as well as the nacelle wake deflection angle (φ_{NW}) and the nacelle wake height at $x = 0.41D$ (z_{NW}).

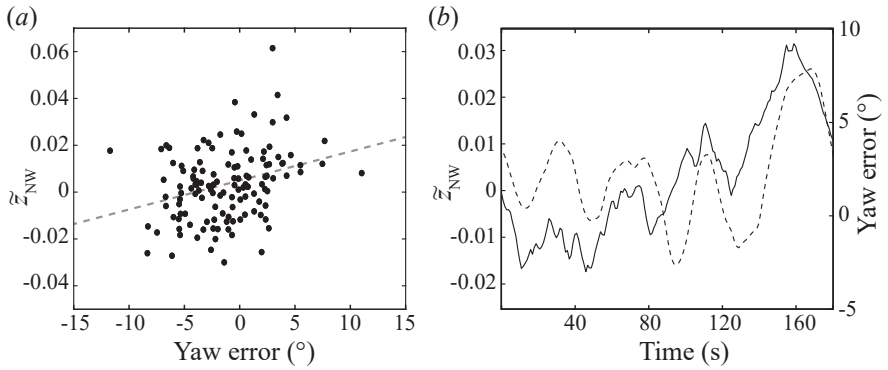

Figure 4.6: (a) Scatter plot showing the relationship between yaw error and vertical nacelle wake position. Each data point represents 30 seconds of data. The dashed line shows the linear regression of the data. (b) A sample three-minute time sequence showing the correspondence between nacelle wake position (solid line) and yaw error (dashed line).

4.3.2 Tower wake

The characteristics of coherent structures shed from the tower are investigated using spectral analysis of the streamwise velocity vectors. Premultiplied frequency spectra are calculated at three different locations in the wake, indicated by I, II, and III in figure 4.7(a). Location I is below the top blade tip and above the hub, II is below the hub and above the bottom tip, and III is below the bottom tip. The vectors used to calculate the spectra are all taken at $x/D = 0.41$, as in figure 4.4. The spectra are calculated over 30-second windows to account for changing parameters such as wind speed, wind direction, hub speed, etc. Figure 4.7(b) shows sample premultiplied spectra for each location, with a gray circle and dashed vertical line marking the location of the most prominent peak. The peaks of the spectra for all the time windows in the dataset are combined into PDFs, shown in figure 4.8 for each location. Each PDF is fit with a bimodal normal distribution to clarify the trends. These distributions reveal peaks within two frequency ranges, indicated by dark and light gray bands in the figure. At the location above the hub (I), the distribution contains a single peak within the blade pass frequency band during the time period of our measurements, indicated by the light gray band and within the range of 0.52-0.74 Hz. This frequency band corresponds to a rotor speed of 10.5-14.8 RPM and tip speed ratio of 7.5-12.1. The prevalence of this frequency is

caused by the structures shed from the blades in the upper half of the wake. Below the hub but above the bottom tip (II), a second frequency emerges corresponding to tower vortex shedding at $St = 0.2$, matching the Strouhal number of the vortex shedding behind a cylinder at high Reynolds numbers (e.g. [91]). The peak of this frequency mode is in the range of 0.22-0.41 Hz, calculated based on a cylinder diameter of 4.1 m and incoming wind speeds within the range of 4.6-8.4 m/s. The signature of the blade pass frequency is still clear at this elevation, but it is significantly weakened by interactions between blade structures and tower structures. Below the bottom tip (III), the signature of the tower vortex frequency is dominant. The blade pass frequency is still visible because of blade tip vortices that are convected below the bottom tip during periods of strong wake expansion. These PDFs indicate that the presence of the tower interferes with the structures shed from the blades, reducing the occurrence of structures at the blade pass frequency. This finding provides evidence for the observation made in the simulation described by Santoni et al. [86] that the tower wake interacts with the blade-shed structures, causing tip vortex breakdown. Their study emphasized the importance of including the tower and nacelle in simulations to accurately model tip vortex breakdown and its significance for wake recovery. Note that conditional sampling for misalignment angle is not applied for this analysis because of the limited amount of 30-second periods that fit the aligned criteria. Therefore, we expect that the trends of the frequency peaks may become clearer when conditional sampling based on yaw error is implemented with more data. Additionally, this method is not used to calculate the frequency of the nacelle wake because the nacelle wake frequency is very low (~ 0.1 Hz), and the 30-second windows used here would not capture enough cycles to provide a strong spectral signal. Therefore the wavelength method described in figure 4.4 was used to quantify the nacelle wake frequency.

4.4 Conclusions and discussion

This study presents the first investigation of the effect of the nacelle and tower on the near wake of a utility-scale wind turbine using super-large-scale particle image velocimetry (SLPIV) and flow visualization with natural snow. The mean flow statistics of the turbulent wake flow field is first examined using 62 minutes of SLPIV data from March

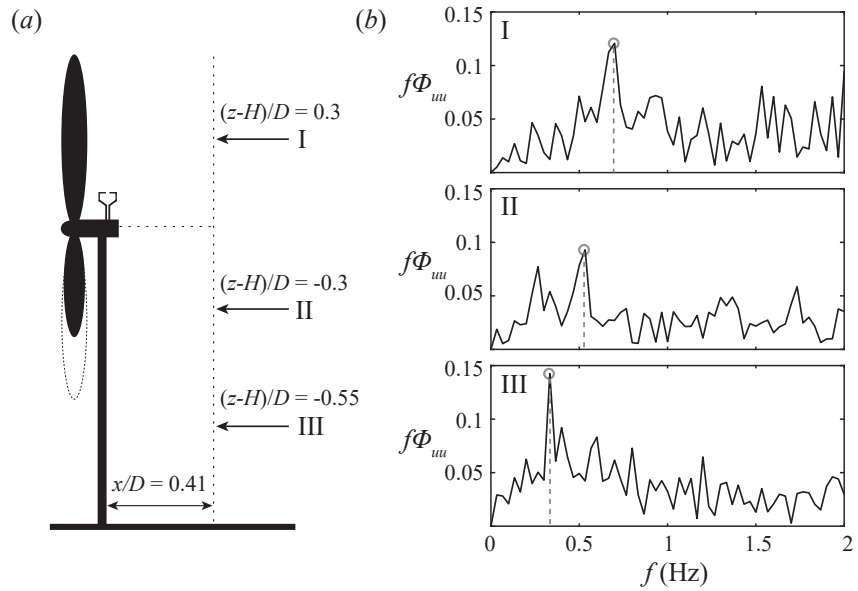

Figure 4.7: (a) Schematic illustrating the locations in the wake where the streamwise velocity spectra are calculated. (b) Sample premultiplied spectra at each wake location – I: Above the hub and below the top blade tip, II: Above the bottom blade tip and below the hub, and III: Below the bottom blade tip. The location of the peak in each spectrum is indicated by a circle and a vertical dashed line.

12th, 2017, with a field of view (FOV) of 125 m (vertical) $\times$ 70 m (streamwise) centred 0.41D downstream of the turbine tower and approximately in the central tower plane (0.06D spanwise offset).

Snow voids reveal coherent structures shed from the blades, nacelle, and tower. A distinct difference in flow pattern is observed above and below the hub due to the strong interaction between the tower and blade-generated vortices below the hub. The nacelle vortex, distinct from the blade root vortices, is visible in the region directly behind the nacelle. The nacelle wake meandering frequency is quantified and shown to match the frequency of vortex shedding from an Ahmed body ($St = 0.06$). Persistent nacelle wake deflection is also observed and found to be strongly connected with the turbine yaw error. Finally, the temporal characteristics of the tower-affected wake below the hub are quantified. The co-presence of two dominant frequencies is observed, one corresponding to blade vortex shedding at the blade pass frequency and the other corresponding to

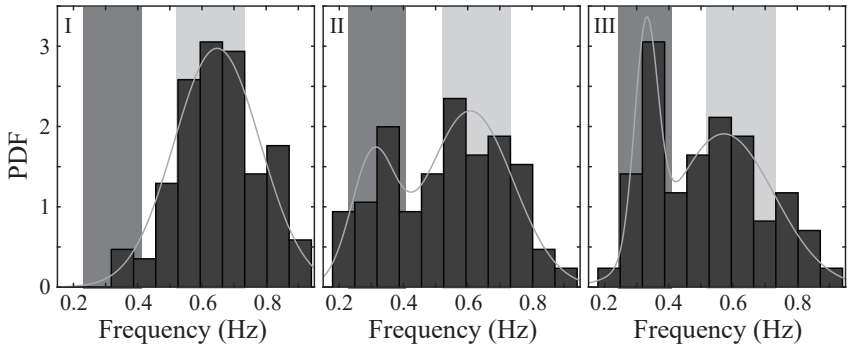

Figure 4.8: PDFs of the frequencies at each of the three wake locations described in figure 4.7 fit with bimodal normal distributions (light gray line). The dark gray and light gray bars indicate the frequency regions corresponding to tower vortex shedding and blade pass frequency, respectively.

tower vortex shedding at $St = 0.2$. The dominance of each frequency varies with elevation.

The high-resolution field-scale data presented in this study highlights the significance of the development of the nacelle and tower structures for the near-wake flow field. Such information should be incorporated into near-wake models to improve our prediction of wake growth. Additionally, our study suggests that the factors influencing nacelle wake meandering may be different for field scale turbines than model scale turbines where the nacelle size is larger relative to the rotor diameter. Our field measurement suggests that the nacelle wake meandering in the near wake may be more associated with the vortex shedding from the nacelle structure rather than the interaction with vortices shed from the blades, which could become more significant as the nacelle wake expands downstream. The nacelle wake is also significantly influenced by yaw error, suggesting the need to consider the yawed condition of the turbine in the modelling of nacelle wake behavior. The factors influencing nacelle wake behavior are especially important because the nacelle wake has been shown to significantly influence downstream whole wake meandering in laboratory-scale studies [25, 82, 83], whereas its influence at the field scale is not yet fully understood. With significantly higher spatial and temporal resolution, our measurements are able to provide detailed flow features that are not available from other state-of-the-art field measurement techniques (e.g., lidar, sodar,

radar, etc.). Our study can provide a link between these features and the large-scale wake behavior investigated in other field scale studies, elucidating the mechanisms that influence wake development under given conditions. By linking the measurement of near-wake structures with far-wake measurement, wake growth and recovery can be predicted more accurately. Additionally, our study can inform laboratory-scale experiment design. The results of our study have reinforced the importance of accurately modelling the field-scale turbine geometry including accurately scaling the nacelle and tower.

We acknowledge our results are limited by the inherent variability of field data and the restrictions it places on analysis techniques (e.g., conditional sampling, spectral analysis, etc.). Moreover, it is worth noting that the present data is limited to a single set of atmospheric conditions, while changes in these conditions such as wind speed, boundary layer stability, and atmospheric turbulence have been shown to significantly influence wake behavior by laboratory scale and LES studies [92, 75, 32]. Particularly, some of variabilities of the nacelle and tower flow structures observed in our current measurements are connected with the effect of coherent structures in the incoming atmospheric boundary layer. Such influence of incoming conditions could be assessed in future studies by simultaneously capturing incoming and near-wake flow fields with SLPIV. Finally, previous studies have shown that turbine operation (e.g. changes in blade pitch, [5]) also affects whole wake and blade-generated coherent structure behavior, so future studies can continue to explore the influence of turbine operation on tower and nacelle-induced structures.

Chapter 5

Dynamic wake modulation induced by utility-scale wind turbine operation

The content of this chapter has been published by the author in *Applied Energy* [3]. Content has been reprinted here with permission.

5.1 Introduction

Wind turbine wakes, the regions of slower and more turbulent air behind turbines, can lead to significant power loss within [57] and even between adjacent wind farms [93]. Therefore, an improved understanding of the utility-scale wind turbine wake and its development is critical for the optimization of wind farm layout and controls. One of the most important aspects of wake development is wake recovery, i.e., the return of the region downwind of the turbine to ambient flow conditions, caused by re-entrainment of momentum through mixing with the surrounding flow. This process is critical for increasing the amount of kinetic energy available for downwind power generation based on large-eddy simulations [94], wind tunnel experiments [95], and analytical studies [96]. It has been well recognized that several factors, including the breakdown of vortex structures shed from the blades [24], the size and spacing of the turbines [22], and the

stability of the atmosphere [97, 98], influence wake recovery. However, dynamic wake modulation, referring to large-scale dynamic motion of the wake, including instantaneous wake expansion and deflection, can also significantly affect its recovery, but has not yet been explored. This phenomenon is typically induced by constantly changing turbine operation and incoming flow conditions associated with utility-scale turbines in the field. Specifically, the amount of wake expansion is determined by axial induction, i.e., the change in streamwise velocity when the flow passes through the rotor, which is in turn a function of the turbine thrust coefficient. Therefore, the changes in axial induction due to variations in incoming flow and turbine operation can induce instantaneous fluctuation in the wake expansion angle. In the extreme case, wake contraction can occur when the turbine undergoes changes in blade pitch [5], significantly affecting the extent of the wake and the rate of wake recovery. Wake deflection occurs when a turbine is operating with yaw error, i.e., when the rotor direction is not aligned with the wind direction, and a spanwise force (parallel to the ground and perpendicular to the wind direction) is exerted on the wake, causing it to deflect in the spanwise direction [1, 99]. Similar to wake expansion, the deflection angle of the wake can also fluctuate in response to changing wind direction, which enhances mixing and modifies the characteristics of wake recovery.

Although a significant number of wake studies (for example, simulations by Jiménez et al. [1], Fleming et al. [100], and Annoni et al. [101]; wind tunnel studies by Grant et al. [102], Haans et al. [103], and Chamorro and Porté-Agel [75]; field tests by Fleming et al. [99], Smalikho et al. [104], Aitken et al. [105], Mirocha et al. [106], Machefaux et al. [107], and Bromm et al. [108]) have been conducted to understand the wake behavior under different wind conditions, very few have accounted for the effect of dynamic wake modulation on wake development. The reason is that such instantaneous changes in conditions are difficult to model on the laboratory scale and in simulations, and the associated instantaneous change of wake characteristics cannot be captured with conventional field measurement techniques (e.g., lidar, radar, sodar, etc.) due to their lack of sufficient spatial and temporal resolution. Nevertheless, some studies have investigated the effect of changing turbine operation and flow conditions on wake behavior. Specifically, continuous regulation of axial induction through blade pitch and generator torque [109, 110] or thrust coefficient [111] to maximize overall wind

farm power generation has been investigated. However, these studies only accounted for the changes in wake velocity, and not for changes in wake expansion and their effect on wake mixing. More recently, Munters and Meyers [112] and Yilmaz and Meyers [113] optimized the time sequence of thrust coefficients of in-line turbines to minimize wake effects on the downwind turbines. Both studies found that certain time sequences caused the wake to breakdown before reaching the next turbine, but they did not quantify the flux or investigate the effect of changes in thrust coefficient that occur during normal utility-scale turbine operation. For wake deflection caused by changes in wind direction, the current state-of-the-art assumes the wake is released from the rotor and passively advected by large-scale turbulence [114, 115]. However, the wake is not a passive tracer; rather, the turbine actively modulates the incoming flow to influence wake behavior. This simplification could be responsible for the discrepancies between the wake position predicted using the passive tracer model and that observed in field tests [116, 117]. Controlling wakes using yaw error alone [118] and a combination of both axial induction and yaw error [119] have also been proposed as methods for optimizing overall wind farm performance, with preliminary success in field tests [120]. However, to implement these strategies most effectively, we need to first understand the impact on wake behavior of the constantly changing flow and turbine operational conditions present in the field.

Consequently, here we present the first investigation of the phenomenon of dynamic wake modulation and its connection with instantaneous variation of incoming flow and turbine operation. This study was made possible through the implementation of super-large-scale flow visualization using natural snowfall, described in detail in Toloui et al. [4], Hong et al. [17], Nemes et al. [20], Heisel et al. [19], Dasari et al. [5], and Abraham et al. [49]. This technique was first developed to characterize the atmospheric boundary layer [4] and the near-wake of a utility-scale wind turbine [17] through imaging the motion of individual snowflakes in a field of view on the order of 10 m, providing unprecedented spatial and temporal resolution in comparison to state-of-the-art field measurement techniques. It was later extended to measure the flow field in the entire span of the turbine wake on the order of 100 m through tracking the motion of patterns of snowflakes representing vortices that are advected by the flow [5, 49]. Here we again take advantage of the visual patterns created by vortical flow structures in snow to thoroughly characterize dynamic wake modulation by a utility-scale turbine.

5.2 Methods

The experiment took place between 19:00 and 22:00 CST on January 22nd, 2018, at night during a snowstorm. The atmospheric and incoming wind conditions during the experiment were recorded using the met tower and SCADA system. The temperature at hub height stayed relatively constant between -3.8°C and -3.5°C, and the variation in temperature between the bottom and top of the wake was approximately 0.8°C. The incoming wind speed varied significantly over the course of the experiment, with instantaneous values between 2 m/s and 17 m/s at the hub, allowing the characterization of the wake under different turbine regions of operation. The wind direction also varied between approximately -30° and 20° clockwise from North. According to the wind direction, the met tower was in the wake of the turbine throughout this time period.

In the current study, a light sheet was used to illuminate the snowflakes in a plane parallel to the rotor (perpendicular to the flow) 17 m ($0.18D$) downstream of the turbine (figure 5.1). A Nikon D600 camera with a 50 mm $f/1.2$ Nikon lens captured the images of snowflakes in a field of view of 73 m × 129 m (spanwise × vertical) for more than 2 hours at a frame rate of 30 Hz and size of 1080 pixels × 1920 pixels. The camera was placed 166 m away from the light sheet and tilted 22.6° with respect to the ground in order to capture the entire vertical rotor span.

Coherent vortex structures in the flow appear as voids in the snow particle seeding projected onto the light sheet due to the centrifugal effect on the inertial particles caused by the strongly rotating fluid [5]. The edges of the voids are determined by the Stokes number, $St = \tau_p/\tau_f$, where τ_p is the snow particle response time and τ_f is the characteristic time scale of the flow [53]. When $St \sim 1$, as in the regions of high circulation within the vortices, the particles are no longer able to track the flow, creating voids in snowflake concentration. Therefore, the circulation threshold represented by the void boundaries depends on the snowflake properties (i.e., size, density), but is on the same order as that observed in [17], $\Gamma \approx 6\text{m}^2/\text{s}$. Image enhancement techniques were used to extract the vortices (described in detail in Appendix A.1), and the images were stacked to reconstruct a three-dimensional visualization showing the changes in the near-wake vortices over time (figure 5.2*a*). The reconstruction demonstrates the significantly different flow features below and above the hub height. Below the hub, strong interactions

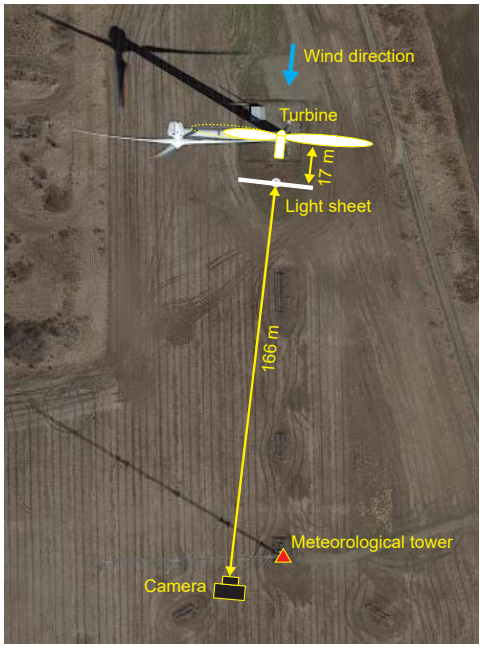

Figure 5.1: Google map of the field site with relevant features highlighted. System components for super-large-scale flow visualization using natural snowfall (i.e., camera and light sheet) overlaid along with relevant distances.

are observed between the vortices shed from the blades and those shed from the tower. Above the hub, the characteristic vortex helix shed from the rotating turbine blade tips (figure 5.2*b*) is more clearly visible. Here the wake modulation becomes more evident since the tip vortex helix is not affected by the tower vortices. Therefore, an envelope was fit to the upper boundary of the portion of the blade tip vortex helix above the hub to capture the overall shape of the wake (figure 5.2*c*). Cross-sections of this envelope were compared to the boundary of the wake with no expansion or deflection included (referred to as the model wake hereafter), extracted from a SolidWorks model of the experimental setup. This process is described in detail in Appendix A.2. The shift between the observed wake shape and the model wake shape was decomposed into vertical and spanwise components ($\delta_{w,z}$ and $\delta_{w,y}$, respectively) at each point in time. This decomposition enabled quantification of the degree of dynamic wake modulation. The effect of these behaviors on wake propagation direction and mixing was then explored.

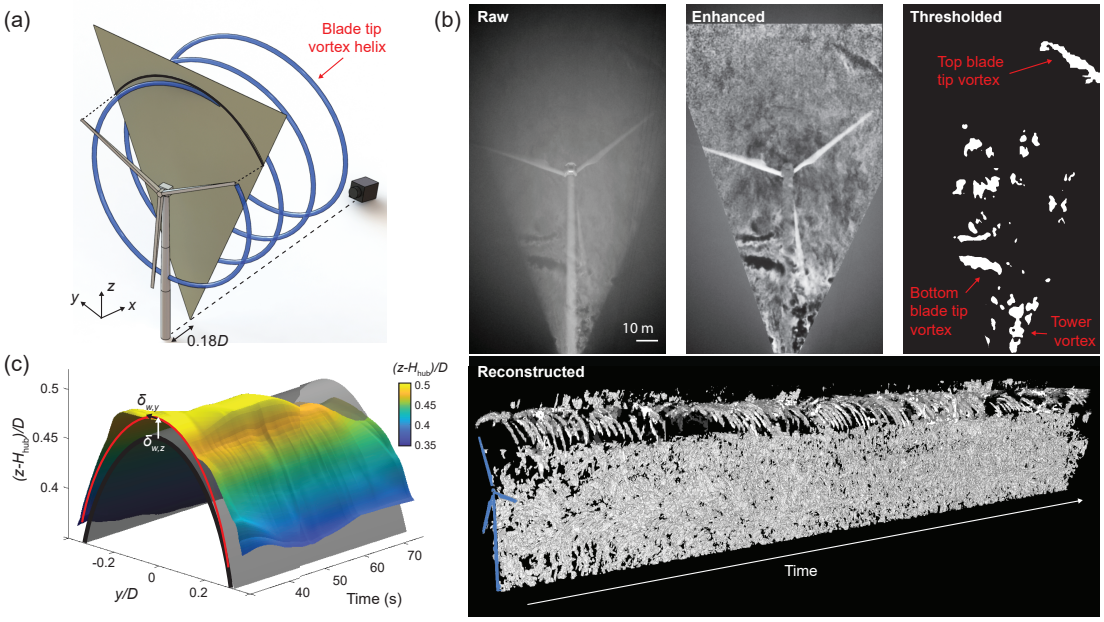

Figure 5.2: (a) Schematic of the experimental setup including the turbine, light sheet, and camera. The blue helix represents the blade tip vortex and the black line indicates the location of the intersection between the model wake and light sheet. The coordinate system is defined, where x is the streamwise direction, y is the spanwise direction, and z is the vertical direction. (b) Image processing steps used to reconstruct instantaneous vortical structures in the near wake, including the raw image, enhanced image, thresholded image, and reconstructed volume. (c) Sample time series of the wake envelope and the model wake position. The red line marks the profile of the shifted wake position least square fit to the experimental data and the arrows indicate the decomposition of the wake shift into vertical and spanwise components ($\delta_{w,z}$ and $\delta_{w,y}$, respectively).

5.3 Results

5.3.1 Intermittency of blade tip vortex formation

When examining the top tip voids in the wake reconstruction, several periods of intermittency are observed where the voids do not appear consistently (figure 5.3a). These periods are identified using the total void area within a time window. The regions with void areas corresponding to the bottom 6% within a period of four blade passes are defined as intermittent. These values were chosen because they provided the clearest separation between intermittency and consistency in the histogram including the entire

data set. Tip vortex intermittency is found to correlate with the incoming wind speed at hub height, U_∞, measured by the sonic anemometer on the turbine nacelle. The distribution of U_∞ during intermittent tip vortex appearance is bimodal (figure 5.3b), corresponding to below rated (region ≤ 2, figure 5.3c) and above rated (region > 2, figure 5.3d) operational regimes. When the incoming wind speed is low (below approximately 10 m/s), the turbine operates in region 2 or below where the control algorithm seeks to maximize the power output by keeping the blade pitch low and nearly constant, maximizing the lift on the airfoils. In these regions, periods of intermittency occur when the wind speed and correspondingly, power production (P_{wt}), are lower (figure 5.3e), because the blades generate less circulation at lower power, producing weaker tip vortices [17]. Above region 2, the blade pitch angle (β) increases with increasing wind speed to regulate the rotor speed and limit the loads experienced by the turbine structure. In these higher regions, periods of intermittency occur at higher values of U_∞ and β (figure 5.3f), consistent with the observations of Dasari et al. [5]. This trend can be explained by the decay of tip vortex strength in response to decreasing angle of attack caused by increasing blade pitch. More importantly, our results highlight the potential benefit of using information provided by the SCADA system to directly predict the occurrence of tip vortex intermittency with statistical certainty. These periods of intermittency have implications for wake recovery, as tip vortex breakdown enhances mixing [24]. Wind speed, blade pitch, and power output measurements are readily available to the turbine controller, so the knowledge of the relationship between these variables and the behavior of the tip vortices in specific regimes can be incorporated into wind farm optimization, enabling the direct modulation and prediction of wake recovery through tip vortex breakdown.

5.3.2 Quantification of dynamic wake modulation

For the analysis of dynamic wake modulation, the periods of intermittency described above are removed in order to extract continuous fluctuations of the wake envelope. Figure 5.4 shows the spanwise wake modulation in response to instantaneous yaw error. In figure 5.4(a), spanwise wake deflection is defined in terms of the displacement along the light sheet plane, $\delta_{w,y}$, and the angle of deflection, $\varphi_{w,y}$, calculated using the distance between the turbine and the light sheet. Figure 5.4(b) shows schematics comparing the

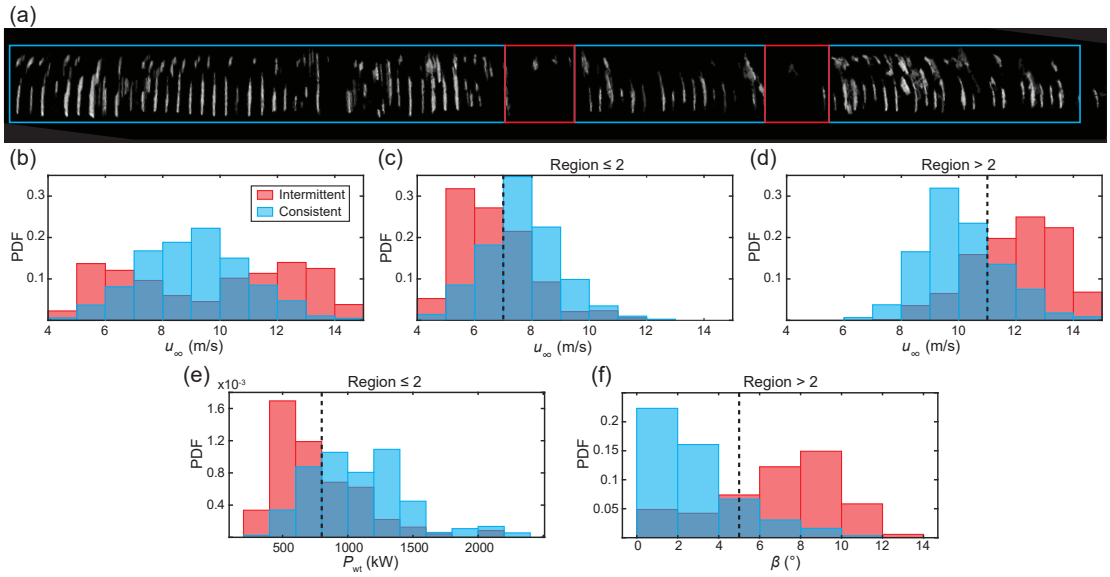

Figure 5.3: (a) Sample sequence of extracted top tip voids, with blue and red boxes marking periods of consistent and intermittent voids, respectively. (b) Histogram comparing the incoming wind speed at hub height during periods of consistent and intermittent tip vortex appearance. (c) Histogram comparing the incoming wind speed during periods of consistent and intermittent tip vortex appearance when the turbine is operating in region 2 or below. (d) Histogram comparing the incoming wind speed during periods of consistent and intermittent tip vortex appearance when the turbine is operating above region 2. (e) Histogram comparing the turbine power during periods of consistent and intermittent tip vortex appearance when the turbine is operating in region 2 or below. (f) Histogram comparing the blade pitch during periods of consistent and intermittent tip vortex appearance when the turbine is operating above region 2.

wake deflection trends in response to steady yaw error and instantaneous yaw error. Under steady yaw error, the wake steering angle,

$$\xi = \varphi_{w,y} - \gamma, \tag{5.1}$$

where γ is the yaw error, is positively correlated with γ [1]. However, under the constant wind direction changes in the field that cause instantaneous yaw error, ξ is negatively correlated with γ with a correlation coefficient of -0.42 (figure 5.4c). According to the numerical simulation from Leishman [121], such opposite deflection can occur in the near wake of the turbine due to the fact that spanwise wake deflection takes time to stabilize under sudden changes in yaw error. Our results further suggest that, when

the yaw error is short-lived as it is under the constantly changing wind conditions in the field, instantaneous wind direction changes can cause significant disturbance to the process of the wake transitioning to the fully deflected state it experiences under steady yaw error. In addition to the inverse statistical relation compared to the steady yaw error condition, a sample time sequence also clearly shows the opposing trend of γ and ξ (figure 5.4d). More remarkably, the same inverse relationship between γ and ξ is observed (with a correlation coefficient of -0.35) when $\varphi_{w,y}$ is obtained from the spanwise velocity recorded at the met tower which, due to the northerly wind direction, is in the wake of the turbine $1.77D$ downstream. This observation indicates the persistence further downstream of the disturbance of the spanwise wake deflection in the near wake induced by the constantly changing wind direction. To provide an assessment of the impact of spanwise dynamic wake modulation on wake position downstream, we consider the maximum steering angle caused by instantaneous yaw error, about 15° in this dataset. At $6D$ downstream, this steering angle corresponds to a $1.6D$ offset from the rotor axis. This shift in wake direction is significant compared to the study conducted by Vollmer et al. [115], which found that wind direction fluctuations cause changes in wake direction up to $0.5D$ at $6D$ downstream when the wake is modelled as a passive tracer under neutrally stratified atmospheric conditions. Therefore, our results show that dynamic wake modulation has a significant effect on wake propagation direction. More importantly, we are able to demonstrate that the instantaneous yaw error, available from the SCADA system of current utility-scale turbines, is strongly correlated with the spanwise wake modulation and can be used to predict wake steering and meandering downstream with statistical certainty.

Figure 5.5 shows the vertical wake modulation response to dynamic turbine operation. In figure 5.5(a), vertical wake modulation is defined by $\delta_{w,z}$, displacement along the vertical direction, and $\varphi_{w,z}$, the angle of vertical deflection. It should be noted that, because only the top half of the wake is measured, the vertical modulation reported here is a combination of wake expansion and vertical deflection of the wake centerline. figure 5.5(b) compares a sample time series of vertical wake modulation to blade pitch (β) and tip speed ratio (λ), showing a negative relationship with β (correlation coefficient of -0.74 when the turbine is operating above region 2) and a positive relationship with λ (correlation coefficient of 0.58). The combination of these two parameters determines

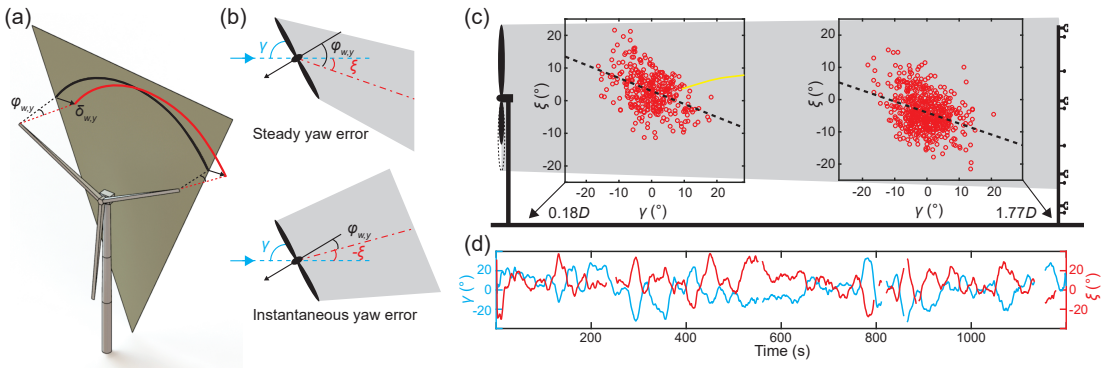

Figure 5.4: (a) Schematic showing how spanwise wake modulation is quantified. (b) Diagrams of (top) average wake deflection under steady yaw error and (bottom) instantaneous deflection under instantaneous yaw error. (c) Instantaneous spanwise wake deflection at two different locations downstream of the turbine: the light sheet position $0.18D$ downstream (left) and the met tower $1.77D$ downstream (right). Each red data point represents an average over 20 s of data, corresponding to the smoothing window applied to the wake envelope. The black dashed lines are least squares best fit lines and the yellow line is the trend for steady yaw wake deflection from Jiménez et al. [1]. (d) Sample time series showing yaw error, θ, and wake steer, α, captured at the light sheet location.

the thrust coefficient, C_T [122], which is shown in figure 5.5(c) to correlate strongly with $\varphi_{w,z}$ (correlation coefficient of 0.74). This relationship suggests that vertical wake modulation is largely contributed by wake expansion caused by instantaneous changes in axial induction, which is a direct function of the thrust coefficient. This characteristic of vertical wake modulation enables the direct prediction of its behavior through blade pitch and tip speed ratio, which are readily available from SCADA data. Such prediction of vertical wake modulation can significantly improve the estimation of kinetic energy available for power generation, as thoroughly discussed in the section below.

Occasionally sudden decreases in vertical wake modulation are observed (figure 5.5d). These appear to occur when the wind speed is high (above approximately 13 m/s) and the turbine is operating in region 3. In this region, the control algorithm attempts to maintain the rotor speed at the rated level by adjusting the blade pitch. When the rotor speed increases past the rated value (these periods are indicated by gray bars in figure 5.5d), the control algorithm must slow it down, injecting energy back into the wake and causing an abrupt reduction in expansion. As our results show, this aspect of

vertical wake modulation behavior is strongly dependent on the region of turbine operation and the control parameters recorded by the SCADA, enabling accurate prediction of this phenomenon and its effect on wake recovery.

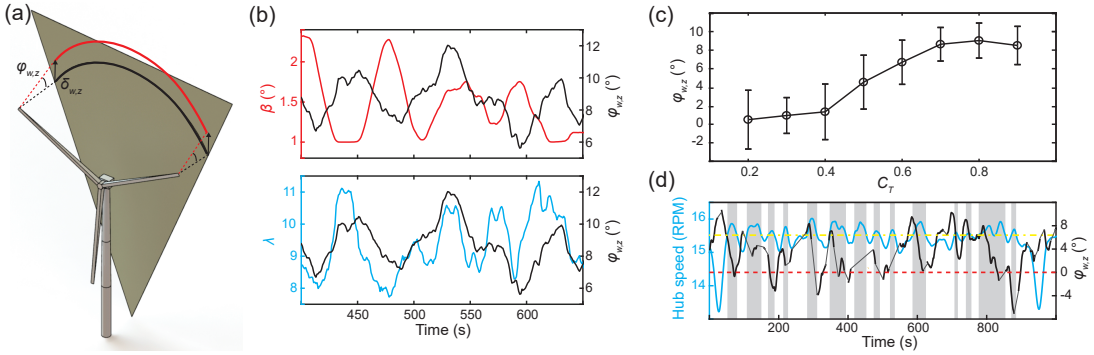

Figure 5.5: (*a*) Schematic showing how vertical wake modulation is quantified. (*b*) Sample time series showing vertical wake modulation with (top) blade pitch and (bottom) tip speed ratio. (*c*) Plot showing the relationship between turbine thrust coefficient and vertical wake modulation. The circles represent the mean value of $\varphi_{w,z}$ for each value of C_T, while the vertical bars show the standard deviation. (*d*) Sample time series of hub speed and vertical wake modulation. Gray bars indicate periods where the hub speed is above the rated speed, 15.5 RPM, also indicated by a dash-dotted brown line. The red dashed line shows where the vertical wake modulation crosses zero. The thinner gray lines connecting the thick black lines represent vertical wake modulation data linearly interpolated through periods of intermittency, included to facilitate visualization.

5.3.3 Influence on wake recovery

To quantify the effect of dynamic wake modulation on the energy flux into the wake, a modified version of the streamtube method implemented by Lebron et al. [123] is employed. Rather than a constant control volume, a moving and deforming control volume is used to capture the wake motion, where the boundary of the streamtube is the boundary of the wake, demarcated by the blade tip vortices. In a large wind farm, flux caused by the Reynolds shear stress is the main contributor to energy re-entrainment and wake recovery according to simulations [94] and laboratory-scale experiments [95, 123, 124]. To quantify the contribution of wake deformation to this term in the energy balance, the vertical and spanwise wake deflection velocities are calculated (figure 5.6*a*), and their fluctuating components are used along with the incoming and wake streamwise

velocities from the SCADA and met tower, respectively, to calculate the corresponding flux terms,

$$\Phi_y = \overline{u}_x \langle u'_x v'_y \rangle, \Phi_z = \overline{u}_x \langle u'_x v'_z \rangle. \tag{5.2}$$

The details of this calculation are described in Appendix A.3. These components of flux, normalized by the cube of the incoming wind speed, are plotted over the duration of the dataset in 5.6(b). The contribution of each component varies with the region of operation. When the turbine is operating in region 3, the vertical energy flux induced by the vertical wake modulation is the main contribution to the total flux. In this region, as explained above, the regulation of the rotor speed causes abrupt changes in vertical wake modulation. In region 2, where less power is produced, the total flux caused by dynamic wake modulation is at its minimum due to the diminishing difference in velocity between the wake and the surrounding freestream flow. In region 2.5, the axial induction, calculated as

$$a = \frac{\overline{u}_{x,\text{freestream}} - \overline{u}_{x,\text{wake}}}{\overline{u}_{x,\text{freestream}}}, \tag{5.3}$$

where $\overline{u}_{x,\text{freestream}}$ is obtained from the SCADA and $\overline{u}_{x,\text{wake}}$ from the met tower at hub height, reaches a maximum in this region as shown in figure 5.7. The vertical and spanwise components of modulation contribute nearly equally to the flux in this region.

In figure 5.6(c) the flux caused by dynamic wake modulation is compared to the total, vertical, and spanwise energy flux into the wake calculated using large eddy simulation by Cortina et al. [2] for an isolated turbine in a neutrally stratified atmosphere. Though the turbine and ambient conditions in the current study are not identical to those described by Cortina et al. [2], the case is the most similar available in the literature, with turbine diameters within 4% and mean wind speeds within 6%. Therefore, the case has sufficiently similar conditions to serve as a baseline for approximate comparison to demonstrate the relative importance of dynamic wake modulation on wake mixing and recovery. This plot shows that vertical flux caused by dynamic wake modulation can be up to 50% of the vertical energy flux calculated using the velocity components alone. In a large wind farm where a fully developed wind farm boundary layer has formed, the wake mixing that supplies energy to downwind turbines is primarily determined by vertical kinetic energy flux, as the energy in the horizontal direction has been depleted by the surrounding turbines [94, 95, 96, 123, 124]. Therefore, the enhanced mixing

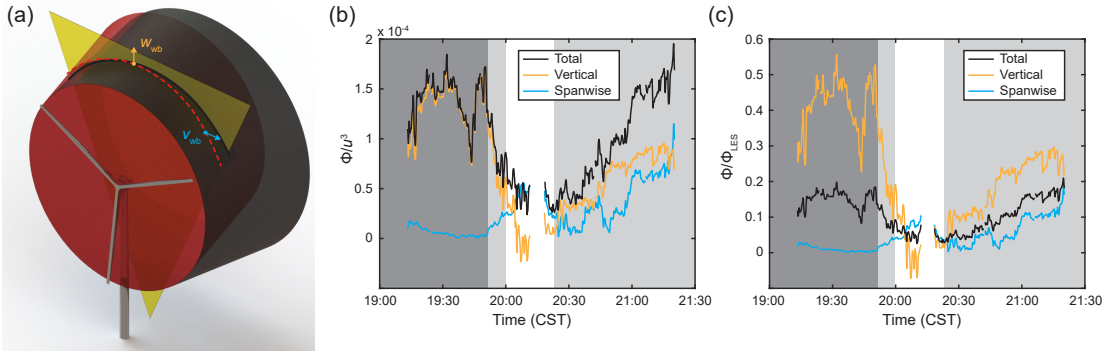

Figure 5.6: (a) Schematic showing wake deflection velocity in the vertical and spanwise directions. The fluctuating components of these velocities are used to calculate the contribution of wake deformation to energy flux. (b) Plot of the vertical, spanwise, and total wake modulation contributions to energy flux through a wake cross-section, normalized by the cube of the incoming velocity. The dark gray region indicates the time period where the turbine is operating in region 3, light gray in region 2.5, and white in region 2. (c) Plot of dynamic wake modulation contributions to energy flux, normalized by the total flux per unit area in the vertical and spanwise directions reported by Cortina et al. [2] for an isolated wind turbine.

caused by vertical wake modulation can potentially lead to substantial increase of the wind power available in a large wind farm. In the spanwise direction, dynamic wake modulation can cause energy flux up to 10% of spanwise energy flux with no deformation included. Overall, dynamic wake modulation can contribute up to 20% more energy flux and an average of 11% more than that calculated without considering dynamic wake modulation. This additional energy flux has significant implications for wake mixing models, which currently do not account for dynamic wake modulation.

5.4 Discussion and conclusion

Through super-large-scale flow visualization using natural snowfall, we reveal and quantify dynamic wake modulation for the first time, which cannot be captured with any other existing techniques. This data is captured at unprecedented spatiotemporal resolution in the wake of an operational utility-scale turbine, and includes flow visualization

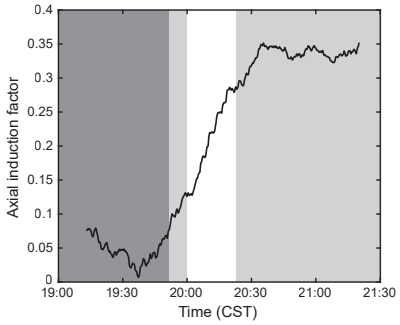

Figure 5.7: Change in axial induction factor, calculated as in equation 5.3. The background shading indicates the region of operation of the turbine during each time period. The dark gray region indicates the time period where the turbine is operating in region 3, light gray in region 2.5, and white in region 2.

over a 2-hour time period containing multiple regions of turbine operation and wind conditions. In the future, this high-resolution data can be used to validate numerical simulations of utility-scale wind turbine near wakes. Applying this visualization technique in the plane parallel to the rotor allows us to decompose the dynamic wake modulation into two components: spanwise and vertical. Each component contributes differently to the wake evolution. The spanwise component is dependent on instantaneous yaw error and significantly affects the variability of the wake propagation direction, which is important for wind farm control schemes relying on wake steering. It should be noted that our results do not contradict the well-established behavior of wake steering as reported in many previous studies. Rather, these instantaneous deflections would be superimposed on top of any mean wake deflection, increasing the fluctuations in wake position. Although the current study only captures part of the blade tip vortex helix, preventing the differentiation between wake expansion and vertical centerline deflection in the vertical component, future snow visualization measurements can be designed to capture a more complete section of the wake by expanding the light sheet and increasing the spotlight intensity. Nevertheless, the relationship between vertical wake modulation and thrust coefficient, which is related to turbine axial induction, suggests wake expansion provides the main contribution to the vertical component. Both spanwise and vertical wake modulations influence wake recovery, crucial for accurate modelling of wind farm power output, by enhancing mixing at the wake boundary. Modulation in the vertical

direction is particularly important for large wind farms where most energy is entrained from above the farm, so the ability to control this behavior would be highly beneficial for wind farm optimization.

Significantly, dynamic wake modulation is directly dependent on parameters that are already being measured by the turbine, so it can easily be integrated into the control algorithms of existing wind farms. These relationships suggest that the parameters that determine dynamic wake modulation (e.g., blade pitch) can be modified to enhance wake mixing and provide more power to downwind turbines. For example, blade pitch is already used to control the turbine loading under rapidly changing wind conditions. Further, Gebraad et al. [122] discuss the potential of using changes in blade pitch to regulate the thrust coefficient for the purposes of axial induction control without significantly reducing the power coefficient. Therefore, blade pitch could also be used to control dynamic wake modulation with the goal of enhancing wake mixing and recovery to improve the overall energy extraction efficiency of the entire wind farm. Data mining and machine learning, as proposed by e.g., Wan et al. [125], Park and Law [126], and Howland and Dabiri [127], can be employed in the future to provide more accurate and robust predictions of wake behaviors in response to changing atmospheric and operation conditions that can be integrated into utility-scale turbine controllers. Models that have been proposed for wind farm control using, for example, wake steering [118] or axial induction control [111], will need to include an increased standard deviation to account for the variability in wake behavior caused by dynamic wake modulation. Undoubtedly this standard deviation will depend on the specific turbine and atmospheric conditions, but the presented results can provide an order-of-magnitude guideline for the amount variability the wake exhibits.

The presented results will affect the implementation of wake models developed by e.g., Jensen [128] or Bastankhah and Porté-Agel [129] which depend on thrust coefficient. In general, our study shows that wake expansion will be larger than predicted by wind tunnel studies or simulations that do not account for dynamic wake modulation. To fully capture the dynamic wake behavior of utility-scale wind turbines, our results provide strong support for a dynamic wake model like the one proposed by Shapiro et al. [130]. Our results indicate that the wake expansion is directly dependent on the instantaneous thrust coefficient, which can be derived from the tip speed ratio and blade pitch, both

readily available to the turbine controller. Therefore, a dynamic wake model must include a time-dependent thrust coefficient rather than a constant averaged value.

Additionally, dynamic wake modulation can be incorporated into layout design decisions for future wind farms. Meyers and Meneveau [131] conducted an analytical optimization of wind turbine spacing and found that cost effectiveness is maximized when turbines are spaced 15 rotor diameters apart, which is significantly higher than the current standard for turbine spacing. However, their study was based on top-down models that account for the effect of wake turbulence on mixing in the wind turbine boundary layer [94, 132], but do not include the additional mixing caused by dynamic wake modulation. To include mixing caused by dynamic wake modulation, the wake eddy viscosity (ν_w) in these models could be increased, and to reflect the effect of changes in operational conditions, a dynamic eddy viscosity value that changes in time should be used. If this additional mixing were included, the wind speed experienced by the wind farm would increase, decreasing the necessary spacing. The idea that enhanced mixing can decrease spacing is confirmed by the computational study conducted by Santhanagopalan et al. [133] which found that increasing the incoming flow turbulence intensity decreases the optimal turbine spacing in a single turbine column. Additionally, Meyers and Meneveau [131] found that when the turbines are operating in region 3, the optimal spacing decreases due to a decrease in thrust coefficient and a corresponding increase in boundary layer wind speed. This finding suggests that changing the wake behavior can allow closer turbine spacing. Controlling dynamic wake modulation could be one way to expedite wake recovery and reduce the optimal turbine spacing, enabling more efficient land area use.

In the current study, we validate our near-wake findings with data from the met tower at almost 2 rotor diameters downstream, but future work can be done to understand the propagation of observed features farther downstream. Observing these behaviors at a distance similar to turbine spacing in a wind farm (6-8 rotor diameters downstream) would be beneficial for quantifying their effects on downwind turbines, and can be achieved through simultaneous measurements with other conventional field measurement techniques (e.g., lidar). Additionally, further investigations of dynamic wake modulation under different atmospheric stabilities would provide insights into the variability of wake behavior over the diurnal cycle. Future work should also be done to

integrate the findings of this study into numerical simulations. The omission of mixing caused by dynamic wake modulation from top-down models could be partially responsible for the underestimation of the power output of large wind farms such as the Horns Rev wind farm in Denmark [134]. By incorporating dynamic wake modulation into wake models, wind farm power output can be predicted more accurately and optimized more effectively, helping wind energy become a more economical renewable energy option.

Chapter 6

Mechanisms and timescales of dynamic near-wake modulation

The content of this chapter is under review for publication by the author in *Journal of Fluid Mechanics*.

6.1 Introduction

Utility-scale wind turbines operate in highly stochastic atmospheric conditions and are subject to constant changes in wind speed, direction, and turbulence. Simplified models of these conditions can be developed, but they cannot be fully replicated in the laboratory or in simulations. Moreover, turbine operation (e.g., blade pitch, rotor speed, yaw angle) is constantly adapting to these changes, further increasing the complexity of the fluid-structure interactions they experience. Improved understanding of these dynamic interactions is essential for continued increases in turbine size and efficiency [134, 135, 8].

Dasari et al. [5] first explored the effect of changes in blade pitch on the wake of a 2.5 MW wind turbine in the field, finding significant impact on wake expansion and blade tip vortex behaviour. Another recent field-scale study investigated the effect of dynamic conditions, including wind direction, blade pitch, and tip speed ratio (ratio of the speed of the blade tips to the incoming wind speed), on the wake of the same 2.5 MW turbine [3]. Using super-large-scale flow visualization with natural snowfall, this investigation

revealed the significant impact of changes in atmospheric and operational conditions on wake deflection and expansion, termed dynamic wake modulation. Changes in blade pitch and tip speed ratio were shown to cause fluctuations in the wake expansion angle and, remarkably, dynamic changes in wind direction were found to deflect the wake in the opposite direction of that observed under steady conditions. Furthermore, these dynamic wake behaviours were shown to enhance mixing up to 20%, accelerating wake recovery. While these findings provided many useful insights into wake behaviors in the field, the underlying mechanisms causing these behaviors were not clear due to the inherent limitations of field studies, including the limited field of view and the lack of control over wind conditions.

Laboratory-scale experiments allow for greater control over flow conditions, enabling direct observation of the transient wake response to dynamic conditions. Yu et al. [136] used an actuator disk in a wind tunnel to investigate step changes in thrust coefficient on the loading and wake. They observed an overshoot or undershoot of wake velocity response, depending on the direction of the thrust coefficient change, attributed to passage of the vorticity shed from the disk edge. With a similar setup, Macri et al. [137] studied step changes in yaw angle. They found a lag in wake deflection and thrust coefficient response on the order of the yaw maneuver duration. To investigate the effect of dynamic inflow on turbine blade loading, Schepers [138] implemented step changes in blade pitch on a 2-bladed, 10 m diameter turbine in the NASA-Ames wind tunnel. In this experiment, load overshoots were observed before a gradual approach to the new equilibrium. Berger and Kühn [139] conducted a similar study to investigate the impact of fast changes in blade pitch on a scaled turbine model and its wake. They also recorded overshoot and undershoot of turbine loading in addition to a decaying wake velocity response attributed to flow inertia. Though these experimental studies successfully isolate individual parameters to determine their effect on the wake, the mechanisms causing the wake changes are still not clear due to their inability to directly observe all variables (e.g., vorticity) at all locations around the rotor. Furthermore, the scalability of wind tunnel experiments is limited by constraints on the physical scale and mechanical characteristics of model turbines and the challenge of replicating the complexity of atmospheric flow.

Simulations have the potential to elucidate these mechanisms, as flow and turbine

parameters can be easily controlled and modified, and all variables can be extracted from the domain. A few simulation studies have investigated the effect of dynamic conditions on wind turbine performance and wake behavior. Leishman [121] reviewed the challenges involved in modelling the unsteady aerodynamics of wind turbines, and used dynamic inflow theory to estimate the time constant for flow development through a rotor as 1-1.5 rotor revolutions. This study also showed a qualitative picture of the wake response to a 30° step change in yaw angle using the vortex wake model, demonstrating that it took about 9 rotor revolutions for the wake to fully stabilize. Ebrahimi and Sekandari [140] simulated the effect of step changes in both wind speed and yaw angle on power production and blade loading, finding the timescale for stabilization to be 4-5 s. Finally, Andersen and Sørensen [141] used large eddy simulations (LES) to investigate the power output response to changes in wind speed and direction. They found a lag between peaks in thrust force and peaks in power that they attributed to generator inertia and the timescale of the controller. Further, they observed that the correlations between the turbine loads and the wake position were low, highlighting the highly dynamic behavior of the wake.

In addition to gaining insight into wake behaviors occurring during normal utility-scale wind turbine operation, improved understanding of the dynamic wake is crucial for the design of recently proposed advanced wind farm control algorithms, including thrust optimization [111, 142, 130, 112, 113], yaw angle modification [143, 144, 145, 146, 147], and a combination of the two [119, 148]. For example, Raach et al. [144, 145] used simulations to investigate the effectiveness of a lidar-based closed-loop control framework, and observed a period of inverse wake deflection in response to a 5° step change in yaw angle. Yilmaz and Meyers [113] and Munters and Meyers [112] took advantage of changes in wake width induced by periodic blade pitch changes to induce vortex rings in the wake of a simulated turbine, thereby re-energizing the wake through their interactions. The wind farm optimization conducted by Munters and Meyers [119] yielded similar behaviors for thrust and analogous yaw oscillations that induced wake meandering. The current study employs LES to explore the underlying physical mechanisms behind these dynamic wake behaviors.

The current study focuses on developing the understanding of dynamic wake behaviors, both those occurring during normal utility-scale turbine operation and those that

result from the implementation of adaptive control algorithms. The investigation uses LES to model changes in blade pitch, wind direction, and rotor yaw occurring at different rates. The timescales and mechanisms of the wake response are then described. Section 6.2 describes the simulation methodology and the turbine model, section 6.3 presents the results, and section 6.4 provides the discussion of the results and conclusions.

6.2 Methodology

6.2.1 Large eddy simulations

LES were performed using Nalu-Wind, a wind-focused fork of the incompressible flow solver developed by Sandia National Laboratories, Nalu [14]. Nalu-Wind solves the filtered Navier-Stokes equations using an unstructured finite-volume formulation that is second order accurate in space and time. The deviatoric part of the resolved Reynolds stress tensor was represented using a Smagorinsky model with a Smagorinsky coefficient of $C_S = 0.08$, based on the average of the values computed by the Lagrangian scale-dependent Smagorinsky model. Martínez-Tossas [149] shows that when using $C_S = 0.08$, the turbulence characteristics (e.g., resolved Reynolds stresses) agree well with the results from the more realistic Lagrangian scale dependent model. The timestep of the simulations was chosen to be 0.025 s such that the Courant–Friedrichs–Lewy (CFL) number based on the tip velocity remained below 1. The simulations were conducted using uniform laminar inflow with an incoming wind speed of $U_\infty = 10$ m/s. Uniform inflow was selected to isolate the changes in turbine operation and their effect on the near wake. Previous simulation studies have frequently used uniform laminar inflow to separate deterministic wake behaviors from the effects of turbulent stochasticity [150, 151, 152, 153, 154]. In addition, the near wake (the focus of the current study) is dominated by coherent structures shed from the turbine rather than random turbulence [58]. Previous field-scale studies using high-resolution flow visualization also exhibit the dominance of coherent structures in the near wake [17, 18, 5, 49, 3]. Most importantly, the results of the recent field study investigating the dynamic wake modulation phenomena explored in the current study show that these large-scale near-wake behaviors dominate above atmospheric turbulence [3]. The size of the simulation domain was 1000

m × 500 m × 500 m ($10.4D \times 5.2D \times 5.2D$, where $D = 96$ m is the turbine rotor diameter), and the top, bottom, and sides of the domain had symmetry boundary conditions imposed. No ground surface was modelled in order to maintain uniform inflow. The resolution farthest from the rotor was 10 m, and the mesh was refined progressively to 0.625 m directly around the rotor, producing a grid with a total of 5.6 million nodes (figure 6.1). This resolution is typical of or finer than similar large-scale simulations in the literature [149, 155, 156].

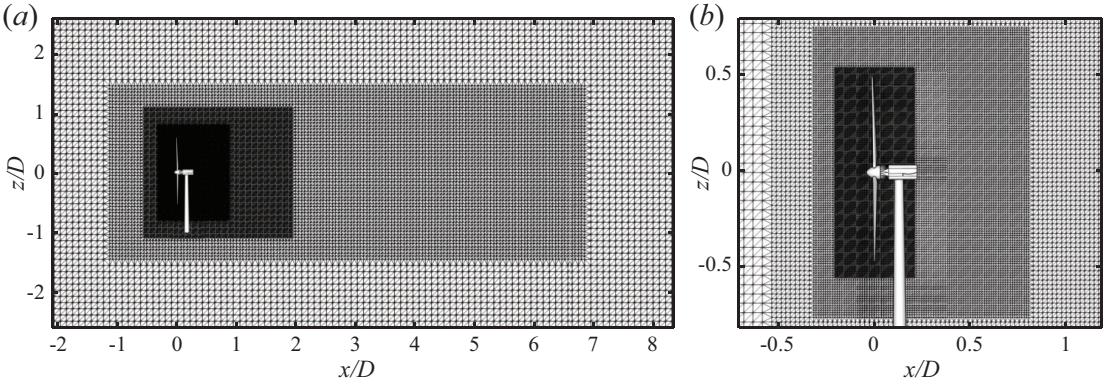

Figure 6.1: (a) The entire simulation domain, showing the grid refinement and the position of the turbine. (b) A smaller portion of the simulation domain highlighting the refined region around the rotor. Note that the simulated turbine is represented using actuator lines. The model included here is shown for visualization purposes. In the current study, wake behaviors are analyzed at $x/D = 0.18$ and $x/D = 5$.

6.2.2 Wind turbine model

The simulated wind turbine was modelled after the University of Minnesota Eolos wind turbine, described in previous studies [17, 43, 5, 49, 3]. It is a 2.5 MW Clipper Liberty C96 three-bladed, horizontal-axis, pitch-regulated, variable speed machine with a 96 m rotor diameter (D) and 80 m hub height (H_{hub}). The turbine model was implemented in OpenFAST [14], and the controller was tuned to match the real power curve as closely as possible. The model was then incorporated into the LES using an actuator line model, where the blades were represented by a force distribution along a line extending from the hub to each blade tip. The actuator line for each blade was discretized into 100 points, and the forces from the blades were then projected onto the flow using a Gaussian

function [157, 158]. The blade forces were calculated using lift and drag coefficient look-up tables determined by the specifications of the Eolos turbine used for the field studies. The nacelle and tower were included in the model as additional body forces, as these structural components have been shown to significantly impact the near wake [49]. The tower was modeled as a drag force discretized into 50 points to allow for variation in cross-sectional diameter along the height. As with the blades, the forces were projected onto the flow using a Gaussian function. The nacelle was modeled as a Gaussian drag body force with a frontal area of $A_n = 20$ m^2 and a drag coefficient of $C_{D,n} = 0.5$. The width of the Gaussian kernel was determined as a function of A_n and $C_{D,n}$ to ensure the appropriate momentum thickness of the generated wake [159]: $\epsilon_D = \sqrt{2C_{D,n}A_n/\pi}$. Previous studies have shown that the actuator line model can successfully reproduce the flow features that dictate the large-scale near-wake behaviours investigated in the current study, i.e., near-wake flow fields and coherent structures [160, 161, 25, 158, 13]. Tip loss corrections have not been included in the current study. Sarlak et al. [77] showed that the wake of a turbine modeled using actuator lines is not significantly modified by the use of tip loss corrections for low to intermediate tip speed ratios, such as those used in the current study.

6.2.3 Wake detection and fitting

The current study focuses on the near wake ($0.18D$ downstream, selected to enable comparison with field-scale experimental results from Abraham and Hong [3]) where the turbine-induced flow modulation originates. To quantify the centerline and width of the wake, the velocity at the cross-section is fit with a two-dimensional Gaussian function,

$$u(y,z) = A * \exp\left(-\frac{(y-y_c)^2 + (z-z_c)^2}{2\sigma^2}\right) + U_\infty, \tag{6.1}$$

where (y_c, z_c) is the center of the Gaussian, σ^2 is the variance, and A is a fitting coefficient [129, 162]. The Gaussian wake model is used because it minimizes the number of fitting coefficients, whereas other wake models, particularly those designed for the near wake, require many additional fitting parameters (e.g., [163, 164, 165]). The center of the wake cross-section is taken to be the center of the Gaussian fit, which is used to determine the wake deflection angle, ξ (figure 6.2a). Often the far wake width is defined

as the 95% confidence interval of the Gaussian velocity deficit profile [105, 166]. However, the near wake velocity deficit has steeper edges than in the far wake, so the 95% confidence interval would severely overestimate the near wake width. By comparing the fitted Gaussian to the near-wake velocity deficit obtained from the LES, we found that the 91% confidence interval provides a more accurate definition of the near wake width. The justification of this selection is described in more detail in Appendix A.4. The wake width is then converted to the wake expansion angle, shown in figure 6.2(b), using the following relation:

$$\varphi = \arctan\left(\frac{1.7\sigma - \frac{D}{2}}{0.18D}\right), \tag{6.2}$$

where the factor of 1.7 corresponds to the 91% confidence interval and $0.18D$ is the downstream distance of the measurement plane.

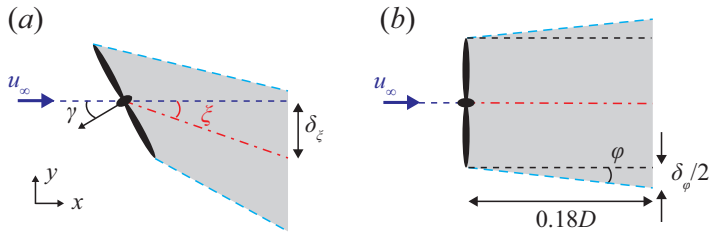

Figure 6.2: (a) Schematic of the turbine wake showing the definition of the yaw misalignment angle, γ, the wake deflection angle, ξ, and the wake deflection magnitude, δ_ξ, from the top (positive-z) view. Coordinate axes are also shown. (b) Schematic of the turbine wake showing the definition of the wake expansion angle, φ, and the wake expansion magnitude, δ_φ. The incoming wind is indicated by u_∞ and the measurement plane is located $0.18D$ downstream of the rotor.

6.3 Results

We now present results for the turbine wake response to three types of operational changes: 1) variations in expansion caused by blade pitch, 2) redirection from wind direction changes, and 3) wake deflection due to rotor yaw. Sample images of the wake velocity during each of these scenarios are shown in figure 6.3.

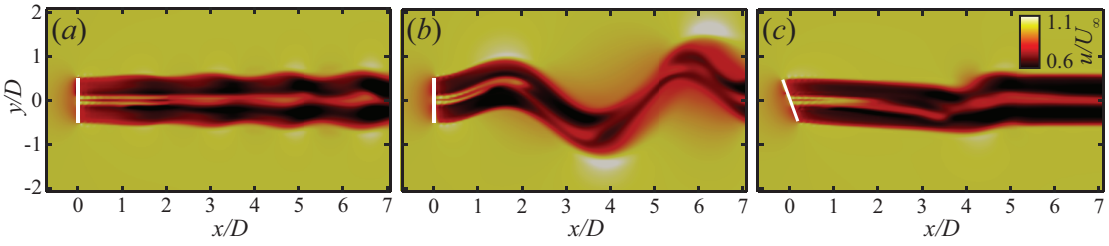

Figure 6.3: Sample timesteps of the wake streamwise velocity at hub height from the top (positive-z) view during the simulations modeling changes in (a) blade pitch, (b) wind direction, and (c) rotor yaw. White lines indicate the position and orientation of the rotor.

6.3.1 Blade pitch

First the effect of changes in blade pitch (β) on the near wake is investigated. Most utility-scale wind turbine controllers increase the pitch of the blades when the incoming wind is above the rated wind speed to reduce the angle of attack of the airfoils and decrease the thrust force of the rotor as a way to regulate the structural loading. To examine the effect of this process on the wake, a time series of pitch changes at different rates, similar to those observed for a utility-scale turbine, is implemented in the OpenFAST turbine controller. The pitch first increases at each rate for 10 s, then decreases at the same rate for 10 s, as shown in figure 6.4(a) along with the resulting changes in wake expansion angle. The wake expansion varies inversely with changes in blade pitch due to the aforementioned reduction in thrust caused by lowering the angle of attack. The same relationship is observed in the field experiment from Abraham and Hong [3]. Interestingly, the correlation is not linear, rather some hysteresis occurs in the wake response. This hysteresis can also be observed in the field data, as evidenced by the fact that there are multiple different values of wake expansion for a given blade pitch angle during a sample sequence of 800 s (figure 6.4b). The same characteristic looping behavior is observed in the relationship between blade pitch and wake expansion from the field data as that observed in the simulation results, though the loops are not as regular as those from the simulations due to the many different factors influencing wake behaviour in the field. Because individual variables are difficult to isolate in the field, the cause of this observation could not be confirmed with certainty. In the simulation, the cause of such hysteretic response becomes clear when comparing the wake expansion

with the tip speed ratio, $\lambda = \frac{\omega D}{2u_\infty}$ where ω is the angular velocity of the rotor, which changes in response to changes in blade pitch. Figure 6.4(c) shows the strong correlation between λ and φ, which suggests that the wake is actually responding to the change in rotor speed rather than the change in blade pitch itself. A similar trend is observed in the experimental data, conditionally sampled for periods where the wind is above the rated speed and the blade pitch is changing, though with a wider range of λ due to larger changes in u_∞ and much more variability due to the dynamic atmospheric wind speed and direction (figure 6.4d). Note that the results of the simulation are repeatable because of the use of uniform inflow, while the experimental data is not deterministic due to the multitude of uncontrolled stochastic variables in the field. Still, the trends observed in the experimental data are robust, as described in more detail in Abraham and Hong [3]. The relationship between λ and φ is stronger than that between β and φ because the reduction in lift force on the blades due to the increase in pitch causes the rotor to slow down, which causes the wake expansion to decrease. This reduction in rotor speed lags slightly behind the increase in blade pitch due to the inertia of the flow. Schepers [138] described the effect of flow inertia to explain the observed lag in turbine response to a step increase in blade pitch. He attributed the lag to the time it takes to accelerate the flow after a decrease in axial induction. Ebrahimi and Sekandari [140] observed a similar delay in thrust change after a step change in wind speed. A linear regression fit is applied to the relationship between λ and φ from the experiment, revealing a shallower slope than that of the simulation data (figure 6.4d). This difference in slope is attributed to the smoothing applied to the experimental wake boundary data to account for turbulent fluctuations, which tends to obscure more extreme values. The experimental data also includes many additional sources of uncertainty, including concurrent changes in multiple parameters that may interact, and the measurement of incoming velocity at the turbine nacelle, which is within the induction zone of the turbine [45]. However, it is remarkable that the overall trends from the experiment and simulations still match well in spite of these discrepancies, indicating that the large-scale wake behaviours dominate over the effects of smaller-scale turbulence.

To quantify the timescale of the wake expansion response, changes in blade pitch angle at different rates (β') are simulated. Blade pitch is varied from 1° (the default pitch angle of the Eolos turbine when operating below the rated wind speed) to 7° at

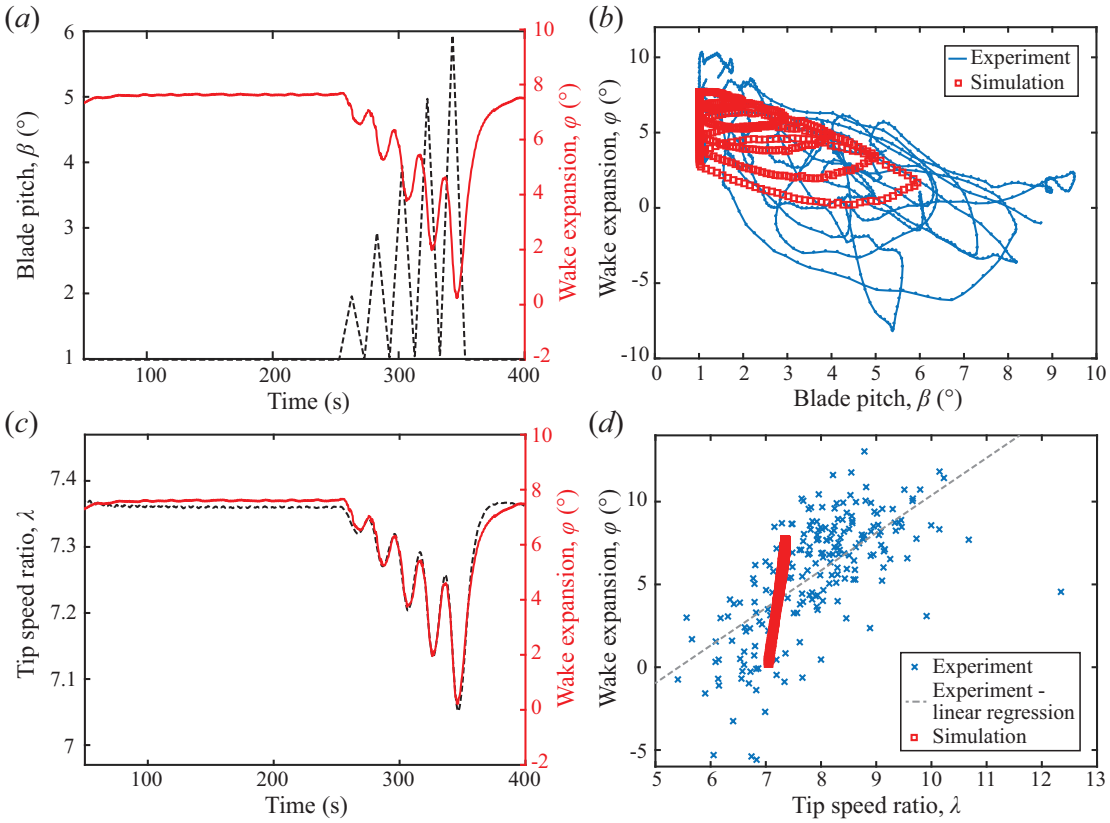

Figure 6.4: (*a*) Prescribed changes in blade pitch (dashed black line) and the resulting changes in wake expansion (solid red line). (*b*) Instantaneous wake expansion angle versus blade pitch from the simulation (red squares) and a sample sequence of 800 s from the experiment from Abraham and Hong [3] (blue line). (*c*) Time series of tip speed ratio changes (dashed black line) caused by changes in blade pitch and resulting wake expansion (solid red line). (*d*) Instantaneous wake expansion angle versus tip speed ratio from the simulation (red squares) and from periods of the experimental dataset from Abraham and Hong [3] where the wind is above the rated speed and the blade pitch is changing (blue crosses). A linear regression fit to the experimental data is included to facilitate comparison with the simulation data.

several different rates between 0.1 °/s and 4 °/s, and from 7° to 1° at rates between -0.1 °/s and -4 °/s. Such step changes are used to replicate the blade pitching behavior of an operational turbine, which cannot change the blade pitch instantaneously. Figure 6.5(a) shows a sample time sequence of the change in wake expansion in response to an increase of blade pitch at a constant rate. The wake begins expanding when the pitch begins changing, then asymptotically approaches its maximum change in expansion, $\varphi_{\max}$. To facilitate physical interpretation of the results, values are normalized using the timescale $\tau_0 = D/U_\infty$ and angles are converted from degrees to radians. Figure 6.5(b) shows that $\varphi_{\max}$ is independent of pitch rate, and that with a 6° (0.10 radian) change in blade pitch, the wake expansion always changes by $\sim 16°$ (0.28 radians). On the other hand, the duration of the wake expansion change is strongly dependent on pitch rate. To quantify this effect, a wake expansion timescale (τ_φ) is defined as in exponential decay, i.e., as the time for the change in wake expansion to reach $\varphi_\tau = (1 - 1/e)\varphi_{\max}$. Berger and Kühn [139] similarly observed exponential decay of wake velocity in response to a step change in rotor thrust. Figure 6.5(c) shows that τ_φ is significantly higher at slow pitch rates ($\tau_\varphi/\tau_0 \sim 5$) compared to fast pitch rates ($\tau_\varphi/\tau_0 \sim 1$). Figure 6.5($d$) further elucidates this trend by scaling the wake expansion timescale by the pitch maneuver duration ($t_{\text{end}} - t_{\text{start}}$). This scaling reveals that $\tau_\varphi/(t_{\text{end}} - t_{\text{start}})$ is linearly dependent on $\beta'\tau_0$, highlighting that as the pitch rate increases, the lag in wake response increases, indicating an increased deviation from quasi-steady behavior. Some asymmetry is observed between increasing and decreasing blade pitch, where the timescales tend to be larger for increasing pitch. This trend is consistent with the explanation provided by Schepers [138] for the difference between an upward and downward pitching step: For an increase in blade pitch, the axial induction is initially large, leading to lower wake velocity and advection time than for a decrease in blade pitch, where the wake velocity is initially higher. To provide a sense of the typical blade pitch rate of a utility-scale wind turbine operating in the field, the mean pitch rate implemented by the Eolos turbine during the experiment described in Abraham and Hong [3] was 0.4 °/s ($\beta'\tau_0 = 0.04$), with a maximum and minimum rate of 2.4 °/s ($\beta'\tau_0 = 0.26$) and 0.2 °/s ($\beta'\tau_0 = 0.02$), respectively. These findings have important implications for the design of advanced wind farm control algorithms that use blade pitch to regulate turbine axial induction (e.g., [113]), which cannot expect the wake to

react immediately to changes in blade pitch.

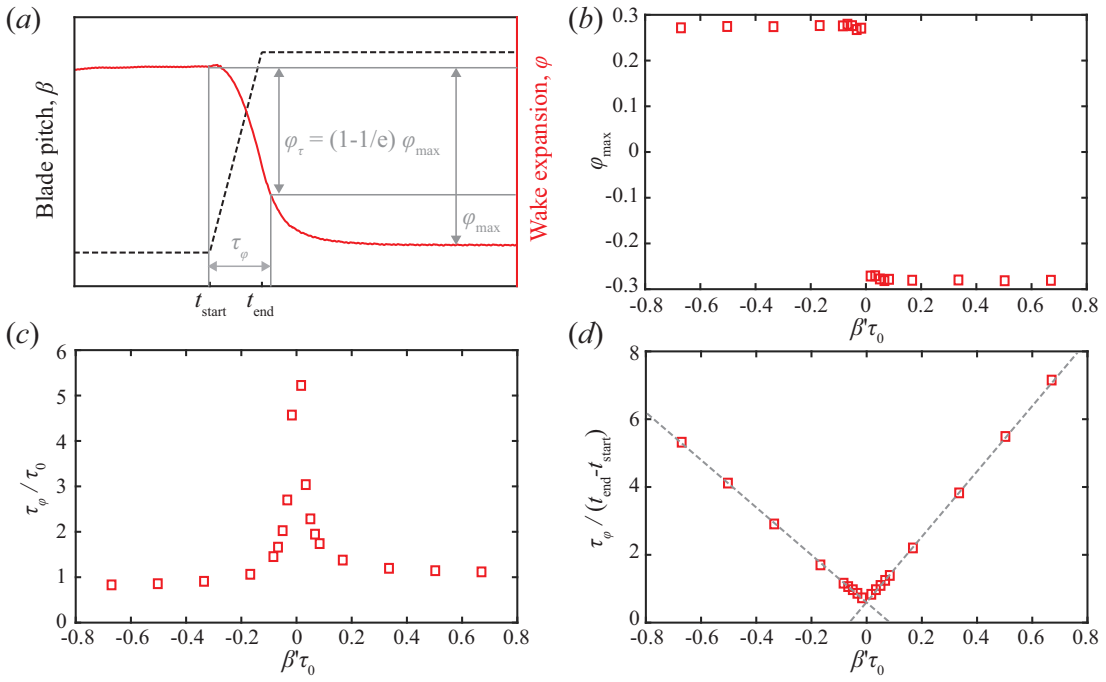

Figure 6.5: (*a*) Sample change in blade pitch angle at a constant rate (dashed black line) and the resulting wake expansion response (solid red line). The wake expansion timescale, τ_φ, and maximum change in wake expansion, $\varphi_{\max}$, are defined in grey. (*b*) Relationship between normalized blade pitch rate and maximum wake expansion change. (*c*) Relationship between normalized pitch rate and normalized wake expansion timescale. (*d*) Relationship between normalized pitch rate and wake expansion timescale normalized by the duration of the blade pitch maneuver. The grey dashed lines show linear regression fits to the data for $\beta'\tau_0 < 0$ and $\beta'\tau_0 > 0$.

6.3.2 Wind direction

In Abraham and Hong [3], a clear correlation was observed between instantaneous incoming wind direction and spanwise wake deflection, though it was in the opposite direction of that described in several previous studies conducted under steady conditions (e.g., [1, 167, 168]). Here the mechanism behind such conflicting results is investigated in more detail. First, the spanwise component of the wind is varied sinusoidally with a 20 s period while the rotor direction is held constant, providing the turbine with

dynamic yaw misalignment (γ) similar to the conditions experienced in the field due to the stochasticity of the atmospheric flow (figure 6.6*a* and supplementary movie 1). The resulting instantaneous wake deflection is shown to follow the trend observed in the field (figure 6.6*b*). Note that, as in the wake expansion case, the slope of the wake deflection response to yaw misalignment angle is shallower for the experimental data than the simulation data. Once again this discrepancy is attributed to the turbulence and uncertainties of the experimental data. Additionally, as will be described in more detail in the following sentences, the wake deflection response is dependent on the timescale of wind direction changes. Atmospheric wind experienced by turbines in the field fluctuates across a range of timescales, whereas the simulated wind direction changes with a constant period.

The period of wind direction changes is increased to 50 s, and a different trend is observed compared with the 20 s period (figure 6.6*c* and supplementary movie 2). With these slower wind direction changes, the wake deflection more closely follows the analytical relationship defined in Jiménez et al. [1] for steady yaw error, though with some hysteresis (figure 6.6*d*). This hysteresis is caused by a lag in the wake response to changes in yaw error. These results suggest the existence of a characteristic wake response timescale during which the wake deflection transitions from the transient opposite deflection response to the steady analytical response. The dependencies of this timescale will be explored in the following section using step changes in γ at different rates. Note that the wake deflection response is asymmetrical, with a larger deflection on the positive side than the negative side, likely caused by wake rotation [167]. The turbine modelled in the current study rotates in the counterclockwise direction. For a clockwise rotating turbine, the negative deflection may be larger than the positive deflection.

6.3.3 Rotor yaw

Using changing wind direction to investigate yaw error includes the coupling of two effects: yaw misalignment induced wake deflection and changes in the direction of wake advection by the surrounding flow. Though this coupling is representative of the wake response in the field under stochastic atmospheric flow, these effects must be separated to gain further insight into the flow modulation caused by the turbine. Therefore,

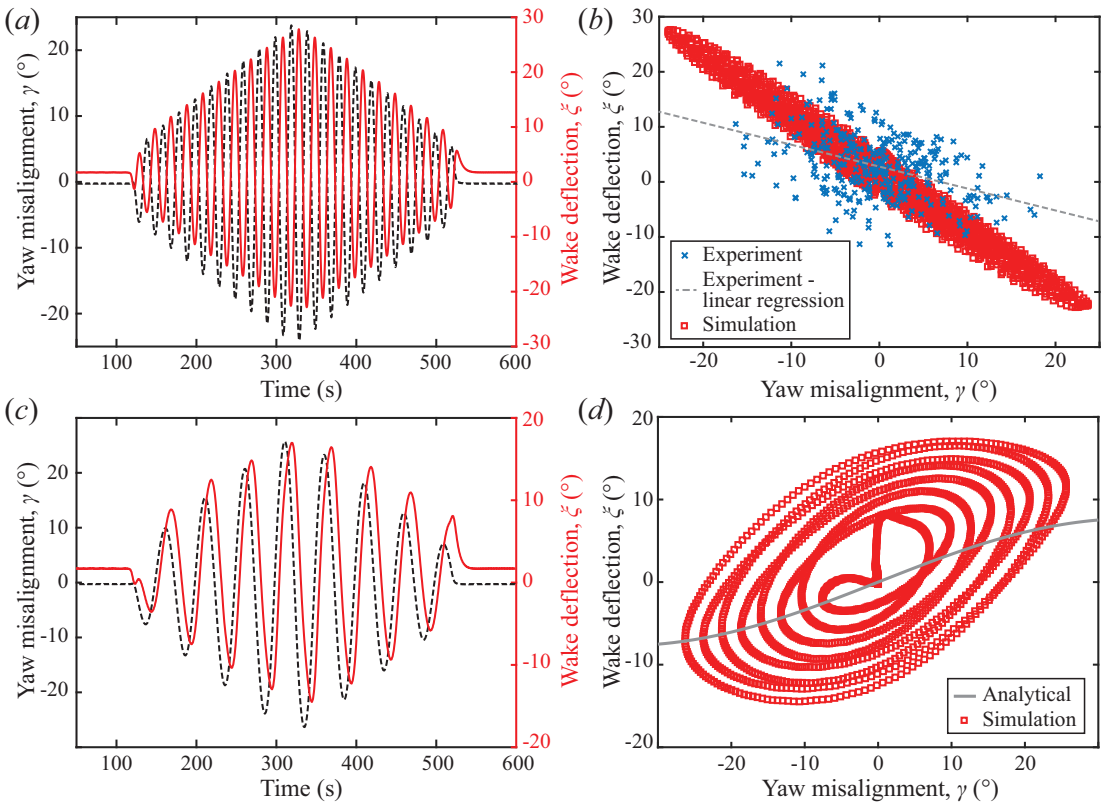

Figure 6.6: (*a*) Prescribed changes in wind direction with a 20 s period (dashed black line) and the resulting changes in spanwise wake deflection (solid red line). (*b*) Instantaneous wake deflection angle versus wind direction for the experiment from Abraham and Hong [3] (blue crosses) and the simulation (red squares). A linear regression fit to the experimental data is included to facilitate comparison with the simulation data. (*c*) Prescribed changes in wind direction with a 50 s period (dashed black line) and the resulting changes in spanwise wake deflection (solid red line). (*d*) Analytical solution for the steady wake deflection angle from Jiménez et al. [1] (grey line) compared to the instantaneous wake deflection versus wind direction from the simulation (red squares).

the same yaw misalignment sequence as that shown in figure 6.6(c) is implemented by changing the rotor yaw angle while keeping the wind direction constant (figure 6.7a). In this scenario, the lag in wake response is longer than previously observed for the changing wind direction scenario with the same period (50 s). This discrepancy is attributed to the fact that, when the wind direction changes, the surrounding flow advects the wake in the spanwise direction, pushing it towards the steady yaw response. Additionally, the streamwise velocity must be kept constant to ensure constant mass flow through the simulation domain, so spanwise velocity is varied in the wind direction simulation. This increase in spanwise velocity causes the wind velocity magnitude to increase. Jiménez et al. [1] showed that the spanwise force exerted by the turbine on the wake is dependent on the square of the inflow velocity magnitude under steady conditions. Because the velocity magnitude is larger in the wind direction simulation during periods of yaw misalignment than in the rotor yaw simulation, the force pushing the wake towards steady-state deflection is stronger in the wind direction simulation. Therefore, the dynamic wake deflection approaches steady-state behavior more quickly than in the rotor yaw simulation. Though the timescales of the wake response in the two cases are different, the general trends observed are consistent, including the magnitude of the inverse wake deflection. To isolate the effect of dynamic wake modulation from that of wake advection by ambient wind, and to facilitate the extension of these findings to wake control applications, the following analysis uses rotor yaw angle changes to investigate dynamic spanwise wake deflection in more detail.

To quantify the inverse wake deflection magnitude and timescale more precisely, changes in rotor direction with constant yaw rates are investigated. The yaw angle is varied from 0° to 20° at several different rates (γ') between 0.1 °/s and 4 °/s, and from 20° to 0° at rates between -0.1 °/s and -4 °/s. As with blade pitch, step changes are used to replicate the yawing behavior of an operational turbine, which cannot change the rotor angle instantaneously. Figure 6.8(a) shows a sample time sequence of wake deflection with a constant yaw rate. Under this condition, the wake first deflects in the direction opposite of the yaw change, then deflects in the same direction as the yaw change for the remaining duration of the rotor motion, consistent with the results of previous studies [121, 144, 145]. Results are once again normalized by τ_0 and angles are converted to radians. Figure 6.8(b) quantifies the magnitude of the maximum inverse

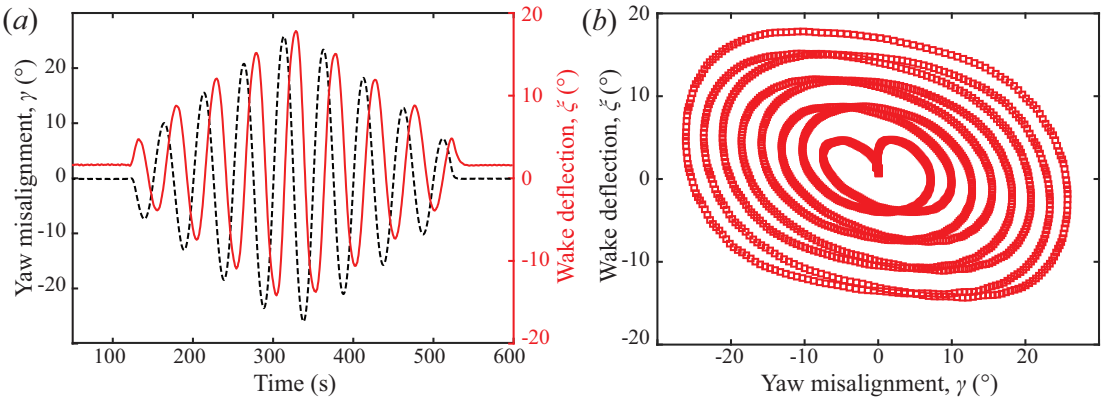

Figure 6.7: (a) Prescribed sinusoidal changes in rotor yaw angle with a period of 50 s, matching the changes in wind direction shown in figure 6.6(c), (dashed black line) and the resulting changes in spanwise wake deflection (solid red line). (b) Instantaneous wake deflection angle versus yaw misalignment angle.

wake deflection, $\xi_{\max}$, showing a clear dependence on yaw rate. This deflection is not insignificant; at the largest yaw rates, it reaches 75% of the rotor misalignment angle. However, the duration of this deflection decreases with increasing yaw rate magnitude. The inverse wake deflection timescale (τ_ξ) is defined in the same way as the wake expansion timescale, i.e., as the time for the wake deflection to reach $\xi_\tau = (1 - 1/e)\xi_{\max}$. The value of τ_ξ/τ_0 generally increases with decreasing yaw rate magnitude, though the peak occurs at a normalized yaw rate $\gamma'\tau_0 > 0$. This asymmetry is also likely caused by wake rotation, and may be reversed in the case of a clockwise rotating turbine. Note that τ_ξ ranges from $0.23\tau_0$ to $0.54\tau_0$ for the yaw rates investigated here, and a yaw rate of 0.5 °/s ($\gamma'\tau_0 = 0.08$, typical of e.g., the Eolos turbine) results in $\tau_\xi = 0.53\tau_0$ when the yaw is increasing and $\tau_\xi = 0.35\tau_0$ when it is decreasing. These values show that the wake takes a significant amount of time to stabilize in response to changes in yaw angle, which has important implications for the design of yaw-based wind farm optimization algorithms. This crucial point will be discussed further in Section 6.4. When an inverse wake deflection rate is defined as $\xi_{\max}\tau_0/\tau_\xi$, another interesting trend is revealed. This quantity is linearly dependent on $\gamma'\tau_0$, with a nearly one-to-one relationship (the linear regression slope is -1.2 and intersects the ordinate axis at $\xi_{\max}\tau_0/\tau_\xi = 0.01$). This relationship clearly demonstrates the tradeoff between inverse wake deflection magnitude and duration under different yaw rates. The physical explanation for this relationship

will be further elucidated in Section 6.3.4. Note that these yaw changes are implemented under turbine operational conditions that are otherwise optimized by the turbine controller (i.e., blade pitch is set to the value determined to maximize power based on the wind speed, as it would be for an operational utility-scale turbine). The effect of yaw changes under sub-optimal operating conditions has not been investigated. However, we expect a reduction in thrust coefficient to increase the inverse wake deflection timescale, as Jiménez et al. [1] showed that the steady wake deflection response weakens with reduced thrust coefficient.

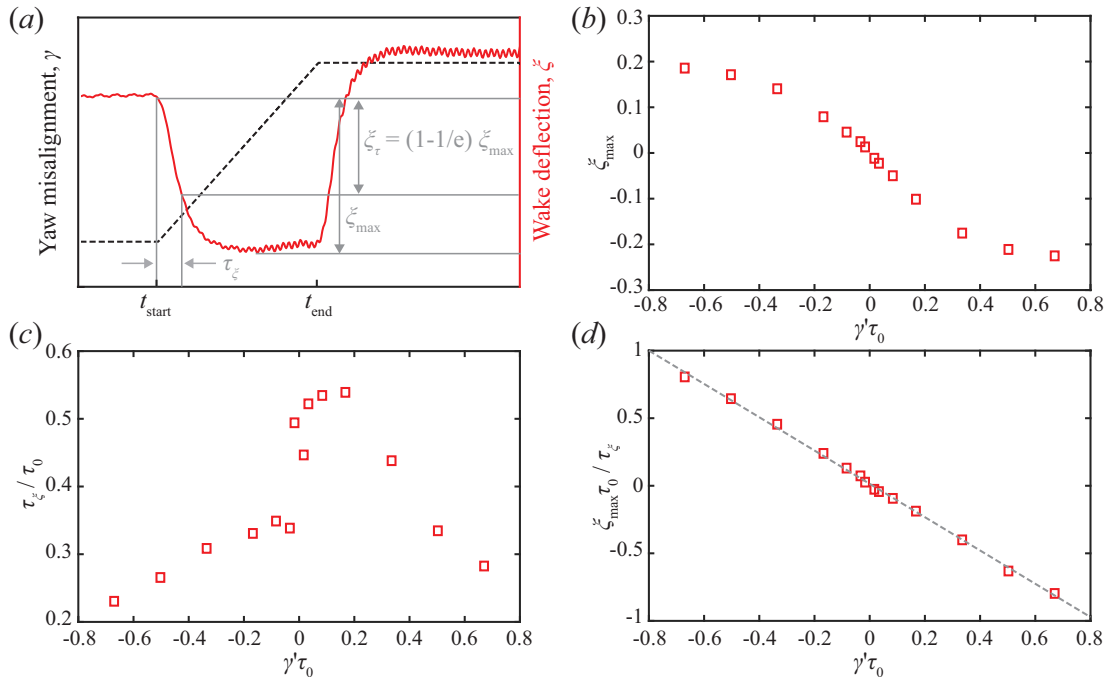

Figure 6.8: (*a*) Sample change in yaw angle at a constant rate (dashed black line) and the resulting wake deflection response (solid red line). The wake deflection timescale, τ_ξ, and maximum inverse wake deflection, $\xi_{\max}$, are defined in grey. (*b*) Relationship between normalized yaw rate and maximum inverse wake deflection. (*c*) Relationship between normalized yaw rate and normalized inverse wake deflection timescale. (*d*) Relationship between yaw rate and $\xi_{\max}\tau_0/\tau_\xi$. The dashed grey line shows the linear regression fit to the data.

6.3.4 Vorticity analysis during dynamic yaw misalignment

Further insight into the mechanism behind these wake behaviors can be gained by looking at the vorticity in the wake. Previous studies have shown that streamwise vorticity plays an important role in the behavior of the yawed wake, leading to wake deflection and the curled wake shape that develops downstream [152, 167, 168, 169, 170]. When streamwise vortices with opposing signs form on the top and bottom halves of the wake, they induce a spanwise velocity. Based on these studies, the following analysis focuses on the streamwise component of the vorticity vector. In the current study, after the turbine yaws, negative streamwise vorticity (ω_x) is observed in the top half of the wake and positive streamwise vorticity is observed in the bottom half (see supplementary movie 3), consistent with the steady yawed wake behavior described in Zong and Porté-Agel [170]. More interestingly, during the positive yaw maneuver, a short period of increased vorticity is observed in the top-left quadrant (I) of the wake and a period of decreased vorticity is observed in the bottom-right quadrant (IV) of the wake (figure 6.9a and supplementary movie 3). The maximum streamwise vorticity in sections of each of the four quadrants of the wake located at $z = \pm 0.3D$, $0.2D < y < 0.5D$ or $-0.5D < y < -0.2D$, and $0.5D < x < 0.6D$ compared to the theoretical vorticity trend excluding the transient effect is plotted over time in figure 6.9(b), demonstrating the observed vorticity changes. Without the transient effect, the streamwise vorticity would be expected to transition smoothly from its initial value to the reduced value in the top half of the wake (quadrants I and II) and the increased value in the bottom half (quadrants III and IV). However, the transient effect shifts the vorticity in the opposite directions in quadrants I and IV. This transient vorticity shift can be explained by the angle of the vortices shed from the turbine blade tips during the yaw maneuver, where one side of the rotor is moving upstream and the other is moving downstream. As explained in Zong and Porté-Agel [170], the angle of the blade tip vortex trajectory determines the streamwise component of the vorticity, which dictates the deflection direction of the wake. When the rotor is turning, the side moving upstream (the left side in figure 6.9) is experiencing a larger streamwise velocity relative to the flow, increasing the streamwise component of the vorticity on that side (supplementary movie 3). On the side moving downstream, the relative velocity is reduced, along with the streamwise vorticity component. As the yaw angle increases, the steady yaw angle effect described

in Zong and Porté-Agel [170] dominates over the transient effect, leading to the expected steady-state vorticity distribution. In quadrants I and IV the transient effect is in the opposite direction of the steady effect, while the two effects are in the same direction in quadrants II and III. Therefore quadrants I and IV contribute to the opposite wake deflection while II and III do not. When the yawing maneuver ends and the two sides of the rotor experience the same relative streamwise velocity, the transient effect disappears altogether.

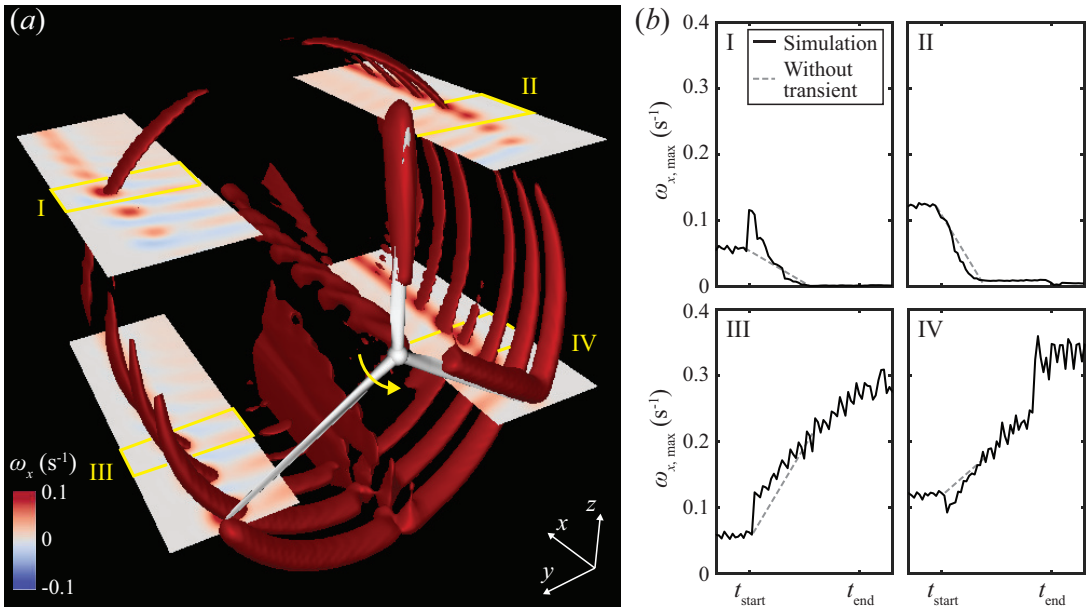

Figure 6.9: (a) Isocontour of streamwise vorticity with cut planes in each quadrant. The isocontour value is $\omega_x = 0.1$ s^{-1}. Note that the turbine tower and nacelle are included in the simulated turbine model, though only the rotor is shown here for clarity. The yellow arrow near the hub indicates the direction of the yaw. The yellow boxes labeled with roman numerals indicate the regions plotted in (b), which shows the maximum streamwise vorticity component within each region over time compared to the theoretical vorticity trend excluding the transient effect. The plotted regions are located at $z = \pm 0.3D$, $0.2D < y < 0.5D$ or $-0.5D < y < -0.2D$, and $0.5D < x < 0.6D$.

Though the value of the streamwise vorticity remains positive in all four quadrants during the transient wake response, the difference in vorticity between the top and bottom of the wake is enough to induce a positive spanwise velocity and corresponding inverse wake deflection. Both the spatially averaged spanwise velocity (v_{avg}, figure

6.10a) and the maximum spanwise velocity ($v_{\max}$, figure 6.10b) within the rotor area at a y-z plane located $0.5D$ downstream show a peak just after the yawing maneuver begins, indicating a transient inverse wake deflection response. Subsequently, the spanwise velocity decreases due to the steady yaw response. As the streamwise vorticity is responsible for the negative spanwise velocity and wake deflection during the steady yaw response [170], so our results indicate the opposite streamwise vorticity shift shown in figure 6.9 causes the positive spanwise velocity and wake deflection that are characteristic of the transient inverse wake deflection response. Note that the magnitude of the transient spanwise velocity peak increases with downstream distance, as does the inverse vorticity shift. The values at $x = 0.5D$ are presented to highlight the velocity and vorticity trends that develop directly after the flow passes through the rotor.

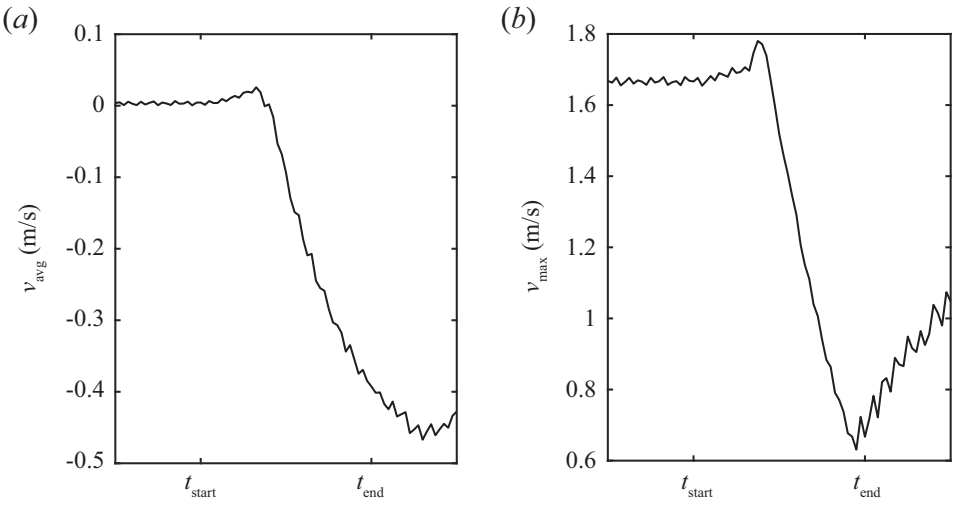

Figure 6.10: (a) Spatially averaged and (b), maximum spanwise velocity (v) over the rotor area in the y-z plane $0.5D$ downstream of the turbine during a yawing maneuver.

The magnitude of the transient vorticity shift is directly dependent on yaw rate, as shown in figure 6.11. This linear relationship sheds light on the clear dependence of the inverse wake deflection rate, $\xi_{\max}\tau_0/\tau_\xi$, on yaw rate shown in figure 6.8. The inverse wake deflection timescale τ_ξ depends on yaw rate because higher yaw rates execute a yawing maneuver of the same magnitude more quickly, but the magnitude of the inverse wake deflection $\xi_{\max}$ is also affected by yaw rate because the strength of the vorticity generated at the rotor is determined by yaw rate. This trend is in contrast

to that observed for blade pitch in figure 6.5, because the magnitude of the maximum wake expansion change $\varphi_{\max}$ is unaffected by pitch rate. The transient wake expansion response to dynamic blade pitch changes is simply a slow approach to steady-state behavior, whereas the wake deflection response to yaw changes occurs in the opposite direction of the steady-state behavior.

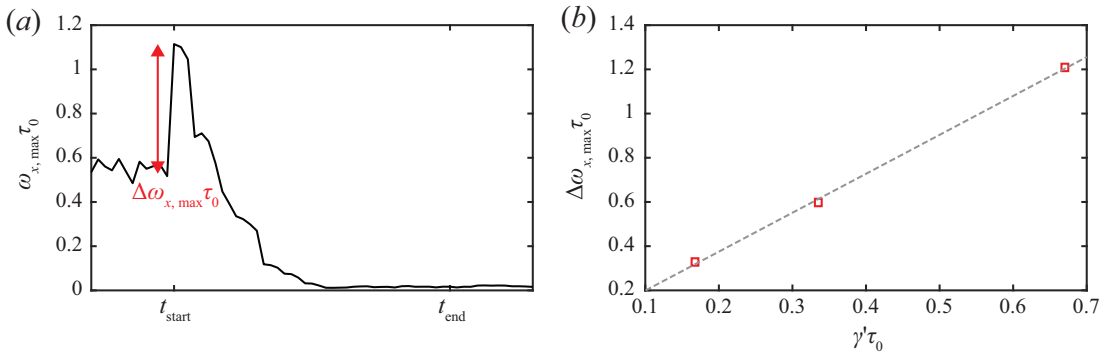

Figure 6.11: Transient vorticity shift dependence on yaw rate, inluding (a) the definition of the vorticity shift magnitude, $\Delta\omega_{x,\max}\tau_0$, and (b) a plot of $\Delta\omega_{x,\max}\tau_0$ versus normalized yaw rate, $\gamma'\tau_0$. The dashed gray trendline shows the linear regression of the data in (b).

The vertical component of vorticity also changes when the rotor is yawing, with the left side producing stronger vorticity than the right side, as with the streamwise component. This imbalance in vertical vorticity may also induce a positive spanwise velocity, contributing to the observed spanwise wake deflection, though it would likely be much smaller than that generated by the streamwise component of vorticity [171]. Previous field-scale flow visualization studies show strong, clear tip vortices within the near-wake of utility-scale wind turbines [17, 18, 5, 49, 3], so turbulence and shear are not expected to significantly inhibit the aforementioned mechanism in the field. Indeed, the same inverse wake deflection described above was observed in the field data from Abraham and Hong [3]. That being said, figure 6.6 shows that the magnitude of the resulting wake deflection is damped by the increased mixing caused by these atmospheric effects.

Based on the analysis of the spanwise wake deflection, one might expect a similar trend in the vertical direction due to the differences in streamwise vorticity between the

left and right sides of the wake. However, no significant transient vertical wake shift is observed during the yawing maneuver. This lack of vertical deflection is attributed to the large number of competing effects acting on the wake in the vertical direction. First, the interaction between wake rotation and the ground has been shown to substantially influence the vertical displacement of the wake center during yaw [167]. Furthermore, Kleusberg et al. [172] showed that the angle of attack of the blades varies between the top and bottom of the rotor when the turbine is yawed, introducing an additional source of vertical asymmetry. Finally, differences in spanwise vorticity between the top and bottom of the rotor may contribute to changes in the vertical velocity field of the wake. The combination of these effects, along with the spanwise asymmetry in streamwise vorticity observed in figure 6.9, balance such that no significant transient vertical wake deflection is observed.

6.3.5 Downstream propagation

In order to apply the findings of the current study to the development of control strategies, the extension of these near-wake timescales to the far wake must be investigated. Qualitatively, it is clear that these dynamic wake modulation behaviours persist downstream. In the wake expansion case, an interesting phenomenon is observed as the wake advects downstream after a change in blade pitch. When the blade pitch increases, the velocity deficit decreases due to a reduction in lift on the blades, so the upstream part of the wake moves faster than the downstream part, leading to a bulge at the point of blade pitch change (figure 6.12*a*). When the blade pitch decreases, the opposite occurs and the wake pinches off (figure 6.12*b*). These same wake width changes have been exploited to enhance wake mixing in previous studies investigating dynamic induction control of wind farms [119, 112, 113, 173]. When the rotor yaw changes, the disturbance due to inverse wake deflection is also observed to persist and strengthen as it moves into the far wake (figure 6.12*c* and *d*).

Quantitative investigation of dynamic wake modulation propagation downstream is also provided, though we note the limitations of this analysis. In the far wake, coherent structures have broken down and atmospheric turbulence is much more dominant than in the near wake [174]. Turbulence is not included in the current study to facilitate the observation of deterministic near wake modulation, as described in Section 6.2.1. The

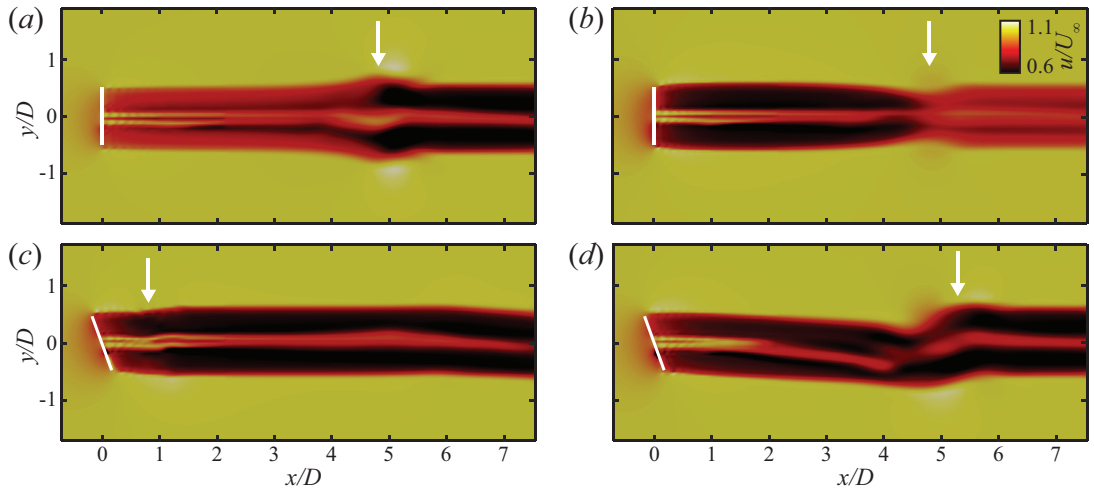

Figure 6.12: Sample timesteps of the wake streamwise velocity at hub height from the top (positive-z) view 50 s after (a) an increase and (b) a decrease in blade pitch. The resulting changes in wake expansion have advected several times the rotor diameter downstream, indicated by the white arrows. Sample timesteps of the same quantity (c) 10 s and (d) 60 s after a change in rotor yaw. The position and orientation of the turbine rotor is marked by white lines and the location of the resulting inverse wake deflection at each timestep is indicated by white arrows.

downside of this simplification is that it limits the ability to draw realistic conclusions about far-wake propagation. Therefore, the following analysis adds primarily theoretical value for idealized conditions. First, the wake expansion response to changes in blade pitch is calculated at $5D$ downstream of the rotor and compared to that observed at $0.18D$. The $5D$ distance is chosen because it is well within the far wake (typically considered to begin at $2-4D$ downstream [23]), but still within the higher-resolution portion of the simulation mesh (figure 6.1a). Furthermore, Santhanagopalan et al. [133] found $5D$ to be the optimal spacing between the first and second row of turbines under most conditions. To facilitate this far wake comparison, $\delta_{\varphi,\max}/D$, where δ_φ is the deviation of the wake diameter from D, is used to represent the amount of wake expansion rather than $\varphi_{\max}$. This metric is selected because its calculation does not depend on the downstream distance, unlike φ (see figure 6.2), and therefore demonstrates how the magnitude of a perturbation changes as it propagates downstream. As shown in figure 6.13(a), the maximum wake expansion does not change significantly between

$0.18D$ and $5D$. The maximum inverse wake deflection, on the other hand, decreases in magnitude as the perturbation is advected downstream (figure 6.13b). The wake deflection metric used, $\delta_{\xi,\max}/D$, is defined using the spanwise deviation of the wake center (figure 6.2), with the wake center location determined by a Gaussian fit to the streamwise wake velocity profile as described in section 6.2.3. Though figure 6.13(b) shows a significant reduction in inverse wake deflection at $5D$, figure 6.12(d) clearly shows qualitatively that it does, in fact, persist into the far wake. This discrepancy between the qualitative and quantitative observations is attributed to the significant distortion of the wake cross-section in the far wake during periods of yaw misalignment [152, 167, 168, 169, 170].

Wake expansion and deflection timescales are also calculated at $5D$ downstream and compared to those at $0.18D$, after accounting for the time it takes for the wake to be advected this distance by the ambient air. Figure 6.13(c) shows that the wake expansion timescale increases significantly as the perturbation caused by changing blade pitch propagates downstream. This increase in timescale is caused by the phenomenon depicted in figure 6.12(a) and (b). When the blade pitch increases, the maximum reduction in wake diameter occurs after the bulge caused by the velocity differences in the upwind and downwind portions of the wake passes. This bulge increases the time between the start of the pitch change maneuver and $\delta_{\varphi,\tau}$, the point used to determine τ_φ (figure 6.14). When the blade pitch decreases, the narrowing of the wake causes the same lag in wake expansion timescale. On the other hand, the deflection timescale at $5D$ downstream does not change significantly from that at $0.18D$ downstream (figure 6.13d). Some increased scatter is observed, especially at the lower yaw rates, attributed to the relatively small inverse wake deflection at these yaw rates and the significant wake distortion discussed above, both of which lead to increased uncertainty in the definition of the wake deflection timescale.

6.4 Conclusions and discussion

The current study uses LES to model transient behaviours in the wake of a wind turbine in response to changes in blade pitch, incoming wind direction, and yaw angle. Changes in blade pitch result in changes in wake expansion that are consistent with the results

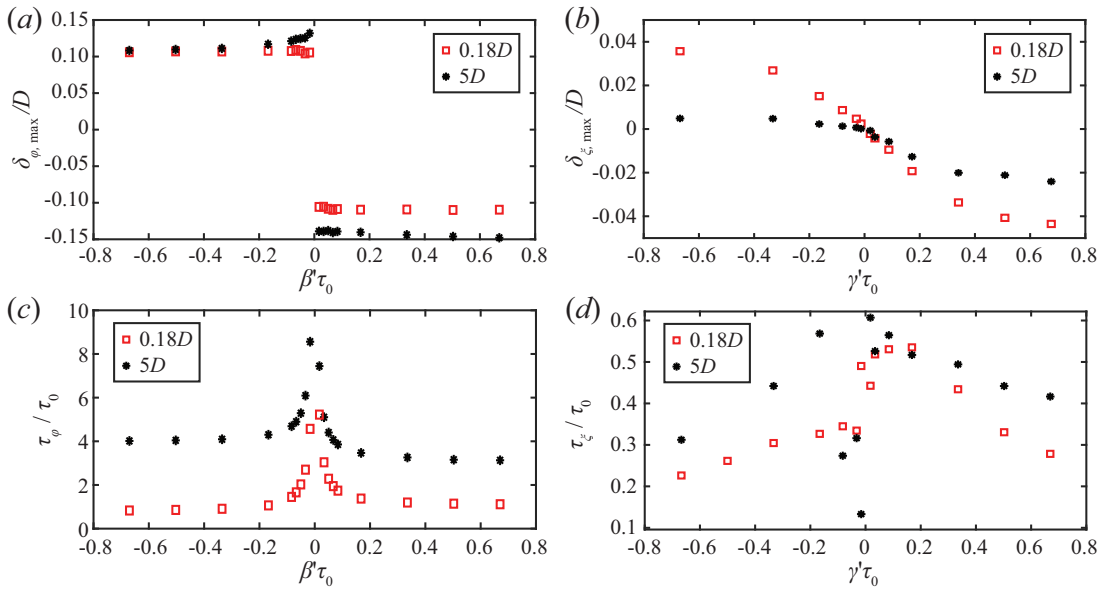

Figure 6.13: (a) Relationship between blade pitch rate and maximum wake expansion change at $0.18D$ and $5D$ downstream of the turbine. (b) Relationship between yaw rate and maximum inverse wake deflection at $0.18D$ and $5D$ downstream. (c) The effect of pitch rate on the wake expansion timescale at $0.18D$ and $5D$ downstream. (d) The effect of yaw rate on the inverse wake deflection timescale at $0.18D$ and $5D$ downstream.

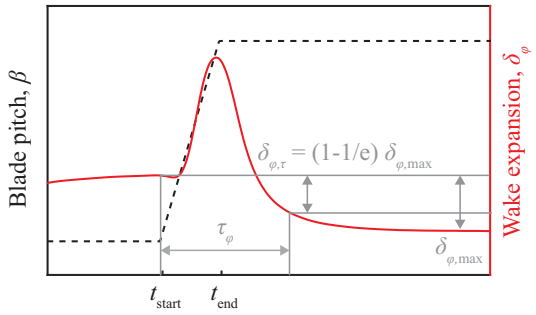

Figure 6.14: Sample change in blade pitch angle at a constant rate (dashed black line) and the resulting wake expansion response at $5D$ downstream (solid red line), with the wake expansion timescale, τ_φ, and maximum change in wake expansion, $\delta_{\varphi,\tau}$, defined in grey.

from the field study from Abraham and Hong [3]. The wake response to blade pitch changes displays hysteresis as a result of rotor and generator inertia, which causes a lag between changes in blade pitch and changes in tip speed ratio. The relationship between wake expansion and tip speed ratio exhibits the strongest dependence of the tested parameters, suggesting tip speed ratio is most responsible for changes in wake expansion. The lag between blade pitch and wake expansion changes is quantified for different pitch rates, showing that, though the maximum change in wake expansion depends on the magnitude of the pitch change, the time for the wake to stabilize varies significantly with pitch rate. Changes in wind direction are investigated to further elucidate the relationship between wake deflection and dynamic yaw misalignment observed in Abraham and Hong [3], which was opposite of the steady yaw misalignment response reported in previous studies (e.g., [1, 167, 168]). This behaviour is shown to depend strongly on the timescale of wind direction changes, with short-period changes (20 s) resulting in opposite wake deflection and long-period changes (50 s) demonstrating the steady wake deflection response. To separate the effects of turbine-modulated wake deflection from wake advection by the ambient flow, changes in rotor angle with a constant wind direction are investigated. The wake takes longer to reach the steady yaw response when the rotor angle is changed as a result of the removal of the wake advection effect. When the yaw rate is changed, a tradeoff is observed between inverse wake deflection time and magnitude. The mechanism behind the transient inverse wake deflection is elucidated

by quantifying changes in streamwise vorticity in different parts of the wake. In the top-left quadrant, the vorticity increases during the yaw maneuver, while it decreases in the bottom-right quadrant, inducing a period of positive spanwise velocity. These behaviours are caused by changes in the relative velocities of each part of the rotor and the resulting change in projection angle of the blade tip vortices. Finally, these near-wake behaviours are shown to propagate downstream to the far wake. The wake expansion timescale increases as the perturbation induced by the blade pitch change is advected downstream, while the wake deflection timescale remains largely unchanged.

The results of the current study provide insight into the wake behaviour of utility-scale wind turbines operating under atmospheric conditions, enabling more accurate modelling and prediction of the real-world wake. They explain phenomena previously observed in high-resolution field scale wake data. Furthermore, they have significant implications for recently proposed dynamic flow control strategies. One such strategy is the regulation of the thrust coefficient of each turbine in a wind farm, e.g., by modifying the blade pitch, to optimize the overall farm power generation [111, 142, 113]. This method can also be applied for power tracking, allowing wind farms to provide additional grid services [130]. Another strategy for wind farm optimization is adaptive yawing to dynamically deflect wind turbine wakes away from downstream turbines [143, 144, 145]. Munters and Meyers [119] proposed combining these two strategies to fully optimize wind farm power output, and Kanev et al. [148] included fatigue loading considerations to maximize overall wind farm lifetime. However, the aforementioned studies did not provide detailed analyses of the timescales of the proposed dynamic wake changes. In order to effectively implement these novel wake control strategies by dynamically varying parameters such as blade pitch and rotor yaw, the transient wake response must be included in the models used to develop such algorithms. The current study shows that the wake consistently takes time on the order of D/U_∞ ($\sim$10 s for the setup presented here) to reach a steady response. Therefore, wake changes with timescales shorter than this cannot be implemented effectively. This limitation is determined by the physical timescales of the vorticity in the wake and the inertia of the rotor.

Dynamic wake modulation is expected to enhance wake recovery downstream due to the fluctuations of the near-wake boundary by an average 11% increase in energy flux

into the wake, as discussed in [3]. Though turbulence still dominates wake recovery, dynamic wake modulation provides a significant contribution. Munters and Meyers [112], Yilmaz and Meyers [113], and Frederik et al. [173] exploited dynamic wake behaviors to further enhance wake breakdown and accelerate recovery. Brown et al. [175] also showed that dynamically varying the blade pitch and rotor speed excites unstable blade tip vortex modes, accelerating breakdown. The results of the current study additionally suggest that these dynamic wake modulations persist into the far wake where they can further impact on wake mixing. Furthermore, when the rotor misalignment angle changes, the resulting asymmetry of the blade tip vortices is expected to accelerate tip vortex breakdown. Tip vortex breakdown is typically induced by the development of instabilities in the vortex helix, particularly by the mutual inductance (vortex pairing) instability [62, 79, 58, 64, 24]. The fundamental study of Ortega et al. [176] and the modal decomposition investigation of Sarmast et al. [64] show that asymmetric vortex configurations destabilize faster than symmetric configurations. As tip vortex breakdown is the first step of wake recovery, the tip vortex asymmetry due to rotor misalignment will contribute to the enhanced wake recovery caused by dynamic wake modulation.

The asymmetric wake response to changes in rotor misalignment is also expected to contribute to wake meandering. Currently, two mechanisms have been proposed in the literature to understand wake meandering: the dynamic wake meandering (DWM) model which considers the wake to be a passive tracer advected by large-scale atmospheric motions, and the idea that the rotor acts like a bluff body shedding vortices [177]. Both of these frameworks treat the turbine as a passive structure, but our results show that the wake deflection is actively modulated by the turbine. In the field, the yaw misalignment between the rotor and wind is constantly changing due to the constant changes in wind direction, which leads to continual changes in wake deflection. These turbine-modulated wake deflections will be superimposed on any meandering caused by advection or bluff body vortex shedding.

The findings of the current study also have implications for turbines undergoing tilt angle changes. These tilt changes can be induced either by the rocking motion of ocean waves for offshore floating turbines [178] or by active wake control [179, 180]. Previous studies have shown that the magnitude of wake deflection in the vertical direction

during rotor tilt is comparable to spanwise wake deflection during yaw [181], and that the counter-rotating vortex mechanism responsible for inducing steady-state spanwise wake deflection is also responsible for tilt-induced vertical wake deflection [180]. These similarities in steady-state behaviors suggest analogous dynamic wake behaviors would result from dynamic tilt changes. For floating offshore turbines, all tilt changes are dynamic, as wave-induced motions are inherently oscillatory. Alternatively, dynamic tilt-based control algorithms could be proposed with the addition of the necessary mechanical components. Future studies may investigate whether the potential benefits of such a control method outweigh the added cost of implementation.

Finally, we acknowledge that the current study investigates the wake of a single example turbine. We expect the qualitative trends described here to hold true regardless of turbine design, but we caution the reader that the quantitative measures may not translate directly to other turbines. Future work can investigate the potential impact of turbine size, geometry, rotation direction, and siting on the observed phenomena. Additionally, the wake behavior was studied under uniform inflow in order to isolate the effects of each parameter changed individually. However, the effect of such atmospheric phenomena as wind shear and veer can be investigated in future studies. More significantly, turbulence has not been included in the current study. Though the near wake is dominated by the coherent structures shed from the turbine, atmospheric turbulence dominates far-wake behaviour in the field [174]. Therefore, the direct applicability of the downstream dynamic wake modulation propagation analysis to wind turbines operating under real-world conditions is limited. As discussed in Section 6.3.5, this far-wake analysis adds primarily theoretical value for idealized conditions.

Chapter 7

The effect of dynamic near-wake modulation on utility-scale wind turbine wake development

The content of this chapter has been published by the author in *Journal of Physics: Conference Series* [182]. Content has been reprinted here with permission.

7.1 Introduction

Improved understanding of wind turbine wake development is required to mitigate the undesirable wake effects of power loss and increased fatigue loading on downwind turbines. In particular, wake recovery caused by re-entrainment of energy through mixing across the wake boundary is critical for increasing the amount of energy available to downwind turbines in a wind farm. It has been well established that several factors can influence wake recovery, including blade tip vortex breakdown [24], wind farm layout [22], and atmospheric stability [98]. Only recently, the effect of turbine operation on wake development has been investigated. Specifically, recent studies have proposed maximizing overall wind farm power by continuously regulating the thrust coefficient of each turbine, reducing the strength of the wake velocity deficit [109, 110, 111]. Two studies by Meyers and colleagues [112, 113] modelled in-line turbines with time-varying

thrust coefficients to find the optimal time sequence for inducing wake breakdown before it reaches the downwind turbine. Another method of wake control is yaw steering, where a misalignment between the rotor and wind direction is applied to deflect the wake in the spanwise direction [1]. Though this method has achieved preliminary success in field tests on an operational wind farm [120], some discrepancies have been observed between the predicted and observed wake deflection [116, 117]. These discrepancies suggest a lack of fundamental understanding of the mechanisms governing this behavior, likely caused by limitations of the techniques used to study it. Laboratory, numerical, and analytical methods must simplify turbine geometry, operational response, and/or atmospheric conditions to predict wake development. Field scale measurement techniques, meanwhile, lack sufficient spatiotemporal resolution to resolve coherent structures and instantaneous wake behavior.

To address the aforementioned limitations, Hong et al. [17] introduced super-large-scale flow visualization using natural snowfall to observe and quantify the flow in the wake of a utility-scale wind turbine. This technique provides high-resolution images of the wake with a field of view up to 100 m and has enabled the identification of several previously unobserved dynamic near-wake phenomena. Hong et al. [17] first characterized the relationship between the behavior of vortices shed from the blade tips and turbine operation. Dasari et al. [5] applied the technique to measure the flow over the entire vertical extent of the wake, identifying intermittent periods of wake contraction related to changes in blade pitch for the first time. Abraham et al. [49] investigated the effect of the tower and nacelle on the near-wake and the changes in their influence in response to changes in incoming flow. Most recently, Abraham and Hong [3] presented the first investigation into dynamic wake modulation, the large-scale motion of the wake in response to instantaneous changes in turbine operation and atmospheric conditions. Significantly, this study demonstrated the impact of dynamic wake modulation on mixing across the near-wake boundary and showed that it can contribute up to 20% more energy flux and an average of 11% more than that calculated without considering dynamic effects. The current study further investigates the impact of dynamic wake modulation on wake mixing and recovery by combining high-resolution field data with high-fidelity large eddy simulations (LES). The inclusion of LES enables

the quantification of the wake behavior at multiple different planes simultaneously, particularly at distances farther downstream than those that can be captured in field-scale flow visualization experiments.

7.2 Methods

To develop further understanding of dynamic wake modulation and to isolate the effect of individual parameters, large eddy simulations (LES) of the Eolos turbine and its wake were conducted. The simulations were performed with Nalu-Wind, a wind-focused fork of the incompressible flow solver developed by Sandia National Laboratories, Nalu [14]. A model of the turbine was developed in OpenFAST and incorporated into the LES using actuator lines [157]. To isolate the influence of dynamic wake modulation associated with changing turbine operation and incoming flow conditions, the simulations were first conducted using uniform laminar inflow with a wind speed of 10 m/s. The changing turbine operation was implemented by modifying the turbine controller with a hard-coded time series of pitch rates, as blade pitch was shown to be one of the main contributors to changes in wake expansion and contraction [5, 3]. The blade pitch was varied linearly at 5 different rates, for 10 seconds each in the positive and negative directions (figure 7.1a). The rotor speed started at 14.7 RPM but was allowed to change in response to changes in blade pitch. Changing incoming flow conditions were modelled by sinusoidally varying the wind direction with increasing magnitude (maximum of 20°, figure 7.1b) while the rotor yaw angle was held constant. These time series were selected to approximately match the magnitudes and rates of change of the blade pitch and wind direction from the field experiment in a more organized and controlled pattern than that observed in the field.

Simulations with turbulent inflow were performed next to explore the effects of dynamic wake modulation under more realistic conditions. The turbulent flow was generated in a 2500 m $\times$ 2500 m $\times$ 500 m volume using a precursor simulation with periodic boundary conditions in the streamwise and spanwise directions. The top surface was capped with an inversion layer and a shear stress boundary condition was applied to the bottom surface using the logarithmic law for rough walls with a friction velocity of $u^* = 0.95$ m/s and a roughness length of $z_0 = 0.53$ m. The turbulence was allowed

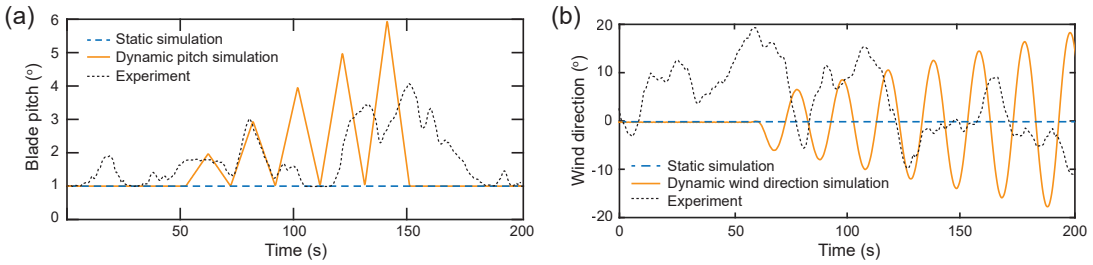

Figure 7.1: Time series of (a) blade pitch and (b) wind direction for the static and dynamic simulations compared to a sample time sequence from the field experiment.

to develop for 20000 s in order to reach a quasi-steady equilibrium state. Then the simulation was run for another 2000 s to generate a fully developed turbulent inflow boundary condition for the turbine simulation.

7.3 Results

7.3.1 Far wake mixing under uniform flow

Figure 7.2 shows the wake under the three uniform flow conditions, with cross-sections showing the mean streamwise velocity at three downstream distances. Both dynamic cases show accelerated wake recovery compared to the static case, indicated by the increased spread and reduced magnitude of the velocity deficit. These features are clearest at the farthest downstream distance ($7D$), but can also be observed closer to the turbine. The dynamic cases also exhibit deformed wake boundaries, indicating that the boundary deformation is intrinsically related to the accelerated wake recovery. This connection is particularly clear in the dynamic wind direction case where the wake boundary is significantly disturbed and the velocity deficit reduction is the strongest.

The accelerated wake recovery is caused by enhanced energy flux into the wake, quantified in figure 7.3 for both dynamic cases at $7D$ downstream (the typical turbine spacing in current wind farms [131]). The energy flux per unit length, calculated as $\Phi = \overline{u}_x \langle u'_x u'_r \rangle_{r=D/2}$, increases with the magnitude of the pitch changes and wind direction changes, as they cause fluctuations in the wake boundary that enhance the mixing across the boundary. The energy flux from the dynamic cases is compared to that from the static case, where it stays constant near zero (no turbulent mixing occurs in this uniform

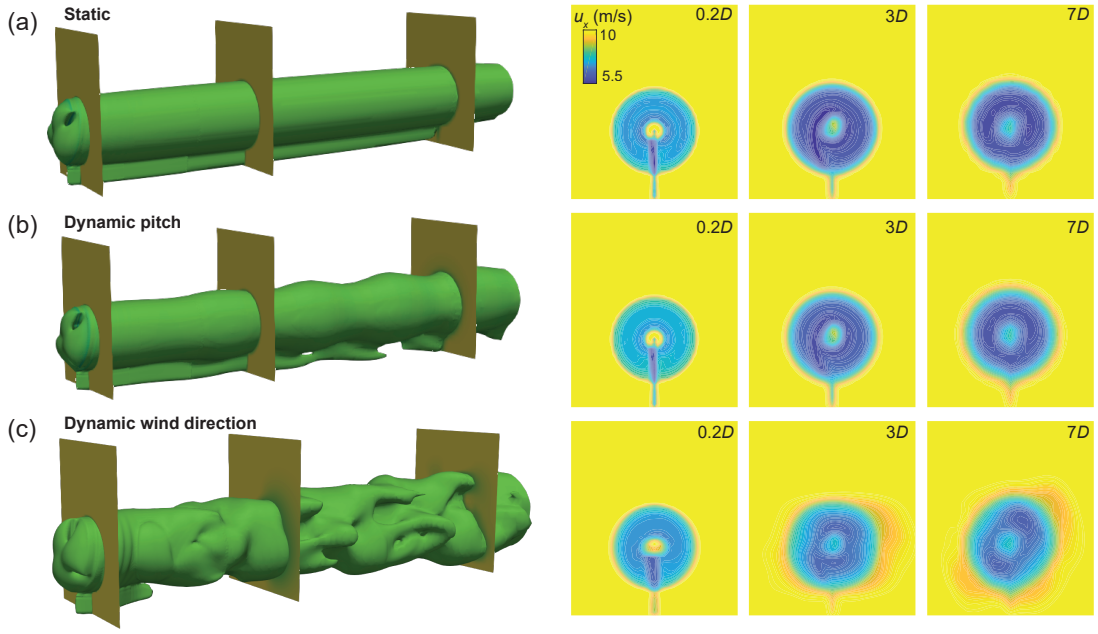

Figure 7.2: Sample instantaneous isocontours of velocity (u_x = 9 m/s) from (a) the static uniform inflow simulation, (b) the dynamic pitch uniform inflow simulation, and (c) the dynamic wind direction uniform inflow simulation with cross-sections showing mean streamwise velocity at three downstream locations.

flow simulation).

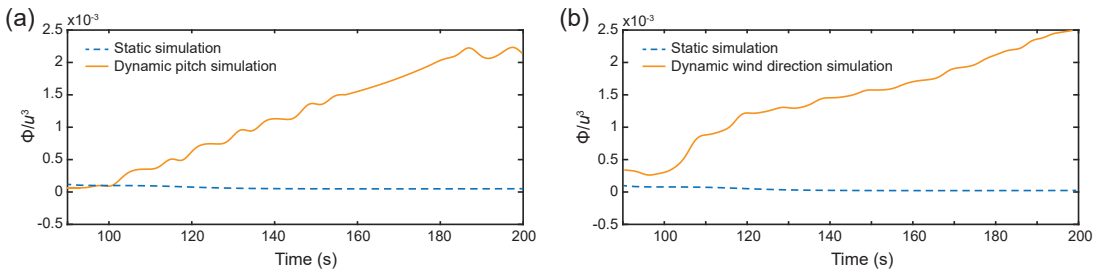

Figure 7.3: (a) Energy flux per unit length into the wake for the static uniform flow simulation and the dynamic pitch uniform flow simulation. (b) Energy flux per unit length into the wake for the static uniform flow simulation and the dynamic wind direction uniform flow simulation. Note that the delay in the start of the signal is due to wake propagation time.

7.3.2 Far wake mixing under turbulent flow

Dynamic wake modulation is next simulated with turbulent inflow to obtain a more realistic understanding of how this modulation affects wake mixing in the atmospheric conditions experienced by utility-scale turbines. With the turbulent inflow, only dynamic pitch is simulated, as the stochasticity of the atmospheric wind direction cannot be readily incorporated into the turbulent simulation at this point. The same blade pitch sequence used in the uniform flow simulation (figure 7.1a) is applied here. Figure 7.4 compares the wake in the static and dynamic pitch cases. It is immediately apparent that the turbulent inflow substantially deforms the wake boundary and enhances mixing compared to the uniform inflow case, accelerating wake recovery. By the time the wake reaches $7D$ downstream, significant recovery has occurred in both the static and dynamic pitch cases. However, some differences between the two cases can still be observed. In the $3D$ and $7D$ planes, the velocity deficit is slightly weaker for the dynamic pitch case than the static pitch case. This finding suggests that dynamic wake modulation still enhances mixing, even under the high-flux conditions of turbulent inflow.

The aforementioned effect is again quantified using the energy flux at the wake boundary $7D$ downstream, shown in figure 7.5 for the static and dynamic pitch cases.

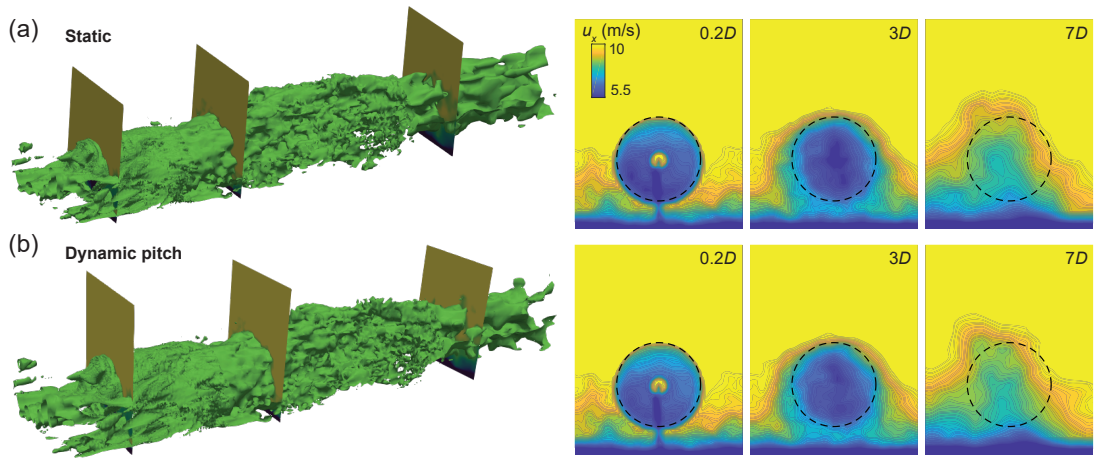

Figure 7.4: Sample instantaneous isocontours of velocity (u_x = 9 m/s) from (a) the static turbulent inflow simulation and (b) the dynamic pitch turbulent inflow simulation with cross-sections showing mean streamwise velocity at three downstream locations. The dashed circle indicates the rotor position.

Though the magnitudes are much closer than in the uniform flow cases, dynamic pitch still enhances mixing across the boundary by an average of 12%. This value is comparable to that reported in the experimental study for the estimated effect of dynamic wake modulation on energy flux in the near wake [3]. Significantly, the pitch changes modelled in the current study are on the same order as those that occur during normal above-rated turbine operation (as demonstrated in figure 7.1a), so the observed enhanced mixing is already occurring frequently in the wake of utility-scale turbines.

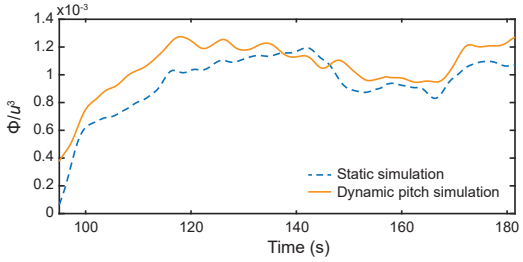

Figure 7.5: Energy flux per unit length into the wake for the static turbulent flow simulation and the dynamic pitch turbulent flow simulation.

Figure 7.5 also shows that the flux enhancement is not constant. There is even a

period where the dynamic pitch case exhibits a lower flux than the static pitch case. The intermittency of the flux enhancement suggests that the dynamic wake modulation may be interacting with another unsteady process in the far-wake, i.e., wake meandering. Figure 7.6 provides further support for this interpretation, comparing top-view cross-sections of the static and dynamic pitch cases at two time points. The first time point (figures 7.6a and b) provides an explanation for the decreased flux observed in the dynamic pitch case. At $\sim 6D$ downstream, a region of the dynamic pitch wake has an increased velocity deficit compared to the static pitch wake, though the inflow in both cases is the same. This observation suggests wake meandering and dynamic wake modulation have a destructive relationship at that moment, inhibiting wake mixing and breakdown. However, throughout most of the simulation these two phenomena appear to have a constructive relationship, working together to enhance mixing. A second time point is shown in figures 7.6(c) and (d), where the wake exhibits a turn at $\sim 5D$ downstream, indicated by the white arrow in the figure. At this point, the velocity deficit is significantly lower in the dynamic pitching case than in the static pitching case, suggesting dynamic wake modulation augments the mixing caused by meandering. This constructive relationship likely occurs most of the time, as the average mixing during the dynamic pitch simulation is higher than that in the static pitch simulation.

7.4 Conclusions and discussion

High-fidelity LES was combined with field scale experiments to investigate the effect of dynamic turbine operation and atmospheric conditions on mixing and recovery in the wake of a 2.5 MW wind turbine. The novel high-resolution flow visualization technique using natural snowfall enabled the quantification of instantaneous near-wake expansion and deflection, termed dynamic wake modulation, in response to changes in blade pitch and wind direction. Simulations were performed to isolate these variables, and the same trends as those observed in the experiments were revealed. Further, energy flux into the wake $7D$ downstream was calculated, showing dynamic turbine-atmospheric interactions enhance mixing in the far-wake. This finding was demonstrated under both uniform and turbulent inflow conditions. Under turbulent flow, a synergistic relationship was observed between dynamic wake modulation and wake meandering, as wake recovery

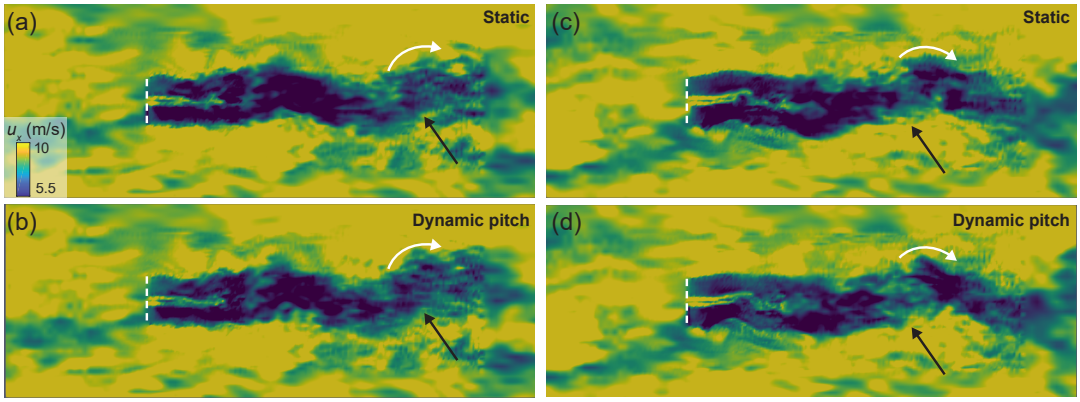

Figure 7.6: Interaction between dynamic wake modulation and meandering in turbulent flow. Sample streamwise velocity field at plane $z = H_{\text{hub}}$ during the same instant for the (a) static pitch simulation and (b) dynamic pitch simulation. Sample streamwise velocity field at plane $z = H_{\text{hub}}$ during a second time for the (c) static pitch simulation and (d) dynamic pitch simulation. The dashed white line indicates the position of the rotor and the black arrow points to the location where a significant difference in velocity deficit between the two cases can be observed. The white curved arrow highlights the turning motion of the wake due to meandering.

was further accelerated when the two phenomena occurred together.

The current study is limited to neutrally stable atmospheric conditions because of the restrictive weather conditions under which the flow visualization experiments can take place (i.e., during snowstorms). In future studies, additional atmospheric stabilities will be investigated using simulations to understand the effect of this variable on the enhanced mixing caused by dynamic wake modulation. Furthermore, we were unable to simulate the large-scale changes in wind speed and direction that occur in the atmosphere. Though this atmospheric stochasticity is a crucial aspect of dynamic wake modulation, it is notoriously difficult to model in simulations [8]. One way to address this limitation would be to couple atmospheric flow simulations at different scales (e.g., mesoscale and microscale), an avenue which will be explored in future studies.

The results of the current study can be applied to the development of more realistic far-wake models. Currently, dynamic wake modulation is not considered in conventional wake models, though we have demonstrated here that it can have a significant impact on wake mixing and development. Improved wake models will allow wind farm layouts

to be designed more efficiently, reducing the levelized cost of wind energy. Additionally, the findings from the current study can be used to develop advanced control algorithms to speed up wake breakdown and recovery, further improving wind farm efficiency.

Chapter 8

Improving wind farm power prediction by including dynamic wake modulation

8.1 Introduction

Wind farm power prediction improvements are urgently needed in the wind energy industry. Currently, median annual energy production predicted by wind farm developers exceeds actual performance by 3.5-4.5% on average [9]. This overprediction bias poses a significant risk to wind energy projects, as energy buyers may have the option to terminate their contract if a project produces less energy than the predicted amount [9]. More accurate wind farm power prediction models would also facilitate improved wind farm layout optimization, further increasing power generation [170]. Furthermore, with power prediction at short timescales, wind farms would be able to provide grid services such as power scheduling [183].

Wind turbine wakes are one of the primary sources of wind farm power loss and uncertainty, leading to up to 20% total energy production loss and 10% plant performance uncertainty [9]. During the wind farm planning process, simplified analytical models are typically used in the layout optimization and loss estimation stages to approximate the width, depth (i.e., velocity deficit), and extent of turbine wakes [184]. Because

site optimization is computationally intensive, the wake models used must be simple to minimize computational expense. However, these simple models do not include all of the relevant physical phenomena, resulting in uncertainties as high as 50% of the loss [184]. To reduce such uncertainty and improve power predictions, additional behaviors exhibited by utility-scale turbine wakes must be included in wake models.

In the field, utility-scale turbines actively interact with the atmospheric flow, dynamically modulating the wakes [3]. However, most simplified wake models used for wind farm power prediction (e.g., Jensen, Park, Larsen) assume steady-state conditions. One notable exception is the dynamic wake meandering (DWM) model, which accounts for wake advection by large-scale turbulent flow structures [114]. An additional advantage of the DWM model is that it provides a unified approach for modeling loading on downstream turbines in addition to power generation [114]. The DWM model falls short, however, in modeling the wake as a passive tracer, without accounting for the active modulation from the turbine.

In the current study, we propose modifications to the DWM model to account for dynamic wake modulation. First, we explain how the changes are implemented in Fast.FARM [185], an open-source wind farm modeling software. Next, we assess the advantages of using the modified DWM model for wind farm power prediction.

8.2 Methods: FAST.Farm modifications

FAST.Farm is an open-source wind farm modeling tool developed by NREL [185]. The software uses OpenFAST [14] to model each turbine and has additional modules to solve for the wind farm wide flow and wake behaviors. The option to define a super controller for the entire wind farm is also provided. Here we focus on the wake dynamics module, which calculates the wake velocity at a series of discrete cross-sectional planes that are advected with the ambient wind. The following submodels are included in the wake dynamics module: wake advection, deflection, and meandering; near-wake correction, and wake-deficit increment. The wake-deficit increment submodel uses the thin shear-layer approximation of the Reynolds-average Navier Stokes equations to calculate the wake velocity at each plane [186]. The eddy viscosity formulation used for turbulence closure accounts for wake mixing due to ambient turbulence and the wake shear layer

[187]:

$$\nu_T(x,r) = F_{\nu\mathrm{Amb}}(x) k_{\nu\mathrm{Amb}} \, {}^{\mathrm{Filt}}TI_{\mathrm{Amb}} \, {}^{\mathrm{FiltDiskAvg}}V_x^{\mathrm{Wind}} \frac{{}^{\mathrm{Filt}}D^{\mathrm{Rotor}}}{2} + F_{\nu\mathrm{Shr}}(x) k_{\nu\mathrm{Shr}} MAX \left[\left(\frac{D^{\mathrm{Wake}}(x)}{2} \right)^2 \left| \frac{\partial V_x}{\partial r}(x,r) \right|, \frac{D^{\mathrm{Wake}}(x)}{2} MIN|_r \{V_x(x,r)\} \right] \tag{8.1}$$

where $F_{\nu\mathrm{Amb}}(x)$ and $F_{\nu\mathrm{Shr}}(x)$ are the filter functions for ambient turbulence and wake shear, respectively, to account for streamwise changes in strength; $k_{\nu\mathrm{Amb}}$ and $k_{\nu\mathrm{Shr}}$ are coefficients weighting the relative strength of the two effects on eddy viscosity; ${}^{\mathrm{Filt}}TI_{\mathrm{Amb}}$ is the low-pass time filtered ambient turbulence intensity; ${}^{\mathrm{FiltDiskAvg}}V_x^{\mathrm{Wind}}$ is the time filtered ambient wind speed normal to the rotor, averaged over the rotor area; and $\frac{{}^{\mathrm{Filt}}D^{\mathrm{Rotor}}}{2}$ is the time filtered rotor radius (note that the rotor diameter can change slightly due to blade deflections). The eddy viscosity for the wake shear layer uses the maximum of two different methods, both of which use the wake cross-section half-width ($\frac{D^{\mathrm{Wake}}(x)}{2}$). The first depends on the magnitude of the streamwise velocity gradient in the radial direction ($\left|\frac{\partial V_x}{\partial r}(x,r)\right|$) and the second depends on the minimum streamwise velocity along the radius at a given downstream distance ($MIN|_r\{V_x(x,r)\}$).

To account for the added mixing contributed by dynamic wake modulation, we propose an additional eddy viscosity term:

$$\nu_{T\mathrm{Dyn}}(x,r) = \begin{cases} k_{\nu\mathrm{Dyn},z}(1 - C_T[n_{\mathrm{Gen}}]) \\ +F_{\nu\mathrm{Dyn},y}(x) k_{\nu\mathrm{Dyn},y} \left\langle \left| \frac{\partial V_y}{\partial x} \right|_{x=0, r<D/2} [n_{\mathrm{Gen}}] \right\rangle & r = \frac{D^{\mathrm{Wake}}(x)}{2} \\ 0 & r \neq \frac{D^{\mathrm{Wake}}(x)}{2} \end{cases} \tag{8.2}$$

This term is divided into two cases because dynamic wake modulation only acts at the wake boundary, $r = \frac{D^{\mathrm{Wake}}(x)}{2}$ — elsewhere it is 0. The added eddy viscosity has two terms, one for the vertical direction and one for the spanwise direction. The eddy viscosity term for vertical wake modulation includes a weighting coefficient ($k_{\nu\mathrm{Dyn},z}$) and dependence on the turbine thrust coefficient, C_T. The relationship with the thrust coefficient is based on the field-scale experimental data from Abraham and Hong [3]. As shown in figure 8.1, a strong inverse relationship is observed between C_T and the vertical component of the additional flux induced by dynamic wake modulation. Therefore, the eddy viscosity is expected to increase at the wake boundary when C_T decreases for the

range of C_T typical of an operational utility-scale turbine. Note that this term does not include a filter function, as the results of Sections 6.3.5 and 7.3.2 show that the strength of dynamic wake expansion does not change significantly with downstream propagation. Even under turbulent conditions, the mean added flux caused by vertical dynamic wake modulation is found to be $\sim 12\%$ of the momentum flux without dynamic wake modulation at both $0.18D$ [3] and $7D$ [182] downstream.

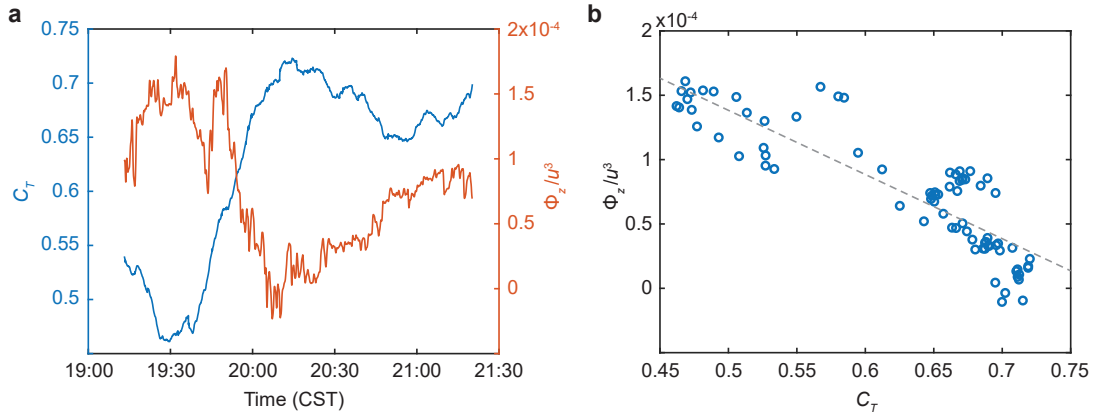

Figure 8.1: Relationship between the vertical component of momentum flux induced by dynamic wake modulation (Φ_z) normalized by u^3 and turbine thrust coefficient (C_T). (a) Time series of both variables over the duration of the field-scale experimental dataset from Abraham and Hong [3]. (b) Scatter plot of Φ_z/u^3 versus C_T where each data point represents the average of 100 s of data. A linear least-squares fit line is shown as a dashed gray line.

The term for the added eddy viscosity due to spanwise wake modulation includes a filter function ($F_{\nu\mathrm{Dyn},y}(x)$), a weighting coefficient ($k_{\nu\mathrm{Dyn},y}$), and dependence on the magnitude of the spanwise velocity gradient at the rotor and averaged over the rotor area ($\left\langle \left| \frac{\partial V_y}{\partial x} \right|_{x=0,r<D/2} \right\rangle$). The relationship with the spanwise velocity gradient is based on the dependence of spanwise dynamic wake modulation on changes in wind direction relative to the rotor. Figure 8.2 shows that the spanwise component of added momentum flux follows some of the fluctuations in the velocity gradient magnitude at the rotor, though it does not reflect all of the changes, particularly the larger scale trends. This discrepancy is attributed to the effects of dynamic wake meandering, wherein the large-scale changes in wind direction advects the wake after it leaves the rotor. This dynamic wake meandering effect is already included in the FAST.Farm wake advection, deflection,

and meandering submodel.

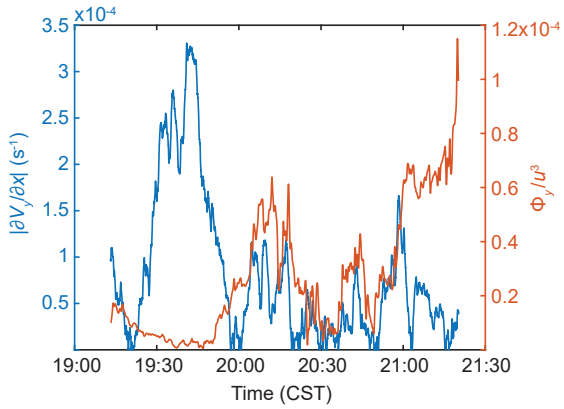

Figure 8.2: Relationship between the spanwise component of momentum flux induced by dynamic wake modulation (Φ_y) normalized by u^3 and the magnitude of the spanwise velocity gradient at the rotor ($\left|\frac{\partial V_y}{\partial x}\right|$) shown as a time series of both variables over the duration of the field-scale experimental dataset from Abraham and Hong [3]

The filter function, $F_{\nu\mathrm{Dyn},y}(x)$, is of a similar form to those in equation 8.1:

$$F_{\nu\mathrm{Dyn},y}(x) = \begin{cases} 1 & x \leq C_{\nu\mathrm{Dyn}}^{\mathrm{DMin\ Filt}} D^{\mathrm{Rotor}} \\ C_{\nu\mathrm{Dyn}}^{\mathrm{FMin}} & \\ +(1 - C_{\nu\mathrm{Dyn}}^{\mathrm{FMin}}) \left[\frac{\frac{x}{\mathrm{Filt}\, D^{\mathrm{Rotor}}} - C_{\nu\mathrm{Dyn}}^{\mathrm{DMin}}}{C_{\nu\mathrm{Dyn}}^{\mathrm{DMax}} - C_{\nu\mathrm{Dyn}}^{\mathrm{DMin}}} \right]^{C_{\nu\mathrm{Dyn}}^{\mathrm{Exp}}} & C_{\nu\mathrm{Dyn}}^{\mathrm{DMin\ Filt}} D^{\mathrm{Rotor}} < x < C_{\nu\mathrm{Dyn}}^{\mathrm{DMax\ Filt}} D^{\mathrm{Rotor}} \\ C_{\nu\mathrm{Dyn}}^{\mathrm{FMin}} & x \geq C_{\nu\mathrm{Dyn}}^{\mathrm{DMax\ Filt}} D^{\mathrm{Rotor}} \end{cases} \tag{8.3}$$

where $C_{\nu\mathrm{Dyn}}^{\mathrm{DMin}}$, $C_{\nu\mathrm{Dyn}}^{\mathrm{DMax}}$, $C_{\nu\mathrm{Dyn}}^{\mathrm{FMin}}$, and $C_{\nu\mathrm{Dyn}}^{\mathrm{Exp}}$ are user-specified parameters. The primary difference between equation 8.3 and the other filter functions in equation 8.1 is that $F_{\nu\mathrm{Dyn},y}(x)$ is strongest near the rotor and weakens farther downstream, whereas $F_{\nu\mathrm{Amb}}(x)$ and $F_{\nu\mathrm{Shr}}(x)$ strengthen as the wake moves downstream. The results of section 6.3.5 show that spanwise dynamic wake modulation weakens as it propagates downstream, while the effects of shear and ambient turbulence strengthen [24].

Because dynamic wake modulation only occurs at the rotor and is then advected downstream, both C_T and $\left\langle \left| \frac{\partial V_y}{\partial x} \right|_{x=0, r<D/2} \right\rangle$ must be evaluated at the wake generation time, n_{Gen}, in equation 8.2 for each downstream wake plane. The wake generation time

is defined as:

$$n_{\text{Gen}} = n - \left(\frac{x_{n_p}^{\text{Plane}}}{\Delta t \, {}^{\text{FiltDiskAvg}}V_{x_{n_p}}^{\text{Wind}}} \right) \tag{8.4}$$

where n is the current time step, $x_{n_p}^{\text{Plane}}$ is the downstream distance of the wake plane from the rotor, Δt is the duration of a single time step, and ${}^{\text{FiltDiskAvg}}V_{x_{n_p}}^{\text{Wind}}$ is the time-filtered rotor-averaged streamwise ambient wind speed at the wake plane. The necessity of evaluating the aforementioned variables at the wake generation time requires that the full time series of each be stored throughout the simulation for every turbine.

Finally, magnitude of the weighting coefficients $k_{\nu\text{Dyn},z}$ and $k_{\nu\text{Dyn},y}$ must be discussed. The results of section 5.3.3 show that the added vertical and spanwise momentum flux due to dynamic wake modulation range from about 0-50% and 0-10%, respectively, of the momentum flux into the wake recorded in a previous LES study. The LES study included the effects of ambient turbulence and wake shear, but did not account for dynamic wake modulation [2]. Figure 8.1 shows that the maximum added vertical flux occurs at $C_T \sim 0.5$. This maximum flux corresponds to ∼50% of the flux caused by shear and turbulence (see figure 5.6). Therefore, $k_{\nu\text{Dyn},z}$ should be approximately equal to the average value of $\nu_{T\text{Amb}} + \nu_{T\text{Shr}}$. In the spanwise case, added flux of $\sim 10\%$ occurs when $\left| \frac{\partial V_y}{\partial x} \right| \sim 6 \times 10^{-5}$ (see figure 8.2. Therefore, $k_{\nu\text{Dyn},y}$ should be approximately equal to the average value of $\frac{0.1}{6\times10^{-5}}(\nu_{T\text{Amb}} + \nu_{T\text{Shr}}) = 1.7 \times 10^3(\nu_{T\text{Amb}} + \nu_{T\text{Shr}})$. For reference, the default values of $k_{\nu\text{Amb}}$ and $k_{\nu\text{Shr}}$ in Fast.FARM are 0.05 and 0.014, respectively [188].

8.3 Discussion

Though evaluation of the aforementioned modifications has not yet been performed, we expect the inclusion of dynamic wake modulation in FAST.Farm to improve the accuracy of its wind farm power predictions. As shown in figure 8 of Stevens and Meneveau [134], all conventional wind farm models underestimate the amount of mixing occurring within the farm, evidenced by underprediction of power in strongly waked wind directions and overprediction in unwaked directions. When FAST.Farm power predictions are compared to SCADA data from a group of five utility-scale wind turbines, the average percent error under waked conditions is 15.5% for below-rated wind speeds and 7.1%

overall [189]. The added mixing caused by dynamic wake modulation is expected to account for some of these discrepancies. Dynamic wake modulation is expected to be particularly important under low turbulence conditions, as turbulent mixing will be weaker. Because turbulence tends to be weaker at lower wind speeds, the dominance of dynamic wake modulation could be the source of the larger error for below-rated wind speeds in FAST.Farm mentioned above. Furthermore, offshore wind is characterized by lower turbulence than that over land [56], and the recent focus on offshore wind in the United States suggests that including dynamic wake modulation in wind farm models is now more important than ever to achieve accurate power predictions.

Though the modifications discussed in section 8.2 are expected to improve wind farm power predictions using FAST.Farm, this method has some significant limitations. First and foremost, several user-specified parameters are required to run FAST.Farm, and the dynamic wake modulation modifications add a few more. Selecting the values for these parameters requires both a clear understanding of how they influence wake dynamics and high-fidelity simulations for calibration [188]. Though studies have shown that FAST.Farm compares well with LES results for cases that were not used to calibrate the parameters [190], it is not yet clear under which circumstances new calibration would be required. In addition, relatively high resolution wind speed data is required to model the inflow to the wind farm, which may not be available at all sites. Instead, users may be required to make assumptions about the wind conditions, generating additional uncertainty.

Chapter 9

Operational-dependent wind turbine wake impact on surface momentum flux

The content of this chapter has been published by the author in *Renewable and Sustainable Energy Reviews* [47]. Content has been reprinted here with permission.

9.1 Introduction

As a renewable and affordable form of energy, wind power is growing rapidly, with a tenfold increase in demand and deployment expected by the year 2050 [8]. With such expansion will come increased interaction between wind turbines and their surroundings, particularly in the area of agriculture, as the richest land-based wind resources in the United States overlap with land used for growing most of the country's wheat and corn [191]. Wind turbines leave wakes behind them, regions characterized by lower wind speed and increased turbulence. Wakes influence the flux of momentum, heat, carbon dioxide, and water vapor between the ground surface and the atmosphere, which can have implications for the surrounding area in terms of biodiversity [192], water temperature of nearby lakes [193], ocean wave properties for offshore wind farms [194], and, most significantly for the United States, crop growth [191].

Several recent studies have investigated the interaction between wind turbine wakes and the ground surface. Using a model turbine in a wind tunnel, Chamorro and Porté-Agel [92] observed in the wake a reduction in shear and turbulence intensity relative to the incoming flow. In a follow-up study investigating the effect of boundary layer stability, the same authors found that the wake reduces momentum flux and increases heat flux near the surface when the boundary layer is stable (usually occurring at night), causing a temperature increase near the ground [75]. On the other hand, Lu and Porté-Agel [161] observed reductions of both surface momentum and heat fluxes in the wake of a wind turbine in a stable boundary layer, modelled with large eddy simulations. Zhang et al. [195] investigated the effect of a convective (unstable) boundary layer, which typically occurs during the day, finding that heat and momentum flux are both enhanced in this scenario, leading to cooling in the lower part of the wake. In a field-scale study, Smith et al. [196] observed negative shear and increased turbulence intensity in the wake at night, causing warming near the surface. Most recently, Archer et al. [197] conducted a field study of the wake effect of a single turbine, observing a reduction in momentum flux and turbulence near the ground surface, and no significant change in heat flux.

While the aforementioned studies focused on single turbine wakes, several others have investigated the overall effects of large wind farms using field measurements and numerical modeling approaches. The field-scale experimental studies are reviewed first. Baidya Roy and Traiteur [198] compared temperature data from meteorological towers upwind and downwind of a wind farm in California, observing warming at night and cooling during the day, attributed to enhanced mixing caused by the wind turbine wakes. Comparing land surface temperature data before and after construction of a wind farm in Texas, Zhou et al. [199] observed warming within the wind farm during the day and night, and cooling in a region nearby. Rajewski et al. [191] conducted measurements of fluxes in a central Iowa wind farm using lidars and moveable meteorological towers. They observed warming at night and cooling, downward CO2 flux, and upward moisture flux during the day.

Several modelling studies of wind farm impacts on the surrounding climate have also been conducted. Modelling turbines within a large wind farm as energy sinks and turbulent kinetic energy (TKE) sources, Baidya Roy et al. [200] observed air drying and

warming near the surface at night, with no significant changes during the day. Li et al. [201] modelled a large wind farm in the Sahara Desert as increased surface roughness, and found resulting regional increases in warming, precipitation, and vegetation. Miller and Keith [202] simulated a wind farm large enough to meet the energy needs of the Continental United States, and observed a resulting temperature increase within the farm, stronger at night than during the day, and no significant change in precipitation. Xia et al. [203] investigated the momentum sink and TKE generation properties of a wind farm separately, finding TKE responsible for strong warming within the wind farm and momentum sink responsible for weak cooling within and downwind of the farm.

To summarize, prior investigations into the impacts of wind farms on surface temperatures present inconsistent results. Though most find warming effects at night, several report warming during the day [199, 201, 202, 203], others record cooling during the day [191, 195, 198], and still others observe no significant change in daytime temperature [196, 197, 200]. These conflicting reports show a lack of fundamental understanding of the mechanism involved in the interaction between the wind turbine wake and the ground surface, caused by limitations in the techniques used to study the phenomenon. Laboratory-scale experiments and computational simulations do not capture the full complexity of utility-scale wind turbine behavior, including dynamic turbine operation and stochastic atmospheric conditions. On the other hand, conventional field-scale flow diagnostic techniques lack the resolution required to capture the instantaneous flow field and coherent turbulent structures involved in the interaction, needed to probe the underlying mechanism.

Therefore, the first goal of the current study is to uncover the mechanism governing wake-ground interaction through a novel field-scale measurement technique that uses snow to visualize the air flow in the wake of a utility-scale wind turbine. The second objective is to apply this new understanding to the resolution of the discrepancies between previous field-scale experimental studies. Finally, the third aim is to provide a tool for developers to predict the potential impact of wind farms on their surroundings throughout the Continental US.

9.2 Methods

9.2.1 Experimental conditions

The experiment took place between 23:00 CST on March 5th, 2018 and 01:00 CST on March 6th, 2018. The atmospheric and incoming wind conditions during this period were recorded using the met tower and SCADA system. The temperature at hub height stayed relatively constant between -3.1°C and -2.8°C. The bottom of the wake was 0.8°C warmer than the top. The Bulk Richardson Number, calculated using the temperature sensors, relative humidity sensors, and cup and vane anemometers at the 126 m and 7 m elevations of the met tower, is defined as $R_B = \frac{g\Delta\overline{\theta_v}\Delta z}{\overline{\theta_v}\left[(\Delta\overline{U})^2+(\Delta\overline{V})^2\right]}$, where g is gravitational acceleration, θ_v is the virtual potential temperature, z is the elevation, U is the northerly wind component, and V is the westerly wind component [46]. During the experiment, $R_B = 0.12$, indicating an approximately neutral atmospheric boundary layer where turbulence is generated mechanically rather than as a result of thermal gradients. The wind speed varied slightly over the course of the experiment, with instantaneous values between 7 m/s and 11 m/s at the hub, allowing the characterization of the wake under turbine operational regions 2-3. The wind direction was primarily easterly, varying between 73° and 103° clockwise from north. Due to the wind direction, the met tower was not influenced by the wake of the turbine during this time period.

9.2.2 Experimental setup

The flow visualization setup is composed of a light sheet and a camera. The light sheet is formed using a curved mirror to expand the beam from a collimated searchlight with a 300 mm beam diameter. The local wind direction was used to align the light sheet parallel to the wind with an angle of 90.4° clockwise from north, 47 m ($0.5D$) downstream of the turbine and offset 19 m ($0.2D$) from the plane of the tower in the spanwise direction (figure 9.1a). As the wind direction changed throughout the experiment, the degree of misalignment between the light sheet and the rotor changed within the range of -17.3° to 12.0°, with an average of 0.8°. A Sony A7RII camera with a 50 mm f/1.2 lens was used to capture video data at a frame rate of 30 Hz and size of 1080 pixels × 1920 pixels. The camera was placed 120 m away from the light sheet and tilted up 12.4° with respect to the ground. The setup resulted in a field of view

that intersected the ground with dimensions of 87 m $\times$ 49 m (streamwise $\times$ vertical), capturing the interaction between the vortices shed from the blade tips and the ground surface.

9.2.3 Interaction characterization

When these bottom blade tip vortices are produced consistently, they appear as a regularly spaced row of approximately circular dark regions in the images, or voids, where the snow is expelled from the region due to the strong rotation of the air (figure 9.1*b*). However, several periods were observed where strong interaction occurred between the bottom tip vortices and the ground surface, identified by the emergence of a significant amount of chaotic voids above the ground but below the elevation of blade tip vortices (figure 9.1*c*). These voids are caused by the preferential concentration of particles in regions of high strain and the expulsion of particles from regions of high vorticity [204], indicating the presence large velocity gradients which lead to enhanced momentum flux and mixing. To understand the frequency of occurrence and the causes of these periods of strong interaction, they were identified throughout the dataset, first using manual detection. When coherent structures were observed between the bottom blade tip vortices and the ground, the corresponding time period was labelled as "strong interaction". When no structures were observed, it was labelled as "no interaction".

To make the process more robust and objective, an automatic detection method was developed. First, the images were enhanced using moving average background division with a 1000 frame window, adaptive histogram equalization, and wavelet-based denoising. Next, the region of the images below the bottom blade tip vortices was smoothed using a 9-pixel Gaussian filter and the pixel intensity gradient was calculated. The mean of the gradient over this region was used to determine the interaction strength, as many strong voids are observed during periods of strong interaction, yielding a large intensity gradient. This metric was found to accurately identify the same periods of strong interaction identified manually, showing it is an effective method for automatic interaction detection (figure 9.1*d*). All image processing was conducted in MATLAB.

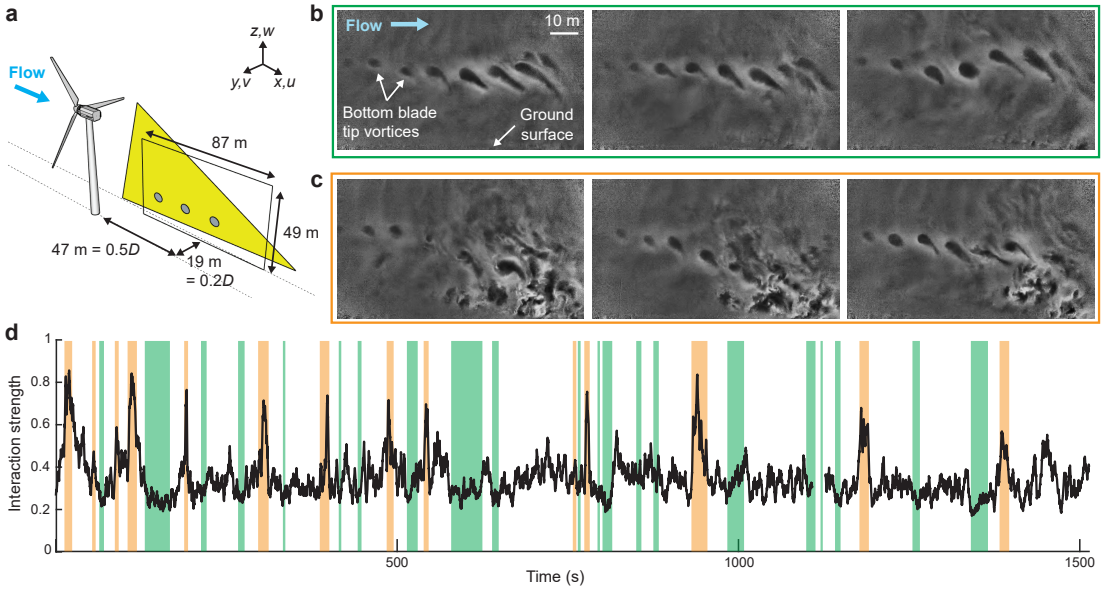

Figure 9.1: Characterization of wake-ground interaction. (a) Schematic showing the setup of the experiment, with the yellow triangle indicating the light sheet and the black rectangle showing the field of view. The origin of the coordinate system is at the base of the turbine support tower. (b) Sample frames from the video showing periods of consistent bottom blade tip vortex appearance, without visible interaction between the wake and the ground surface. (c) Sample video frames, identified manually, showing strong interaction between the wake and the surface. (d) Automatically characterized interaction strength (black line) compared with manually identified strong and weak interaction periods (orange and green bars, respectively). The orange bars coincide with peaks in the interaction strength, showing the robustness of the automatic characterization method.

9.2.4 Vector calculation

To quantify the velocity field, the image distortion induced by the tilt angle of the camera was first corrected following the method described in Toloui et al. [4]. Additionally, the motion of clouds was visible in the background of the video. This was removed by applying a high-pass filter with a cutoff frequency of 0.5 Hz to the video, based on a peak in the video frequency spectrum below the blade pass frequency of the turbine, confirmed to be caused by the cloud motion using manual tracking of the clouds in the video. The velocity vectors were calculated using the adaptive multi-pass cross-correlation algorithm from LaVision Davis 8 with an initial interrogation window of 64 $\times$ 64 pixels

and second pass with interrogation windows of 48 × 48 pixels with 75% overlap. Note that the video did not have sufficient resolution to resolve the individual snow particles in the images, so the snow patterns associated with coherent flow structures provided the signal for the cross-correlation, a concept validated in Dasari et al. [5]. The cross-correlation was applied with a 5-frame skip to ensure sufficient displacement of the structures, resulting in a temporal resolution of 6 Hz. A Hampel filter was applied to the final vector field to remove outliers.

9.3 Results

9.3.1 Two turbine operational pathways to strong interaction

The interaction strength metric shows that the periods of strong interaction occurred intermittently throughout the duration of the dataset (figure 9.1*d*), begging the question of the cause of such drastic changes in wake behavior. To investigate this question, the interaction strength was compared to a broad range of turbine operational and atmospheric parameters. The coincidence of peaks in interaction strength with peaks in three other parameters was observed: the pitch of the turbine blades (figure 9.2*a*), the change in the tip speed ratio (ratio of the speed of the blade tips to the speed of the wind, figure 9.2*b*), and the power output of the turbine (figure 9.2*c*). However, the overall correlation with each parameter was not very strong, suggesting the periods of strong interaction are caused by a combination of multiple factors. To tease out these relationships, a decision tree was used. Periods of strong interaction were defined as periods with the interaction strength above one standard deviation away from the mean, totaling 7 min of the 55 min of recorded data. Sixteen turbine operational and atmospheric parameters were used to train the decision tree to identify periods of strong interaction. Remarkably, the decision tree identified the same three significant parameters manually observed to have some relationship with the interaction strength (figure 9.2*d*). The decision tree was able to predict the occurrence of strong interactions with 89% accuracy. The events were slightly undercounted, suggesting that there are some periods of strong interaction that occur under conditions not accounted for by the decision tree. However, under the specific operational conditions predicted by decision tree, strong interaction is highly likely to occur. Note that the parameters leading to

strong interaction cannot be manually adjusted to induce or mitigate strong interaction with the ground surface, as they are direct responses to atmospheric conditions. They can, however, be used as indicators to predict the occurrence of these periods with reasonable confidence using information already recorded by the turbine controller.

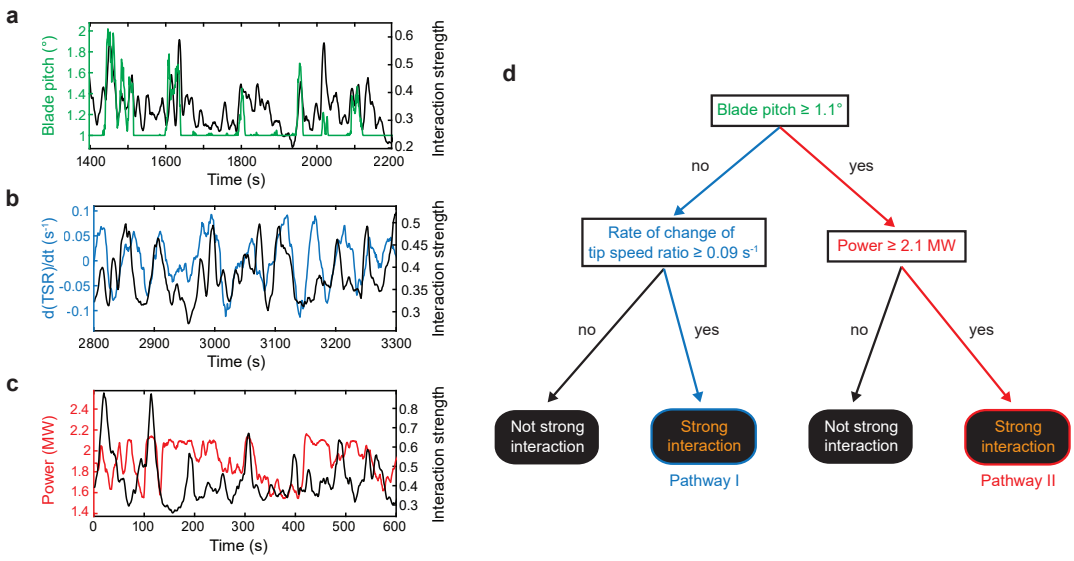

Figure 9.2: Relationship between wake-ground interaction and turbine operational parameters, including (a) blade pitch, (b) change in tip speed ratio over time, and (c) turbine power production. (d) Decision tree showing periods of strong interaction can be predicted by the same three parameters identified manually. The two different pathways to strong interaction are shown in blue and red.

More significantly, the decision tree revealed the existence of two pathways to achieve strong interaction with the ground. The pathway at any given moment is determined by the blade pitch, an indicator of the region of turbine operation (figure 9.2d). When the blade pitch $< 1.1°$, the turbine is operating in region 2 where the atmospheric wind speed is below the rated wind speed and the turbine controller attempts to maximize power production. In this operational region, strong wake-ground interaction occurs when the rate of change of the tip speed ratio ≥ 0.09 s^{-1}. The tip speed ratio, which is constantly changing in response to the perpetual changes in atmospheric wind speed, determines the spacing between the blade tip vortices. When it increases quickly, the blade tip vortices are pushed closer together, causing them to interact and "leapfrog"

over each other. This interaction induces a larger-scale rotation in the flow, pushing the tip vortices closer to the surface and facilitating wake-ground interaction (figure 9.3).

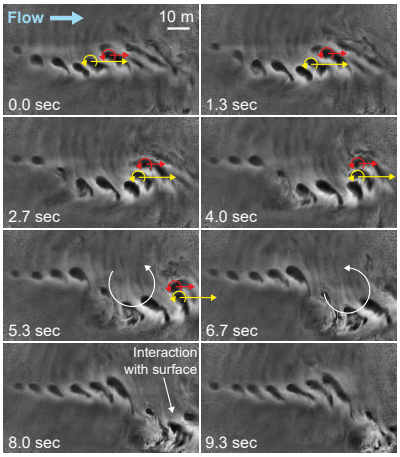

Figure 9.3: Sample image sequence of pathway I to wake-ground interaction, induced by blade tip vortex leapfrogging. One vortex (indicated by a red arrow) moves slower than a vortex behind it (indicated by a yellow arrow), until the rear vortex catches up and the two interaction. The interaction causes a larger-scale rotation (white circular arrow), which pushes the tip vortices closer to the ground, facilitating interaction between the wake and the surface.

The second pathway occurs when the blade pitch $\geq 1.1°$ and the turbine is operating above the rated wind speed, in region 3 (figure 9.2). In this region, the blade pitch varies to regulate the loading on the turbine structure. This pathway is characterized by power production ≥ 2.1 MW. Two tip vortex features that are characteristic of higher power production are observed in this pathway: wider spread in trajectory angle (figure 9.4a) and larger size (figure 9.4b) compared to the first pathway. When more energy is extracted from the wind, the velocity deficit in the wake increases, causing the wake expansion to increase to conserve mass, and pushing the tip vortices closer to the ground. Additionally, the size of snow voids associated with tip vortices is correlated with their circulation strength, which increases with turbine power production [17]. Though these distinctions between the pathways may not be very striking in figures 9.4(a) and (b) due to the dynamic and multi-variate field conditions, a two-sample Kolmogorov-Smirnov test confirms the statistical significance of the differences ($p < 0.001$ for both tip vortex trajectory and size). The velocity and vorticity in the wake confirm these findings, as

strong downward flow (figure 9.4c) and enhanced vorticity (figure 9.4d) are observed around the bottom tip elevation during periods of strong wake-ground interaction in region 3, indicating increased wake expansion and tip vortex strength, respectively.

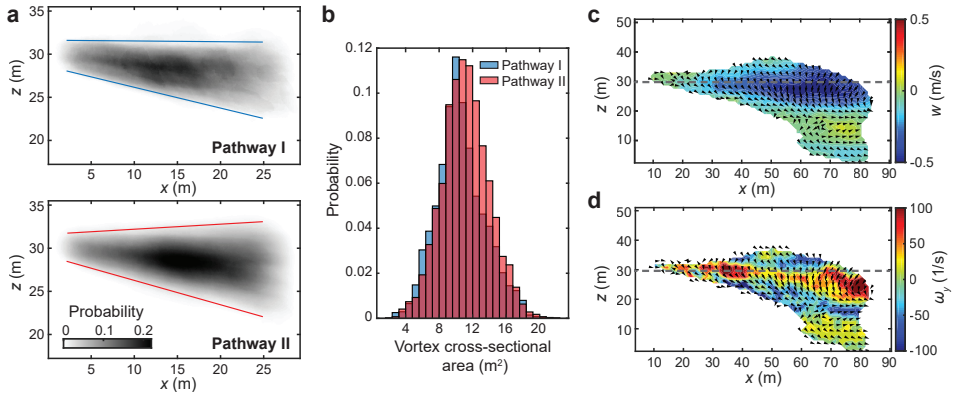

Figure 9.4: Pathway II to wake-ground interaction, caused by (a) increased spread in bottom tip vortex trajectory angle (shading indicates the probability of finding a tip vortex in each location) and (b) increased bottom tip vortex size (defined as the area of the vortex cross-section in the light sheet) compared with pathway I. The tip vortices were extracted for analysis using the image processing method described in [3] and the images were calibrated using the method described in [4] and [5]. Only tip vortices within $0.3D$ of the turbine were included to preclude distortion caused by interaction with the ground or each other. (c) Average wake vertical velocity (w) field conditionally sampled for periods of strong interaction in region 3, subtracted from ensemble averaged region 3 vertical velocity field. Strong downward flow is observed around the bottom blade tip elevation, indicated by a gray dashed line, revealing increased wake expansion during periods of strong interaction in region 3. (d) Average wake spanwise vorticity (ω_y) field conditionally sampled for periods of strong interaction in region 3, subtracted from ensemble averaged region 3 vorticity field. Enhanced vorticity is observed around the bottom blade tip elevation (gray dashed line).

9.3.2 Impact of wake-ground interaction on surface momentum flux

The abovementioned wake-ground interaction can lead to strong variation of surface momentum flux during the operation of a utility-scale turbine. The vertical profile of the mean momentum flux in the wake compared with that outside the wake is consistent with laboratory scale studies [75, 195], showing a strong downward flux just below the bottom tip height and a strong upward flux just above (figure 9.5a). On average, no

significant increase in downward momentum flux near the surface is observed compared to measurements outside the wake. However, when the average momentum flux is calculated over periods of strong interaction only, a significant increase in downward flux is observed near the surface, along with a reduction of flux magnitude just below the bottom blade tip elevation (27 m). The reduction near 27 m is caused by the disturbance of the bottom blade tip vortex location due to either leapfrogging (pathway I) or increased wake expansion (pathway II), and the flattening of the momentum gradient due to enhanced mixing. At an elevation of 10 m, the standard for near-surface atmospheric measurements, the average flux during strong interactions is almost an order of magnitude stronger than that outside of the wake (-2.1×10^{-3} vs. -0.4×10^{-3}, nondimensionalized by U_{hub}^2, where U_{hub} is the mean incoming wind speed at hub height). Though these values are small, they are comparable to normalized surface momentum flux values reported in previous wind tunnel and field studies [75, 195, 197], and they indicate a $> 400\%$ relative increase in flux during periods of strong interaction. Additionally, their difference is outside the bounds of the measurement uncertainty, estimated to be 7×10^{-4} based on uncertainty analysis of the snow-powered flow quantification technique conducted by Dasari et al. [5]. More significantly, there are some periods of strong interaction where the flux is another order of magnitude stronger (figure 9.5*b*), highlighting the intermittency of the wake effects on surface fluxes. Separating the flux during periods of strong interaction into the two pathways shows that pathway II causes a stronger average flux increase than pathway I by a factor of 1.8 (figure 9.5*c*). Further, pathway II is responsible for the periods of strongest flux. These results show that the extent of wind turbine wake interaction with the ground surface is highly dependent on turbine operating conditions.

Additional data taken from the met tower located 170 m ($1.8D$) south of the turbine supplements the flow visualization findings. When the wind blows from the north, the met tower is located within the wake of the turbine and the 20 Hz 3-component wind data from the sonic anemometer at the 10 m elevation is used to calculate the vertical surface momentum flux. From nearly nine years of stored data, 615 20-min periods are selected where the wind is coming from the north (between -11° and 12° clockwise from north) and the turbine is operating in region ≥ 2. The flux is then conditionally sampled

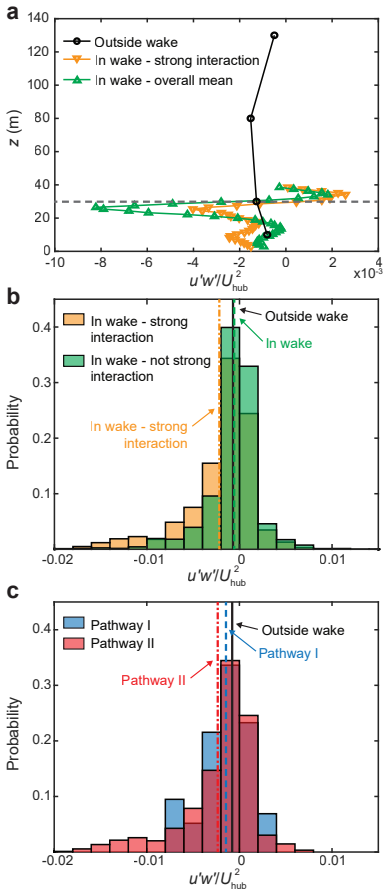

Figure 9.5: The effect of wake-ground interaction on surface momentum flux. (a) Profile of the average momentum flux outside of the wake, inside of the wake, and inside the wake only during periods of strong interaction, normalized by the incoming wind speed. The horizontal dashed line indicates the bottom blade tip elevation (30 m). (b) Histogram of the normalized momentum flux in the wake at the 10 m elevation for periods of strong interaction and periods not identified as strong interaction. The average of each case, including the momentum flux outside the wake, is indicated by a vertical line. (c) Histogram of the normalized momentum flux in the wake at the 10 m elevation for each strong interaction pathway. The average of each case, including the momentum flux outside the wake, is indicated by a vertical line.

based on the two enhanced flux pathways uncovered from the decision tree and normalized by U_{hub}^2 using simultaneously recorded SCADA data. Pathway II enhances flux at the met tower by a factor of 1.8, the same factor calculated from the flow visualization data, while pathway I does not significantly change the surface flux $1.8D$ downstream (table 9.1). The different impacts of the two pathways can likely be explained by the different mechanisms for each. Pathway I occurs due to tip vortex leapfrogging in the extreme near wake ($< 1D$), as observed in the flow visualization data. Therefore, by the time the wake has travelled further downstream, this effect has dissipated. In the pathway II case, however, the enhanced mixing is caused by the strength of the tip vortices and the wake rather than an isolated event, allowing the effect to persist as the wake travels downstream.

Table 9.1: Mean momentum flux for each pathway under different atmospheric stabilities using 205 hours of data from the met tower located $1.8D$ downstream of the turbine.

$\overline{u'w'}/U_{\text{hub}}^2 \times 10^{-3}$	Not strong interaction	Strong interaction —Pathway I	Strong interaction —Pathway II
All atmospheric stabilities	-1.1	-1.1	-2.0
Stable ($R_B \geq 0.25$)	-0.8	-0.9	-2.5
Neutral ($0 \leq R_B < 0.25$)	-1.4	-1.3	-1.9
Unstable ($R_B < 0$)	-1.2	-1.3	-1.5

Furthermore, the effect of atmospheric stability on wake-induced momentum flux enhancement is investigated using the more than 200 hours of met tower wake data. The Bulk Richardson Number (R_B), the dimensionless number that quantifies the effect of buoyancy due to temperature gradients versus shear-generated turbulence defined in section 9.2.1, is used to categorize each 20-min period as stable, neutral, or unstable. The greater the value of R_B, the more stable the atmospheric boundary layer, indicating less turbulent mixing is occurring. This categorization reveals that the pathway II surface momentum flux enhancement is strongest when the boundary layer is stable and weakest when it is unstable (table 9.1). These findings are consistent with the observations of multiple previous studies that show that the wind turbine wake and the coherent structures within it are stronger and persist longer with increasing atmospheric stability [75, 195, 97, 98, 205], providing further support for a stronger wake and tip

vortex as the mechanism behind pathway II surface flux enhancement. Note that, even though the met tower is in the wake of the wind turbine, R_B uses mean values of wind speed and temperature from the top and bottom edges of the wake, which will not be significantly impacted by the wake, as evidenced by the results shown in Figure 5b and as observed in [75]. Even with a 20% uncertainty in R_B caused by the slight velocity reduction at these points, the resulting uncertainty in the normalized momentum flux values listed in table 9.1 is 1×10^{-4}, which does not significantly affect the observed trends.

9.3.3 Reconciling discrepancies in previous studies

The dependence of wake-surface interaction on operating conditions, a factor that was not considered in previous studies, facilitates the proposal of an explanation to reconcile the conflicting temperature change results from field studies in the literature. The connection between momentum flux and temperature is supported by multiple previous studies (e.g., [203, 206, 207]) which demonstrate that changes in momentum flux affect near-surface thermal stratification, which in turn affects turbulent heat fluxes and surface temperatures. Furthermore, from a fundamental heat transfer perspective, turbulent mixing is the main mechanism for heat transport in a turbulent boundary layer [208]. Based on this relationship, the momentum enhancement is estimated qualitatively to provide insight into the mechanism behind temperature changes observed in previous studies. Five-min resolution simulated wind speed data for the Continental United States, obtained from the Wind Integration National Dataset Toolkit [209], is used to perform this analysis. Note that this data is not used to quantify the momentum flux enhancement occurring during any of the referenced studies. Rather, it provides an additional explanation for the qualitative temperature changes observed that could not be fully understood previously.

Baidya Roy and Traiteur [198] observed cooling during the day at a California wind farm in the summer of 1989, with the period with the largest temperature change occurring in the afternoon. Based on the simulated wind speed data, wind speeds are highest in the afternoon during this time of year, suggesting flux enhancement through pathway II was occurring. This enhanced flux likely caused cooling due to the presence of aquifer recharging ponds located between the wind farm rows [197]. Zhou et al. [199]

investigated the effect of a Texas wind farm on temperature changes in the winter and summer, finding significant temperature increases at night, particularly in the summer. This observation could be caused by enhanced mixing bringing warmer air down to the surface, which is typically cooler at night. The simulated historical data shows that the mean wind speed at the site of the investigation is higher at night, especially during the summer. However, the rated wind speed of the turbines in the wind farm is 12 m/s, while the maximum mean wind speed is 8.5 m/s which may not be high enough to push the turbines into region 3 for significant amount of time. On the other hand, the standard deviation of wind speed is higher in the evening, particularly in the summer. The standard deviation, calculated for each hour using the five-min resolution data, represents the level of wind speed fluctuations that cause changes in tip speed ratio. The occurrence of high wind speed fluctuations in the evening indicates that pathway I flux enhancement could be responsible for the observed temperature increase. Smith et al. [196] reported an increase in surface temperature at night in a wind farm in the United States Midwest. The largest temperature changes occurred during the periods of highest wind speed, suggesting flux enhancement through pathway II. Rajewski et al. [191] compared surface warming to boundary layer stability in an Iowa wind farm. They observed warming when the boundary layer was slightly stable, which typically occurs in the evening and morning [210]. The simulated historical data shows the highest standard deviation of wind speed also occurs during these periods, indicating the temperature changes were caused by pathway I flux enhancement. Additionally, the rated wind speed for the turbines investigated was 14 m/s, significantly higher than the maximum mean wind speed of 7.2 m/s, so pathway II is less likely to be responsible for the observed changes. Finally, Archer et al. [197] investigated the impact of a single turbine in Delaware on surface fluxes. They did not observe any flux increases in the turbine wake, potentially due to the fact that the periods investigated had very low wind speeds ($\sim$ 5 m/s at hub height), during which the turbine would be operating below region 2. In the current experiments, no significant interaction between the wake and the surface was observed when the wind speed was so low, as the tip vortices and wake expansion are not strong enough for the wake to reach the ground. Though many other factors may influence the previously reported findings, this analysis demonstrates that turbine operational conditions cannot be neglected when evaluating the impact of

wind turbines on their surroundings.

9.3.4 Map of potential impacts

The impact of wind turbines on surface fluxes has significant implications for wind farm siting decisions. To provide guidance for these decisions, maps of the potential impact of wind turbines on surface momentum flux enhancement in the Continental United States are provided based on the two pathways identified above (figure 9.6). The surface momentum flux impact index, I_{SMF}, is calculated using the mean and standard deviation for each hour of wind speed data from the Wind Integration National Dataset Toolkit [209]. Because the data has five-min resolution, 12 data points are used for each calculation. Pathway I for enhanced flux is characterized by changes in tip speed ratio, which is in turn determined by changes in wind speed, while pathway II is characterized by high mean wind speeds that push the turbine into region 3 operation. Therefore, the average standard deviation and mean are used to calculate the index for pathways I and II, respectively. The index for pathway I is

$$I_{\mathrm{SMF,I}} = \left(\mathrm{std}(u) - \min\left(\mathrm{std}(u)\right)\right) / \max\left(\mathrm{std}(u) - \min\left(\mathrm{std}(u)\right)\right), \tag{9.1}$$

where u is the wind speed. For pathway II, the index is defined as

$$I_{\mathrm{SMF,II}} = \left(\mathrm{mean}(u) - \min\left(\mathrm{mean}(u)\right)\right) / \max\left(\mathrm{mean}(u) - \min\left(\mathrm{mean}(u)\right)\right). \tag{9.2}$$

The overall surface momentum flux impact index combines the effects of both pathways:

$$I_{\mathrm{SMF}} = 0.6 I_{\mathrm{SMF,I}} + I_{\mathrm{SMF,II}}. \tag{9.3}$$

The index for pathway I is weighted with 0.6 because the flux enhancement due to pathway I is 0.6 times that of pathway II. Note that these indices are not used to directly calculate the momentum flux. Rather, they are used to predict the likelihood of a wind turbine or farm operating under conditions that would cause enhanced interaction with the surface through either of the two pathways. Overall, the potential mixing enhancement is strongest in the Rocky Mountain and Great Plain regions of the US (figure 9.6*a*). Pathway I contributes most in the Rocky Mountain region where the wind speed exhibits significant fluctuations (figure 9.6*b*), while pathway II contributes

most in the Great Plains where the wind resource is largest (figure 9.6c). These findings can be incorporated into wind farm siting models to determine the impact of potential wind farms on their surroundings.

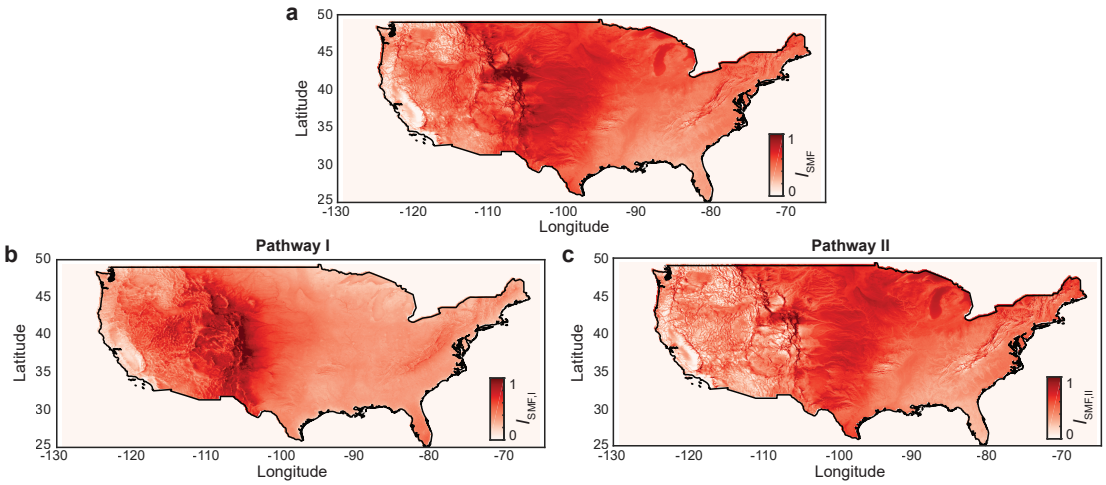

Figure 9.6: Impact of potential wind farms in the Continental United States. (a) Impact of potential wind farms on surface momentum flux enhancement, considering both pathways. (b) Impact of potential wind farms on mixing, only considering pathway I. (c) Impact of potential wind farms on mixing, only considering pathway II.

9.4 Conclusion and discussion

The current study employs a novel field-scale flow visualization technique using natural snowfall to probe the mechanisms governing wind turbine wake interactions with the ground surface. This technique reveals that periods of strong wake-ground interaction are highly intermittent. Furthermore, these periods occur as a result of changes in turbine operation. Two pathways to strong interaction are defined: Pathway I occurs when the turbine is operating in region 2 (below the rated wind speed) and the tip speed ratio changes rapidly, leading to leapfrogging. Pathway II occurs when the turbine operates in region 3 (above the rated wind speed) and generates more power, causing a stronger wake and larger blade tip vortices. Flow visualization data is supplemented with more than 200 hours of met tower data from 1.8D downstream that supports the existence of the two pathways to strong interaction and shows that pathway II is

significantly stronger than pathway I once the wake has propagated downstream. The met tower data provides additional insights into the effects of atmospheric stability on periods of wake-ground interaction, showing that surface momentum flux enhancement is strongest when the boundary layer is stable. The dependence of enhanced mixing on turbine operation is then used to propose an explanation for the discrepancies between previous field studies on wake-ground interaction. Finally, maps of the Continental US showing the potential impact of wind farms on surface momentum flux enhancement are presented.

The impact of wind turbines on surface fluxes has significant implications for wind farm siting, particularly for the agricultural industry. The enhanced mixing caused by wind turbines can affect the evapotranspiration process in plants, which enables the diffusion of gasses necessary for photosynthesis [211]. This consideration is especially important in the Continental United States, where much of richest wind resources coincide with regions of high agricultural productivity (figure 9.7). Previous studies have also shown that wind farms can cause warming of lakes downwind due to increased evaporation [193] and offshore wind farms can affect the properties of the surrounding ocean waves [194]. To minimize any negative impacts of a potential wind farm, the findings of the current study should be integrated into models used for siting decisions. As a potential benefit of the enhanced mixing observed here, wind farms could be coupled with solar farms, as surface cooling is a key issue limiting solar panel efficiency [212]. The results of the current study have global implications; multiple studies have shown that large-scale wind farms can affect global climate, but the magnitude of the impact is not consistent between them [201, 202, 207, 213, 214]. The dependence of wake-ground mixing on incoming flow and turbine operational conditions can be incorporated into the global climate models used to assess wind farm impacts in order to achieve more reliable results.

Though the current study is largely limited to the near wake of a single utility-scale turbine, the physical insights gained are broadly applicable. Enhanced mixing between the wake and the ground happens under turbine operating conditions that are likely to occur regardless of the specific turbine design and turbine layout in a farm. Furthermore, the effects of the near wake are likely significantly stronger than those of the far wake due to the presence of the strong coherent structures shed from the blade tips. In the near

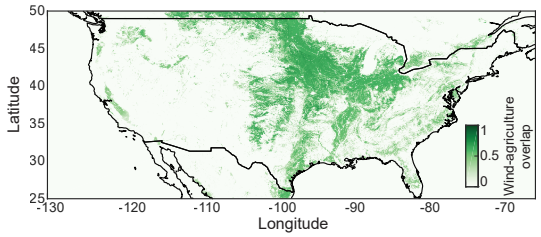

Figure 9.7: A map of the overlap between wind resources and agriculture in the Continental United States, combining the wind speed at 100 m elevation from the Global Wind Atlas [6] and the percentage of each square kilometer used for cropland from the Global Land Cover SHARE database from the Food and Agriculture Organization of the United Nations [7].

wake, the blade tip vortices generate a concentrated region of increased vorticity and turbulence intensity, which weakens significantly after the tip vortices begin to break down [63, 24]. Beyond the point of tip vortex breakdown, random mixing leads to re-entrainment of momentum and re-energizing of the wake. However, according to the Biot-Savart Law, coherent vortices induce a velocity in the fluid at a distance r away, while random turbulent fluctuations do not have this property. The strong coherent vortices (i.e., blade tip vortices) that have the ability to induce a velocity at the ground surface only exist in the near wake until $\sim 2D$, so the interaction between the wake and the ground is likely to be strongest within this region.

When extending these results to a whole wind farm, the result will likely be spatial and temporal heterogeneity. The near wake of each individual turbine will experience periods of enhanced surface momentum flux, while the far wakes of individual turbines and the wake of the wind farm as a whole will not see the same effects. Indeed, this expectation is supported by the results of Smith et al. [196] who observed strong wake effects in measurements taken $2.4D$ downstream of an individual turbine, but no clear wake signal in measurements taken $26D$ downstream of the entire wind farm. The significance of the near wake brings to light the shortcomings of many wind farm parameterizations in climate models. Wind farms are often modelled as roughness elements [201, 207, 213] or momentum sinks and turbulent kinetic energy (TKE) sources [200, 202, 203, 214], neither of which captures the aforementioned heterogeneity. The

actual wind turbine wake, particularly the near wake, is more complicated than a uniform TKE increase and momentum deficit, with coherent structures and a complex wake profile [49]. Even higher-fidelity models such as large eddy simulations often do not account for the stochasticity of the atmosphere or the corresponding changes in turbine operation (e.g., pitch, hub speed) that are responsible for the intermittency of the flux enhancement observed in the current study. The spatial and temporal averages of the wind farm boundary layer mask the local extremes that could significantly affect the environment around the wind farm.

However, the reader should use caution when extending the findings of the current study, as the physical understanding of the results was derived from intermittent occurrences during an experiment conducted under limited atmospheric conditions at a single site. Under different atmospheric stabilities or surface roughnesses, the tip vortices may interact differently with the ambient turbulence, leading to additional mechanisms for wake-ground interaction. Further investigation into the effects of wind turbines on heat and moisture fluxes is required before the full impact of a wind farm can be determined. Therefore, when deciding whether to build a wind farm in a specific location, the framework provided here can be used with more accurate local wind data to improve the reliability of the predicted effect on the surrounding environment.

Chapter 10

Conclusion and Discussion

10.1 Summary

Utility-scale wind turbines experience constantly changing atmospheric conditions. As dynamic structures, they are actively interacting with the inflow and modulating their wake behavior. To evaluate these complex flow-structure interactions in the field, super-large-scale flow imaging using natural snowfall is employed at the Eolos field site, home of a 2.5 MW wind turbine. This technique provides high-resolution flow fields, enabling quantification of velocity, turbulence, and coherent structure characteristics in both the inflow and wake of the turbine.

This technique first provides an opportunity to reveal the complex flow coming towards the turbine. Chapter 3 investigates the impact of atmospheric coherent structures on the turbine structure, power generation, and wake. Vortical coherent structures in the inflow to the turbine are first identified and characterized by quantifying their size and packet length. Long coherent structure packets are shown to increase fluctuating stresses on the turbine support tower. Large inflow vortices interact with the turbine blades, leading to deviations from the expected power generation. The sign of these deviations is related to the rotation direction of the vortices, with rotation in the same direction as the circulation on the blades leading to periods of power surplus, and opposite rotation causing power deficit. Periods of power deficit coincide with wake contraction events. These findings highlight the importance of considering coherent structure properties when making turbine design and siting decisions.

The impact of the nacelle and tower on the coherent structures in the near-wake is evaluated in chapter 4. The nacelle wake meandering frequency is found to scale with the nacelle dimension rather than the rotor dimension, corresponding to the vortex shedding frequency of an Ahmed body. Persistent nacelle wake deflection is observed and shown to be connected with the turbine yaw error. Strong interaction between the tower- and blade-generated structures, quantified by the co-presence of two dominant frequencies, demonstrates the influence of the tower on blade tip vortex breakdown. This study highlights the influence of the tower and nacelle on the behavior of the near-wake, informing model development and elucidating the mechanisms that influence wake evolution.

The next four chapters focus on the large-scale motion of the wake in response to changes in incoming flow and turbine operational conditions, termed dynamic wake modulation. Chapter 5 introduces this phenomenon, quantifying the wake expansion response to changes in blade pitch and tip speed ratio and the wake deflection response to changes in rotor alignment with the wind direction. These measurements reveal the significant influence of dynamic wake modulation, which causes an increase in flux across the near wake boundary of 11% on average, on wake recovery, providing insights into necessary modifications to traditional wake and farm models. Further, the study uncovers the direct connection between dynamic wake modulation and operational parameters readily available to the turbine controller, which pave the way for more precise wake prediction and control algorithms under field conditions for wind farm optimization.

In chapter 6, the mechanisms governing dynamic wake modulation are examined in more detail under controlled conditions using large eddy simulations. First the results of the simulations are compared to the field-scale experiment, showing agreement between the trends observed using both methods. The timescales of the wake response to changes in blade pitch, wind direction, and yaw angle are then quantified to inform the design of advanced dynamic wake control strategies. Next, the propagation of the near-wake expansion and deflection response and its impact on the energy flux into the wake at seven rotor diameters downstream are evaluated (chapter 7). Dynamic wake modulation is found to enhance mixing in the far wake under both uniform and turbulent flow conditions.

Next, a method for improving wind farm power prediction by incorporating dynamic

wake modulation is proposed in chapter 8. FAST.Farm, an open-source wind farm modeling software is used as the basis for modifications, including additional eddy-viscosity terms to account for enhanced mixing across the wake boundary. These modifications are expected to reduce power generation prediction uncertainty that is currently a primary source of risk in the wind energy industry. In addition, the revised software can be used to improve wind farm design and layout optimization.

Finally, the interaction between the wind turbine near-wake and the ground surface is characterized (chapter 9). Intermittent periods of strong interaction between the wake and the ground surface are observed and the momentum flux during these periods is quantified. Significantly, two turbine operational-dependent pathways that lead to these periods of increased wake-ground interaction are identified. The first is caused by changes in tip speed ratio that lead to blade tip vortex leapfrogging, and the second results from increased power generation and the corresponding increase in tip vortex strength and wake expansion. Data from the meteorological tower at the Eolos site provides further insights into the strength and persistence of the enhanced flux for each pathway under different atmospheric conditions. Through the discovery of these pathways, discrepancies can be resolved between previous conflicting studies on the impact of wind turbines on surface fluxes. Furthermore, the results are used to generate a map of the potential impact of wind farms on surface momentum flux throughout the Continental United States, providing a valuable resource for wind farm siting decisions.

10.2 Implications

This work has provided several novel insights into utility-scale wind turbine wake behaviors. Understanding of these behaviors can be incorporated into wind farm simulations and experiments at a range of fidelities. Currently, many simplifying assumptions are made that compromise the accuracy of model study finding. For example, the dynamic wake meandering model treats the wake as a passive tracer [114, 115], while the current work has shown that this is not the case. Additionally, laboratory-scale turbine models often do not size the nacelle proportionally to the rotor, leading to inaccurate nacelle wake behavior [82, 83], which impacts wake development downstream [25]. The primary challenge is to incorporate these field-scale behaviors accurately without sacrificing the

primary benefit of the models, such as their simplicity. The findings of the current work provide insights into which simplifications do not compromise the accuracy of the results and which need to be revised. Using these findings, simplifications with improved accuracy can be developed, as in the modified power prediction model presented in chapter 8.

By incorporating the findings of the current research into improved models, wind farm design and siting decisions can be made more effectively. During the wind farm site optimization process, turbine locations are iteratively perturbed to minimize the levelized cost of energy. In each iteration, the wake losses are estimated [184]. With improved wake models, the optimization algorithm can select a wind farm layout that reduces these losses with improved accuracy while minimizing costs. For example, the additional wake mixing contributed by dynamic wake modulation may enable closer turbine spacing, allowing more turbines to fit in a given area and increasing the energy density of the wind farm.

In recent years, advanced control algorithms have attracted substantial interest as methods for improving wind farm efficiency. Rather than each turbine working to maximize its own power generation (greedy control), the entire wind farm can work together to maximize total power generation (coordinated control). The basis of coordinated control is controlling the wakes so they do not interfere with downstream turbines. A wide variety of methods have been proposed to accomplish this goal (see section 6.1 for examples), but they all require detailed understanding of wake behavior. Coordinated control algorithms typically take advantage of turbine control maneuvers that are already used for greedy control (e.g., blade pitch, yaw angle) and therefore occur under normal utility-scale wind turbine operation. Consequently, these coordinated control algorithms cannot be implemented on utility-scale turbines without accounting for the phenomena described in the current work, particularly dynamic wake modulation which dictates the magnitude and timescale of the wake response to turbine operational changes. As the wake behaviors observed in the current work are directly attributed to parameters measured by the standard SCADA system, the wake response to changes in these parameters can be predicted with statistically significant confidence.

10.3 Limitations and future work

There are still many unanswered questions about the wake response to dynamic operation and inflow. First, the propagation of the observed near-wake behaviors downstream has been investigated using simulations, but not field data. This limitation is primarily attributed to the challenge of aligning the flow visualization light sheet with the far wake. Farther from the turbine, wake meandering and deflection make it difficult to predict the position of the wake. Additionally, the wake would be constantly fluctuating in and out of the light sheet. In spite of these challenges, far wake data would be very useful for understanding how near wake behaviors persist, change, and interact as they move downstream.

Additionally, the flow visualization technique could be extended to record multiple wake planes simultaneously. This extension would enable the simultaneous capture of larger inflow and near-wake FOVs to quantify flow modulation as it passes through the rotor in more detail, perpendicular cross-sections of the near wake to facilitate full three-dimensional visualization, and near and far wake planes to directly observe downstream propagation. Similarly, stereo particle image velocimetry [215] with natural snowflakes could be employed to capture the out-of-plane velocity component. These configurations would enable a more thorough characterization of the utility-scale wind turbine wake.

Finally, the current research focused on conducting experiments under typical turbine operating conditions, without modifying the turbine controller. Though effective for understanding how the turbine wake behaves during normal operation, environmental variables could not be isolated from turbine control maneuvers. For example, the turbine blade pitch angles changes when the wind speed changes, so the resulting wake behavior could be a response to either factor. Future studies could experiment with modifying the control to isolate individual variables. Furthermore, advanced control algorithms could be implemented on the Eolos turbine to evaluate their impact on the wake. Individual pitch control, where the pitch of each turbine blade is modified separately to regulate loads, has already been tested on the Eolos turbine, though its effect on the wake was not analyzed [216]. Quantifying such an effect is an excellent opportunity for future super-large-scale flow visualization studies.

References

[1] Á. Jiménez, A. Crespo, and E. Migoya. Application of a LES technique to characterize the wake deflection of a wind turbine in yaw. *Wind Energy*, 13:559–572, 2010.

[2] G. Cortina, M. Calaf, and R. B. Cal. Distribution of mean kinetic energy around an isolated wind turbine and a characteristic wind turbine of a very large wind farm. *Physical Review Fluids*, 1(7):074402, 2016.

[3] A. Abraham and J. Hong. Dynamic wake modulation induced by utility-scale wind turbine operation. *Applied Energy*, 257:114003, 2020.

[4] M. Toloui, S. Riley, J. Hong, K. Howard, L. P. Chamorro, M. Guala, and J. Tucker. Measurement of atmospheric boundary layer based on super-large-scale particle image velocimetry using natural snowfall. *Experiments in Fluids*, 55:1737, 2014.

[5] T. Dasari, Y. Wu, Y. Liu, and J. Hong. Near-wake behaviour of a utility-scale wind turbine. *Journal of Fluid Mechanics*, 859:204–246, 2019.

[6] Global Wind Atlas. Technical report, Technical University of Denmark, 2019.

[7] Global land cover share database. Technical report, Food and Agriculture Organization of the United Nations, 2013.

[8] P. Veers and et al. Grand challenges in the science of wind energy. *Science*, 366:eaau2027, 2019.

[9] J. C. Y. Lee and M. J. Fields. An overview of wind-energy-production prediction bias, losses, and uncertainties. *Wind Energy Science*, 6(2):311–365, 2021.

[10] S. Lee, M. J. Churchfield, P. J. Moriarty, J. Jonkman, and J. Michalakes. A numerical study of atmospheric and wake turbulence impacts on wind turbine fatigue loadings. *Journal of Solar Energy Engineering, Transactions of the ASME*, 135(3):1–10, 2013.

[11] S. H. Kim, H. K. Shin, Y. C. Joo, and K. H. Kim. A study of the wake effects on the wind characteristics and fatigue loads for the turbines in a wind farm. *Renewable Energy*, 74:536–543, 2015.

[12] K. Howard and M. Guala. Upwind preview to a horizontal axis wind turbine: a wind tunnel and field-scale study. *Wind Energy*, 19:1371–1389, 2016, 1605.01449.

[13] K. Nilsson, W. Z. Shen, J. N. Sørensen, S.-P. Breton, and S. Ivanell. Validation of the actuator line method using near wake measurements of the MEXICO rotor. *Wind Energy*, 18:499–514, 2015.

[14] M. A. Sprague, S. Ananthan, G. Vijayakumar, and M. Robinson. ExaWind: A multifidelity modeling and simulation environment for wind energy. *Journal of Physics: Conference Series*, 1452:012071, 2020.

[15] G. V. Iungo, Y. T. Wu, and F. Porté-Agel. Field measurements of wind turbine wakes with lidars. *Journal of Atmospheric and Oceanic Technology*, 30(2):274–287, 2013.

[16] G. Wang and X. Zheng. Very large scale motions in the atmospheric surface layer: a field investigation. *Journal of Fluid Mechanics*, 802:464–489, 2016.

[17] J. Hong, M. Toloui, L. P. Chamorro, M. Guala, K. Howard, S. Riley, J. Tucker, and F. Sotiropoulos. Natural snowfall reveals large-scale flow structures in the wake of a 2.5-MW wind turbine. *Nature Communications*, 5:4216, 2014.

[18] X. Yang, J. Hong, M. Barone, and F. Sotiropoulos. Coherent dynamics in the rotor tip shear layer of utility-scale wind turbines. *Journal of Fluid Mechanics*, 804:90–115, 2016.

[19] M. Heisel, T. Dasari, Y. Liu, J. Hong, F. Coletti, and M. Guala. The spatial structure of the logarithmic region in very-high-Reynolds-number rough wall turbulent boundary layers. *Journal of Fluid Mechanics*, 857:704–747, 2018.

[20] A. Nemes, T. Dasari, J. Hong, M. Guala, and F. Coletti. Snowflakes in the atmospheric surface layer: observation of particle-turbulence dynamics. *Journal of Fluid Mechanics*, 814:592–613, 2017.

[21] C. Li, K. Lim, T. Berk, A. Abraham, M. Heisel, M. Guala, F. Coletti, and J. Hong. Settling and clustering of snow particles in atmospheric turbulence. *Journal of Fluid Mechanics*, 912:A49, 2021, 2006.09502.

[22] L. J. Vermeer, J. N. Sørensen, and A. Crespo. Wind turbine wake aerodynamics. *Progress in Aerospace Sciences*, 39:467–510, 2003.

[23] T. Göçmen, P. Van Der Laan, P. E. Réthoré, A. P. Diaz, G. C. Larsen, and S. Ott. Wind turbine wake models developed at the technical university of Denmark: A review. *Renewable and Sustainable Energy Reviews*, 60:752–769, 2016.

[24] L. E. M. Lignarolo, D. Ragni, F. Scarano, C. J. Simão Ferreira, and G. J. W. Van Bussel. Tip-vortex instability and turbulent mixing in wind-turbine wakes. *Journal of Fluid Mechanics*, 781:467–493, 2015.

[25] S. Kang, X. Yang, and F. Sotiropoulos. On the onset of wake meandering for an axial flow turbine in a turbulent open channel flow. *Journal of Fluid Mechanics*, 744:376–403, 2014.

[26] J. Hong and A. Abraham. Snow-powered research on utility-scale wind turbine flows. *Acta Mechanica Sinica*, 36(2):339–355, 2020.

[27] C. E. Willert and M. Gharib. Digital particle image velocimetry. *Experiments in Fluids*, 10(4):181–193, 1991.

[28] R. J. Adrian. Twenty years of particle image velocimetry. *Experiments in Fluids*, 39(2):159–169, 2005.

[29] S. T. Frandsen. Turbulence and turbulence- generated structural loading in wind turbine clusters. Technical Report January, 2007.

[30] J. Park, S. Basu, and L. Manuel. Large-eddy simulation of stable boundary layer turbulence and estimation of associated wind turbine loads. *Wind Energy*, 17:359–384, 2014.

[31] D. Medici and P. H. Alfredsson. Measurements on a wind turbine wake: 3D effects and bluff body vortex shedding. *Wind Energy*, 9(3):219–236, 2006.

[32] Y. Wu and F. Porté-Agel. Atmospheric Turbulence Effects on Wind-Turbine Wakes: An LES Study. *Energies*, 5:5340–5362, 2012.

[33] S. E. Hommema and R. J. Adrian. Packet structure of surface eddies in the atmospheric boundary layer. *Boundary-Layer Meteorology*, 106(1):147–170, 2003.

[34] D. Li and E. Bou-Zeid. Coherent structures and the dissimilarity of turbulent transport of momentum and scalars in the unstable Atmospheric surface layer. *Boundary-Layer Meteorology*, 140(2):243–262, 2011.

[35] S. P. Oncley, O. Hartogensisa, and C. Tong. Whirlwinds and hairpins in the atmospheric surface layer. *Journal of the Atmospheric Sciences*, 73(12):4927–4943, 2016.

[36] K. Träumner, T. Damian, C. Stawiarski, and A. Wieser. Turbulent Structures and Coherence in the Atmospheric Surface Layer. *Boundary-Layer Meteorology*, 154(1):1–25, 2015.

[37] I. Cheliotis, E. Dieudonné, H. Delbarre, A. Sokolov, E. Dmitriev, P. Augustin, and M. Fourmentin. Detecting turbulent structures on single Doppler lidar large datasets: an automated classification method for horizontal scans. *Atmospheric Measurement Techniques*, 13:6579–6592, 2020.

[38] L. Alcayaga, G. C. Larsen, M. Kelly, and J. Mann. Large-scale coherent structures in the atmosphere over a flat terrain. *Journal of Physics: Conference Series*, 1618:062030, 2020.

[39] R. J. Adrian. Hairpin vortex organization in wall turbulence. *Physics of Fluids*, 19:041301, 2007.

[40] N. D. Kelley, B. J. Jonkman, G. N. Scott, J. T. Bialasiewicz, and L. S. Redmond. The Impact of Coherent Turbulence on Wind Turbine Aeroelastic Response and Its Simulation. In *WindPower 2005*, page 22, 2005.

[41] L. P. Chamorro, C. Hill, V. S. Neary, B. Gunawan, R. E. A. Arndt, and F. Sotiropoulos. Effects of energetic coherent motions on the power and wake of an axial-flow turbine. *Physics of Fluids*, 27(5), 2015.

[42] I. Karagali, J. Mann, E. Dellwik, and N. Vasiljević. New European Wind Atlas: The Osterild balconies experiment. *Journal of Physics: Conference Series*, 1037:052029, 2018.

[43] L. P. Chamorro, S. J. Lee, D. Olsen, C. Milliren, J. Marr, R. E. A. Arndt, and F. Sotiropoulos. Turbulence effects on a full-scale 2.5 MW horizontal-axis wind turbine under neutrally stratified conditions. *Wind Energy*, 18:339–349, 2015.

[44] M. Heisel, J. Hong, and M. Guala. The spectral signature of wind turbine wake meandering: A wind tunnel and field-scale study. *Wind Energy*, 21(9):715–731, 2018.

[45] C. Li, A. Abraham, B. Li, and J. Hong. Incoming flow measurements of a utility-scale wind turbine using super-large-scale particle image velocimetry. *Journal of Wind Engineering and Industrial Aerodynamics*, 197:104074, 2020.

[46] R. B. Stull. *An introduction to boundary layer meteorology*. Kluewer Academic Publishers, Dordrecht, 1988.

[47] A. Abraham and J. Hong. Operational-dependent wind turbine wake impact on surface momentum flux. *Renewable and Sustainable Energy Reviews*, 144:111021, 2021.

[48] W. Thielicke and E. J. Stamhuis. PIVlab – Towards User-friendly, Affordable and Accurate Digital Particle Image Velocimetry in MATLAB. *Journal of Open Research Software*, 2, 2014.

[49] A. Abraham, T. Dasari, and J. Hong. Effect of turbine nacelle and tower on the near wake of a utility-scale wind turbine. *Journal of Wind Engineering and Industrial Aerodynamics*, 193:103981, 2019.

[50] J. H. Lee and H. J. Sung. Very-large-scale motions in a turbulent boundary layer. *Journal of Fluid Mechanics*, 673:80–120, 2011.

[51] B. Ganapathisubramani, E. K. Longmire, and I. Marusic. Characteristics of vortex packets in turbulent boundary layers. *Journal of Fluid Mechanics*, 478(478):35–46, 2003.

[52] R. J. Adrian, C. D. Meinhart, and C. D. Tomkins. Vortex organization in the outer region of the turbulent boundary layer. *Journal of Fluid Mechanics*, 422:1–54, 2000.

[53] J. K. Eaton and J. R. Fessler. Preferential concentration of particles by turbulence. *International Journal of Multiphase Flow*, 20:169–209, 1994.

[54] S. K. Robinson. A Review of Vortex Structures and Associated Coherent Motions in Turbulent Boundary Layers. In A. Gyr, editor, *Structure of Turbulence and Drag Reduction*, pages 23–50, Zurich, 1990. Springer-Verlag Berlin Heidelberg.

[55] A. W. Sherwood. *Aerodynamics*. McGraw-Hill, New York, 1946.

[56] R. J. Barthelmie, S. T. Frandsen, M. N. Nielsen, S. C. Pryor, P. E. Rethore, and H. E. Jørgensen. Modelling and measurements of power losses and turbulence intensity in wind turbine wakes at middelgrunden offshore wind farm. *Wind Energy*, 10(6):517–528, 2007.

[57] R. J. Barthelmie, K. Hansen, S. T. Frandsen, O. Rathmann, J. G. Schepers, W. Schlez, J. Phillips, K. Rados, A. Zervos, E. S. Politis, and P. K. Chaviaropoulos. Modelling and measuring flow and wind turbine wakes in large wind farms offshore. *Wind Energy*, 12(5):431–444, 2009.

[58] J. N. Sørensen. Instability of helical tip vortices in rotor wakes. *Journal of Fluid Mechanics*, 682:1–4, 2011.

[59] S. E. Widnall. The stability of a helical vortex filament. *Journal of Fluid Mechanics*, 54(4):641–663, 1972.

[60] J. Whale, C. G. Anderson, R. Bareiss, and S. Wagner. An experimental and numerical study of the vortex structure in the wake of a wind turbine. *Journal of Wind Engineering and Industrial Aerodynamics*, 84(1):1–21, 2000.

[61] V. L. Okulov and J. N. Sørensen. Instability of helical tip vortices in rotor wakes. *Journal of Fluid Mechanics*, 576:1–25, 2007.

[62] S. Ivanell, R. Mikkelsen, J. N. Sørensen, and D. Henningson. Stability analysis of the tip vortices of a wind turbine. *Wind Energy*, 13:705–715, 2010.

[63] M. Sherry, J. Sheridan, and D. L. Jacono. Characterisation of a horizontal axis wind turbine's tip and root vortices. *Experiments in Fluids*, 54(3), 2013.

[64] S. Sarmast, R. Dadfar, R. F. Mikkelsen, P. Schlatter, S. Ivanell, J. N. Sørensen, and D. S. Henningson. Mutual inductance instability of the tip vortices behind a wind turbine. *Journal of Fluid Mechanics*, 755:705–731, 2014.

[65] A. Nemes, D. Lo Jacono, H. M. Blackburn, and J. Sheridan. Mutual inductance of two helical vortices. *Journal of Fluid Mechanics*, 774:298–310, 2015.

[66] M. M. Hand, D. A. Simms, L. J. Fingersh, D. W. Jager, J. R. Cotrell, S. Schreck, and S. M. Larwood. Unsteady Aerodynamics Experiment Phase VI: Wind Tunnel Test Configurations and Available Data Campaigns. 2001.

[67] D. Simms, S. Schreck, M. Hand, and L. J. Fingersh. NREL Unsteady Aerodynamics Experiment in the NASA-Ames Wind Tunnel : A Comparison of Predictions to Measurements. Technical Report June, 2001.

[68] Q. Wang, H. Zhou, and D. Wan. Numerical simulation of wind turbine blade-tower interaction. *Journal of Marine Science and Application*, 11:321–327, 2012.

[69] Y. Li, K.-J. Paik, T. Xing, and P. M. Carrica. Dynamic overset CFD simulations of wind turbine aerodynamics. *Renewable Energy*, 37:285–298, 2012.

[70] C. E. Lynch and M. J. Smith. Unstructured overset incompressible computational fluid dynamics for unsteady wind turbine simulations. *Wind Energy*, 16:1033–1048, 2013.

[71] M.-C. Hsu, I. Akkerman, and Y. Bazilevs. Finite element simulation of wind turbine aerodynamics: validation study using NREL Phase VI experiment. *Wind Energy*, 17:461–481, 2014.

[72] J. O. Mo, A. Choudhry, M. Arjomandi, and Y. H. Lee. Large eddy simulation of the wind turbine wake characteristics in the numerical wind tunnel model. *Journal of Wind Engineering and Industrial Aerodynamics*, 112:11–24, 2013.

[73] W. Miao, C. Li, G. Pavesi, J. Yang, and X. Xie. Investigation of wake characteristics of a yawed HAWT and its impacts on the inline downstream wind turbine using unsteady CFD. *Journal of Wind Engineering and Industrial Aerodynamics*, 168:60–71, 2017.

[74] M. Draper, A. Guggeri, M. Mendina, G. Usera, and F. Campagnolo. A Large Eddy Simulation-Actuator Line Model framework to simulate a scaled wind energy facility and its application. *Journal of Wind Engineering and Industrial Aerodynamics*, 182:146–159, 2018.

[75] L. P. Chamorro and F. Porté-Agel. Effects of thermal stability and incoming boundary-layer flow characteristics on wind-turbine wakes: A wind-tunnel study. *Boundary-Layer Meteorology*, 136(3):515–533, 2010.

[76] P. Krogstad and P. E. Eriksen. "Blind test" calculations of the performance and wake development for a model wind turbine. *Renewable Energy*, 50:325–333, 2013.

[77] H. Sarlak, T. Nishino, L. A. Martínez-Tossas, C. Meneveau, and J. N. Sørensen. Assessment of blockage effects on the wake characteristics and power of wind turbines. *Renewable Energy*, 93:340–352, 2016.

[78] R. J. A. M. Stevens, L. A. Martínez-Tossas, and C. Meneveau. Comparison of wind farm large eddy simulations using actuator disk and actuator line models with wind tunnel experiments. *Renewable Energy*, 116:470–478, 2018.

[79] M. Felli, R. Camussi, and F. Di Felice. Mechanisms of evolution of the propeller wake in the transition and far fields. *Journal of Fluid Mechanics*, 682:5–53, 2011.

[80] G. V. Iungo, F. Viola, S. Camarri, F. Porté-Agel, and F. Gallaire. Linear stability analysis of wind turbine wakes performed on wind tunnel measurements. *Journal of Fluid Mechanics*, 737:499–526, 2013.

[81] F. Viola, G. V. Iungo, S. Camarri, F. Porté-Agel, and F. Gallaire. Prediction of the hub vortex instability in a wind turbine wake: Stability analysis with eddy-viscosity models calibrated on wind tunnel data. *Journal of Fluid Mechanics*, 750:R1, 2014.

[82] K. B. Howard, A. Singh, F. Sotiropoulos, and M. Guala. On the statistics of wind turbine wake meandering: An experimental investigation. *Physics of Fluids*, 27(7), 2015.

[83] D. Foti, X. Yang, M. Guala, and F. Sotiropoulos. Wake meandering statistics of a model wind turbine: Insights gained by large eddy simulations. *Physical Review Fluids*, 1(4):044407, 2016.

[84] X. Yang and F. Sotiropoulos. A new class of actuator surface models for wind turbines. *Wind Energy*, 21(5):285–302, 2018, arXiv:1006.4405v1.

[85] J. Wang, D. McLean, F. Campagnolo, T. Yu, and C. L. Bottasso. Large-Eddy Simulation of Waked Turbines in a Scaled Wind Farm Facility. *Journal of Physics: Conference Series*, 854(1), 2017.

[86] C. Santoni, K. Carrasquillo, I. Arenas-Navarro, and S. Leonardi. Effect of tower and nacelle on the flow past a wind turbine. *Wind Energy*, 20(12):1927–1939, 2017.

[87] E. G. Duell and A. R. George. Experimental study of a ground vehicle body unsteady near wake. *SAE Transactions*, 108(6):1589–1602, 1999.

[88] S. Krajnović and L. Davidson. Numerical Study of the Flow Around a Bus-Shaped Body. *Journal of Fluids Engineering*, 125(3):500, 2003.

[89] M. Gohlke, J. F. Beaudoin, M. Amielh, and F. Anselmet. Experimental analysis of flow structures and forces on a 3D-bluff-body in constant cross-wind. *Experiments in Fluids*, 43(4):579–594, 2007.

[90] J. Keogh, T. Barber, S. Diasinos, and D. Graham. The aerodynamic effects on a cornering Ahmed body. *Journal of Wind Engineering and Industrial Aerodynamics*, 154:34–46, 2016.

[91] W. C. L. Shih, C. Wang, D. Coles, and A. Roshko. Experiments on flow past rough circular cylinders at large Reynolds numbers. *Journal of Wind Engineering and Industrial Aerodynamics*, 49:351–368, 1993.

[92] L. P. Chamorro and F. Porté-Agel. A wind-tunnel investigation of wind-turbine wakes: Boundary-layer turbulence effects. *Boundary-Layer Meteorology*, 132:129–149, 2009.

[93] J. K. Lundquist, K. K. Duvivier, D. Kaffine, and J. M. Tomaszewski. Costs and consequences of wind turbine wake effects arising from uncoordinated wind energy development. *Nature Energy*, 4(1):26, 2019.

[94] M. Calaf, C. Meneveau, and J. Meyers. Large eddy simulation study of fully developed wind-turbine array boundary layers. *Physics of Fluids*, 22(1):1–16, 2010.

[95] R. B. Cal, J. Lebrón, L. Castillo, H. S. Kang, and C. Meneveau. Experimental study of the horizontally averaged flow structure in a model wind-turbine array boundary layer. *Journal of Renewable and Sustainable Energy*, 2(1):0–25, 2010.

[96] A. Peña and O. Rathmann. Atmospheric stability-dependent infinite wind-farm models and the wake-decay coefficient. *Wind Energy*, 17:1269–1285, 2014.

[97] M. Magnusson and A.-S. Smedman. Influence of atmospheric stability on wind turbine wakes. *Wind Engineering*, 18(3):139–152, 1994.

[98] K. S. Hansen, R. J. Barthelmie, L. E. Jensen, and A. Sommer. The impact of turbulence intensity and atmospheric stability on power deficits due to wind turbine wakes at Horns Rev wind farm. *Wind Energy*, 15:183–196, 2012.

[99] P. Fleming, J. Annoni, A. Scholbrock, E. Quon, S. Dana, S. Schreck, S. Raach, F. Haizmann, and D. Schlipf. Full-Scale Field Test of Wake Steering. *Journal of Physics: Conference Series*, 854(1):012013, 2017.

[100] P. A. Fleming, P. M. O. Gebraad, S. Lee, J. W. van Wingerden, K. Johnson, M. Churchfield, J. Michalakes, P. Spalart, and P. Moriarty. Evaluating techniques for redirecting turbine wakes using SOWFA. *Renewable Energy*, 70:211–218, 2014.

[101] J. Annoni, P. M. O. Gebraad, A. K. Scholbrock, and P. A. Fleming. Analysis of axial-induction-based wind plant control using an engineering and a high-order wind plant model. *Wind Energy*, 19:1135–1150, 2016.

[102] I. Grant, P. Parkin, and X. Wang. Optical vortex tracking studies of a horizontal axis wind turbine in yaw using laser-sheet, flow visualisation. *Experiments in Fluids*, 23:513–519, 1997.

[103] W. Haans, T. Sant, G. van Kuik, and G. van Bussel. Measurement of tip vortex paths in the wake of a HAWT under yawed flow conditions. *Journal of Solar Energy Engineering*, 127(4):456–463, 2005.

[104] I. N. Smalikho, V. A. Banakh, Y. L. Pichugina, W. A. Brewer, R. M. Banta, J. K. Lundquist, and N. D. Kelley. Lidar Investigation of Atmosphere Effect on a Wind Turbine Wake. *Journal of Atmospheric and Oceanic Technology*, 30:2554–2570, 2013.

[105] M. L. Aitken, R. M. Banta, Y. L. Pichugina, and J. K. Lundquist. Quantifying Wind Turbine Wake Characteristics from Scanning Remote Sensor Data. *Journal of Atmospheric and Oceanic Technology*, 31:765–787, 2014.

[106] J. D. Mirocha, D. A. Rajewski, N. Marjanovic, J. K. Lundquist, B. Kosovic, C. Draxl, M. J. Churchfield, and M. J. Churchfield. Investigating wind turbine impacts on near- wake flow using profiling lidar data and large-eddy simulations with an actuator disk model. *Journal of Renewable and Sustainable Energy*, 7:043243, 2015.

[107] E. Machefaux, G. C. Larsen, T. Koblitz, N. Troldborg, M. C. Kelly, A. Chougule, K. S. Hansen, and J. S. Rodrigo. An experimental and numerical study of the

atmospheric stability impact on wind turbine wakes. *Wind Energy*, 19:1785–1805, 2016.

[108] M. Bromm, A. Rott, H. Beck, L. Vollmer, G. Steinfeld, and M. Kuhn. Field investigation on the influence of yaw misalignment on the propagation of wind turbine wakes. *Wind Energy*, 21:1011–1028, 2018.

[109] J. R. Marden, S. D. Ruben, and L. Y. Pao. A Model-Free Approach to Wind Farm Control Using Game Theoretic Methods. *IEEE Transactions on Control Systems Technology*, 21(4):1207–1214, 2013.

[110] P. M. O. Gebraad and J. W. van Wingerden. Maximum power-point tracking control for wind farms. *Wind Energy*, 18(3):429–447, 2014.

[111] J. P. Goit and J. Meyers. Optimal control of energy extraction in wind-farm boundary layers. *Journal of Fluid Mechanics*, 768:5–50, 2015.

[112] W. Munters and J. Meyers. Towards practical dynamic induction control of wind farms: analysis of optimally controlled wind-farm boundary layers and sinusoidal induction control of first-row turbines. *Wind Energy Science*, 3(1):409–425, 2018.

[113] A. E. Yilmaz and J. Meyers. Optimal dynamic induction control of a pair of inline wind turbines. *Physics of Fluids*, 30(8):085106, 2018.

[114] G. C. Larsen, H. A. Madsen, K. Thomsen, and T. J. Larsen. Wake meandering: A pragmatic approach. *Wind Energy*, 11(4):377–395, 2008.

[115] L. Vollmer, G. Steinfeld, D. Heinemann, and M. Kühn. Estimating the wake deflection downstream of a wind turbine in different atmospheric stabilities: an LES study. *Wind Energy Science*, 1(2):129–141, 2016.

[116] J. Trujillo, F. Bingöl, G. C. Larsen, J. Mann, and M. Kühn. Light detection and ranging measurements of wake dynamics. Part II: two-dimensional scanning. *Wind Energy*, 14:61–75, 2011.

[117] T. J. Larsen, H. A. Madsen, G. C. Larsen, and K. S. Hansen. Validation of the dynamic wake meander model for loads and power production in the Egmond aan Zee wind farm. *Wind Energy*, 16:605–624, 2013.

[118] T. Ahmad, A. Basit, M. Ahsan, O. Coupiac, N. Girard, B. Kazemtabrizi, and P. C. Matthews. Implementation and Analyses of Yaw Based Coordinated Control of Wind Farms. *Energies*, 12:1266, 2019.

[119] W. Munters and J. Meyers. Dynamic strategies for yaw and induction control of wind farms based on large-eddy simulation and optimization. *Energies*, 11:177, 2018.

[120] M. F. Howland, S. K. Lele, and J. O. Dabiri. Wind farm power optimization through wake steering. *Proceedings of the National Academy of Sciences*, 116(29):14495–14500, 2019.

[121] J. G. Leishman. Challenges in modelling the unsteady aerodynamics of wind turbines. *Wind Energy*, 5:85–132, 2002.

[122] P. M. O. Gebraad, P. A. Fleming, and J. W. Van Wingerden. Comparison of actuation methods for wake control in wind plants. *Proceedings of the American Control Conference*, 2015-July:1695–1701, 2015.

[123] J. Lebron, L. Castillo, and C. Meneveau. Experimental study of the kinetic energy budget in a wind turbine streamtube. *Journal of Turbulence*, 13:N43, 2012.

[124] N. Hamilton, H. S. Kang, C. Meneveau, and R. B. Cal. Statistical analysis of kinetic energy entrainment in a model wind turbine array boundary layer. *Journal of Renewable and Sustainable Energy*, 4(6):1–20, 2012.

[125] C. Wan, Z. Xu, P. Pinson, Z. Y. Dong, and K. P. Wong. Probabilistic forecasting of wind power generation using extreme learning machine. *IEEE Transactions on Power Systems*, 29(3):1033–1044, 2014.

[126] J. Park and K. H. Law. A data-driven, cooperative wind farm control to maximize the total power production. *Applied Energy*, 165:151–165, 2016.

[127] M. F. Howland and J. O. Dabiri. Wind farm modeling with interpretable physics-informed machine learning. *Energies*, 12(14):2716, 2019.

[128] N. O. Jensen. A note on wind generator interaction - Technical Report Risoe-M-2411(EN). Technical report, Risø National Laboratory, Roskilde, 1983.

[129] M. Bastankhah and F. Porté-Agel. A new analytical model for wind-turbine wakes. *Renewable Energy*, 70:116–123, 2014.

[130] C. R. Shapiro, J. Meyers, C. Meneveau, and D. F. Gayme. Dynamic wake modeling and state estimation for improved model-based receding horizon control of wind farms. *Proceedings of the American Control Conference*, pages 709–716, 2017.

[131] J. Meyers and C. Meneveau. Optimal turbine spacing in fully developed wind farm. *Wind Energy*, 15:305–317, 2012.

[132] C. Meneveau. The top-down model of wind farm boundary layers and its applications. *Journal of Turbulence*, 13:N7, 2012.

[133] V. Santhanagopalan, M. A. Rotea, and G. V. Iungo. Performance optimization of a wind turbine column for different incoming wind turbulence. *Renewable Energy*, 116:232–243, 2018.

[134] R. J. A. M. Stevens and C. Meneveau. Flow structure and turbulence in wind farms. *Annual Review of Fluid Mechanics*, 49:311–339, 2017.

[135] F. Porté-Agel, M. Bastankhah, and S. Shamsoddin. Wind-turbine and wind-farm flows: a review. *Boundary-Layer Meteorology*, 174:1–59, 2018.

[136] W. Yu, V. W. Hong, C. Ferreira, and G. A. M. van Kuik. Experimental analysis on the dynamic wake of an actuator disc undergoing transient loads. *Experiments in Fluids*, 58:149, 2017.

[137] S. Macrí, S. Aubrun, A. Leroy, and N. Girard. Experimental investigation of wind turbine wake and load dynamics during yaw maneuvers. *Wind Energy Science*, 6:585–599, 2021.

[138] J. G. Schepers. IEA Annex XX : Dynamic Inflow effects at fast pitching steps on a wind turbine placed in the NASA-Ames wind tunnel. Technical report, ECN, Petten, 2007.

[139] F. Berger and M. Kühn. Experimental investigation of dynamic inflow effects with a scaled wind turbine in a controlled wind tunnel environment. *Journal of Physics: Conference Series*, 1037:052017, 2018.

[140] A. Ebrahimi and M. Sekandari. Transient response of the flexible blade of horizontal-axis wind turbines in wind gusts and rapid yaw changes. *Energy*, 145:261–275, 2018.

[141] S. J. Andersen and J. N. Sørensen. Instantaneous response and mutual interaction between wind turbine and flow. *Journal of Physics: Conference Series*, 1037:072011, 2018.

[142] W. Munters and J. Meyers. An optimal control framework for dynamic induction control of wind farms and their interaction with the atmospheric boundary layer. *Philosophical Transactions of the Royal Society A*, 375:20160100, 2017.

[143] P. M. O. Gebraad, P. A. Fleming, and J. W. van Wingerden. Wind turbine wake estimation and control using FLORIDyn, a control-oriented dynamic wind plant model. *Proceedings of the American Control Conference*, pages 1702–1708, 2015.

[144] S. Raach, J.-W. van Wingerden, S. Boersma, D. Schlipf, and P. W. Cheng. $\mathscr{H}\infty$ Controller Design for Closed-Loop Wake Redirection. *Proceedings of the American Control Conference*, pages 703–708, 2017.

[145] S. Raach, S. Boersma, B. Doekemeijer, J.-W. van Wingerden, and P. W. Cheng. Lidar-based closed-loop wake redirection in high-fidelity simulation. *Journal of Physics: Conference Series*, 1037:032016, 2018.

[146] P. Fleming, J. King, K. Dykes, and E. et al Simley. Initial results from a field campaign of wake steering applied at a commercial wind farm – part 1. *Wind Energy Science*, 4:273–285, 2019.

[147] M. F. Howland, A. S. Ghate, S. K. Lele, and J. O. Dabiri. Optimal closed-loop wake steering - Part 1: Conventionally neutral atmospheric boundary layer conditions. *Wind Energy Science*, 5:1315–1338, 2020.

[148] S. K. Kanev, F. J. Savenije, and W. P. Engels. Active wake control: An approach to optimize the lifetime operation of wind farms. *Wind Energy*, 21:488–501, 2018.

[149] L. A. Martínez-Tossas, M. J. Churchfield, A. E. Yilmaz, H. Sarlak, P. L. Johnson, J. N. Sørensen, J. Meyers, and C. Meneveau. Comparison of four large-eddy

simulation research codes and effects of model coefficient and inflow turbulence in actuator-line-based wind turbine modeling. *Journal of Renewable and Sustainable Energy*, 10(3):033301, 2018.

[150] C. Tsalicoglou, S. Jafari, N. Chokani, and R. S. Abhari. RANS computations of MEXICO rotor in uniform and yawed inflow. *Journal of Engineering for Gas Turbines and Power*, 136:011202, 2014.

[151] N. Troldborg, F. Zahle, P.-E. Rethore, and N. N. Sørensen. Comparison of wind turbine wake properties in non-sheared inflow predicted by different computational fluid dynamics rotor models. *Wind Energy*, 18:1239–1250, 2015.

[152] M. F. Howland, J. Bossuyt, L. A. Martínez-Tossas, J. Meyers, and C. Meneveau. Wake structure in actuator disk models of wind turbines in yaw under uniform inflow conditions. *Journal of Renewable and Sustainable Energy*, 8:043301, 2016.

[153] Y. Kim, E. Jost, G. Bangga, P. Weihing, and T. Lutz. Effects of ambient turbulence on the near wake of a wind turbine. *Journal of Physics: Conference Series*, 753(3):032047, 2016.

[154] H. Rahimi, J. G. Schepers, W. Z. Shen, N. Ramos García, M. S. Schneider, D. Micallef, C. J. Simao Ferreira, E. Jost, L. Klein, and I. Herráez. Evaluation of different methods for determining the angle of attack on wind turbine blades with CFD results under axial inflow conditions. *Renewable Energy*, 125:866–876, 2018.

[155] M. L. Blaylock, B. C. Houchens, D. C. Maniaci, T. Herges, A. Hsieh, R. C. Knaus, and P. Sakievich. Comparison of field measurements and large eddy simulations of the scaled wind farm technology (SWiFT) site. *Proceedings of the ASME-JSME-KSME 2019 Joint Fluids Engineering Conference*, 59070:V004T04A012, 2019.

[156] J. Nielson and K. Bhaganagar. Using field data–based large eddy simulation to understand role of atmospheric stability on energy production of wind turbines. *Wind Energy*, 43(6):625–638, 2019.

[157] J. N. Sørensen and W. Z. Shen. Numerical modeling of wind turbine wakes. *Journal of Fluids Engineering*, 124:393–399, 2002.

[158] L. A. Martínez-Tossas, M. J. Churchfield, and S. Leonardi. Large eddy simulations of the flow past wind turbines: actuator line and disk modeling. *Wind Energy*, 18:1047–1060, 2014.

[159] L. A. Martínez-Tossas. *Large Eddy Simulations and Theoretical Analysis of Wind Turbine Aerodynamics Using an Actuator Line Model*. Phd, Johns Hopkins University, 2017.

[160] B. Sanderse, S. P. van der Pijl, and B. Koren. Review of computational fluid dynamics for wind turbine wake aerodynamics. *Wind Energy*, 14:799–819, 2011.

[161] H. Lu and F. Porté-Agel. Large-eddy simulation of a very large wind farm in a stable atmospheric boundary layer. *Physics of Fluids*, 23:065101, 2011.

[162] E. W. Quon, P. Doubrawa, and M. Debnath. Comparison of rotor wake identification and characterization methods for the analysis of wake dynamics and evolution. *Journal of Physics: Conference Series*, 1452:012070, 2020.

[163] T. Ishihara and G. W. Qian. A new Gaussian-based analytical wake model for wind turbines considering ambient turbulence intensities and thrust coefficient effects. *Journal of Wind Engineering and Industrial Aerodynamics*, 177:275–292, 2018.

[164] A. Keane, P. E. O. Aguirre, H. Ferchland, P. Clive, and D. Gallacher. An analytical model for a full wind turbine wake. *Journal of Physics: Conference Series*, 753(3):032039, 2016.

[165] M. Cathelain, F. Blondel, P. A. Joulin, and P. Bozonnet. Calibration of a super-Gaussian wake model with a focus on near-wake characteristics. *Journal of Physics: Conference Series*, 1618:062008, 2020.

[166] P. Doubrawa, R. J. Barthelmie, H. Wang, and M. J. Churchfield. A stochastic wind turbine wake model based on new metrics for wake characterization. *Wind Energy*, 20:449–463, 2017.

[167] M. Bastankhah and F. Porté-Agel. Experimental and theoretical study of wind turbine wakes in yawed conditions. *Journal of Fluid Mechanics*, 806:506–541, 2016.

[168] C. R. Shapiro, D. F. Gayme, and C. Meneveau. Modelling yawed wind turbine wakes: A lifting line approach. *Journal of Fluid Mechanics*, 841:R1, 2018.

[169] L. A. Martínez-Tossas, J. Annoni, P. A. Fleming, and M. J. Churchfield. The aerodynamics of the curled wake: a simplified model in view of flow control. *Wind Energy Science*, 4:127–138, 2019.

[170] H. Zong and F. Porté-Agel. A point vortex transportation model for yawed wind turbine wakes. *Journal of Fluid Mechanics*, 890:A8, 2020.

[171] T. Leweke, S. Le Dizès, and C. H. K. Williamson. Dynamics and instabilities of vortex pairs. *Annual Review of Fluid Mechanics*, 48:507–541, 2016.

[172] E. Kleusberg, P. Schlatter, and D. S. Henningson. Parametric dependencies of the yawed wind-turbine wake development. *Wind Energy*, 23(6):1367–1380, 2020.

[173] J. Frederik, R. Weber, S. Cacciola, F. Campagnolo, A. Croce, C. Bottasso, and J.-W. van Wingerden. Periodic dynamic induction control of wind farms: proving the potential in simulations and wind tunnel experiments. *Wind Energy Science*, 5:245–257, 2020.

[174] L. Zhan, S. Letizia, and G. V. Iungo. LiDAR measurements for an onshore wind farm: Wake variability for different incoming wind speeds and atmospheric stability regimes. *Wind Energy*, 23:501–527, 2020.

[175] K. Brown, D. Houck, D. Maniaci, and C. Westergaard. Rapidly recovering wind turbine wakes with dynamic pitch and rotor speed control. *AIAA Scitech 2021 Forum*, page 1182, 2021.

[176] J. M. Ortega, R. L. Bristol, and Ö. Savaş. Experimental study of the instability of unequal-strength counter-rotating vortex pairs. *Journal of Fluid Mechanics*, 474:35–84, 2003.

[177] X. Yang and F. Sotiropoulos. A review on the meandering of wind turbine wakes. *Energies*, 12(24):4725, 2019.

[178] S. Rockel, E. Camp, J. Schmidt, J. Peinke, R. B. Cal, and M. Hölling. Experimental study on influence of pitch motion on the wake of a floating wind turbine model. *Energies*, 7(4):1954–1985, 2014.

[179] J. Annoni, A. Scholbrock, M. Churchfield, and P. Fleming. Evaluating tilt for wind plants. *Proceedings of the American Control Conference*, pages 717–722, 2017.

[180] K. Su and D. Bliss. A numerical study of tilt-based wake steering using a hybrid free-wake method. *Wind Energy*, 23(2):258–273, 2020.

[181] J. Bossuyt, R. Scott, N. Ali, and R. B. Cal. Quantification of wake shape modulation and deflection for tilt and yaw misaligned wind turbines. *Journal of Fluid Mechanics*, 917:A3, 2021.

[182] A. Abraham, L. A. Martínez-Tossas, and J. Hong. The effect of dynamic near-wake modulation on utility-scale wind turbine wake development. *Journal of Physics: Conference Series*, 1618:062063, 2020.

[183] M. Khalid and A. V. Savkin. A method for short-term wind power prediction with multiple observation points. *IEEE Transactions on Power Systems*, 27(2):579–586, 2012.

[184] A. Clifton, A. Smith, and M. Fields. Wind Plant Preconstruction Energy Estimates. Current Practice and Opportunities. Technical report, National Renewable Energy Laboratory, Golden, CO, 2016.

[185] J. Jonkman, J. Annoni, G. Hayman, B. Jonkman, and A. Purkayastha. Development of FAST.Farm: A new multiphysics engineering tool for wind farm design and analysis. In *AIAA SciTech Forum: Wind Energy Symposium*, page 0454, 2017.

[186] J. Jonkman and K. Shaler. FAST.Farm User's Guide and Theory Manual. Technical Report April, National Renewable Energy Laboratory, Golden, CO, 2021.

[187] J. F. Ainslie. Calculating the flowfield in the wake of wind turbines. *Journal of Wind Engineering*, 27:213–224, 1988.

[188] P. Doubrawa, J. Annoni, J. Jonkman, and A. Ghate. Optimization-based calibration of FAST.Farm parameters against SOWFA. In *AIAA SciTech Forum: Wind Energy Symposium*, page 0512, 2018.

[189] K. Shaler, M. Debnath, and J. Jonkman. Validation of FAST.Farm against Full-Scale Turbine SCADA Data for a Small Wind Farm. *Journal of Physics: Conference Series*, 1618:062061, 2020.

[190] J. Jonkman, P. Doubrawa, N. Hamilton, J. Annoni, and P. Fleming. Validation of FAST . Farm Against Large-Eddy Simulations. *Journal of Physics: Conference Series*, 1037:062005, 2018.

[191] D. A. Rajewski, E. S. Takle, J. K. Lundquist, S. Oncley, J. H. Prueger, T. W. Horst, M. E. Rhodes, R. Pfeiffer, J. L. Hatfield, K. K. Spoth, and R. K. Doorenbos. Crop Wind Energy Experiment (CWEX): Observations of surface-layer, boundary layer, and mesoscale interactions with a wind farm. *Bulletin of the American Meteorological Society*, 94(5):655–672, 2013.

[192] K. Xu, L. He, H. Hu, S. Liu, Y. Du, Z. Wang, Y. Li, L. Li, A. Khan, and G. Wang. Positive ecological effects of wind farms on vegetation in China's Gobi desert. *Scientific Reports*, 9(1):6341, 2019.

[193] S. A. Abbasi and N. Abbasi. The likely adverse environmental impacts of renewable energy sources. *Applied Energy*, 65(1-4):121–144, 2000.

[194] E. D. Christensen, M. Johnson, O. R. Sørensen, C. B. Hasager, M. Badger, and S. E. Larsen. Transmission of wave energy through an offshore wind turbine farm. *Coastal Engineering*, 82:25–46, 2013.

[195] W. Zhang, C. D. Markfort, and F. Porté-Agel. Wind-turbine wakes in a convective boundary layer: A wind-tunnel study. *Boundary-Layer Meteorology*, 146(2):161–179, 2013.

[196] C. M. Smith, R. J. Barthelmie, and S. C. Pryor. In situ observations of the influence of a large onshore wind farm on near-surface temperature, turbulence intensity and wind speed profiles. *Environmental Research Letters*, 8:034006, 2013.

[197] C. L. Archer, S. Wu, A. Vasel-Be-Hagh, J. F. Brodie, R. Delgado, A. St. Pé, S. Oncley, and S. Semmer. The VERTEX field campaign: observations of near-ground effects of wind turbine wakes. *Journal of Turbulence*, 20(1):64–92, 2019.

[198] S. Baidya Roy and J. J. Traiteur. Impacts of wind farms on surface air temperatures. *Proceedings of the National Academy of Sciences*, 107(42):17899–17904, 2010.

[199] L. Zhou, Y. Tian, S. Baidya Roy, C. Thorncroft, L. F. Bosart, and Y. Hu. Impacts of wind farms on land surface temperature. *Nature Climate Change*, 2:539–543, 2012.

[200] S. Baidya Roy, S. W. Pacala, and R. L. Walko. Can large wind farms affect local meteorology? *Journal of Geophysical Research D: Atmospheres*, 109:D19101, 2004.

[201] Y. Li, E. Kalnay, S. Motesharrei, J. Rivas, F. Kucharski, D. Kirk-Davidoff, E. Bach, and N. Zeng. Climate model shows large-scale wind and solar farms in the Sahara increase rain and vegetation. *Science*, 361(6406):1019–1022, 2018.

[202] L. M. Miller and D. W. Keith. Climatic Impacts of Wind Power. *Joule*, 2:1–15, 2018.

[203] G. Xia, L. Zhou, J. R. Minder, R. G. Fovell, and P. A. Jimenez. Simulating impacts of real-world wind farms on land surface temperature using the WRF model: physical mechanisms. *Climate Dynamics*, 53:1723–1739, 2019.

[204] K. D. Squires and J. K. Eaton. Preferential concentration of particles by turbulence. *Physics of Fluids A*, 3(5):1169–1178, 1991.

[205] M. Abkar and F. Porté-Agel. Influence of atmospheric stability on wind-turbine wakes: A large-eddy simulation study. *Physics of Fluids*, 27:035104, 2015.

[206] S. Baidya Roy. Simulating impacts of wind farms on local hydrometeorology. *Journal of Wind Engineering and Industrial Aerodynamics*, 99(4):491–498, 2011.

[207] D. W. Keith, J. F. DeCarolis, D. C. Denkenberger, D. H. Lenschow, S. L. Malyshev, S. Pacala, and P. J. Rasch. The influence of large-scale wind power on global climate. *Proceedings of the National Academy of Sciences*, 101(46):16115–16120, 2004.

[208] J. H. IV Lienhard and J. H. V Lienhard. *A Heat Transfer Textbook*. Phlogiston Press, Cambridge, Massachusetts, fifth edit edition, 2020.

[209] C. Draxl, A. Clifton, B. M. Hodge, and J. McCaa. The Wind Integration National Dataset (WIND) Toolkit. *Applied Energy*, 151:355–366, 2015.

[210] V. Kumar, J. Kleissl, C. Meneveau, and M. B. Parlange. Large-eddy simulation of a diurnal cycle of the atmospheric boundary layer: Atmospheric stability and scaling issues. *Water Resources Research*, 42:W06D09, 2006.

[211] J. Sakurai-Ishikawa, M. Murai-Hatano, H. Hayashi, A. Ahamed, K. Fukushi, T. Matsumoto, and Y. Kitagawa. Transpiration from shoots triggers diurnal changes in root aquaporin expression. *Plant, Cell and Environment*, 34(7):1150–1163, 2011.

[212] J. Siecker, K. Kusakana, and B. P. Numbi. A review of solar photovoltaic systems cooling technologies. *Renewable and Sustainable Energy Reviews*, 79:192–203, 2017.

[213] C. Wang and R. G. Prinn. Potential climatic impacts and reliability of very large-scale wind farms. *Atmospheric Chemistry and Physics*, 10(4):2053–2061, 2010.

[214] A. C. Fitch. Climate impacts of large-scale wind farms as parameterized in a global climate model. *Journal of Climate*, 28(15):6160–6180, 2015.

[215] B. Wieneke. Stereo-PIV using self-calibration on particle images. *Experiments in Fluids*, 39:267–280, 2005.

[216] D. Ossmann, P. Seiler, C. Milliren, and A. Danker. Field testing of multivariable individual pitch control on a utility-scale wind turbine. *Renewable Energy*, 170:1245–1256, 2021.

[217] R. J. Moffat. Describing the uncertainties in experimental results. *Experimental Thermal and Fluid Science*, 1(1):3–17, 1988.

Appendix A

Dynamic wake modulation appendices

A.1 Void extraction from images

Several image processing steps were applied to the raw images to extract the voids that indicate vortices in the flow, shown in figure 5.2(b) and in more detail focusing on the top tip vortices in figure A.1. First, the images were detilted to correct for distortion caused by the inclination angle of the camera using the process described in Dasari et al. [5]. A 500-frame moving average intensity image was calculated and subtracted from each image in the sequence. Histogram equalization was applied to enhance the contrast, and a 1.5-pixel median filter was applied to reduce noise (figure A.1b). The region outside of the light sheet was masked out. The images were then denoised using total variation denoising (figure A.1c). The images were binarized using a threshold calculated based on the average intensity of the image sequence (figure A.1d). The blades were removed from the non-thresholded images using a mask generated by averaging images that were highly correlated in the region of the blades. Median filter smoothing (figure A.1e) and Canny edge detection (figure A.1f) were also applied to the non-thresholded images. Binary regions that contained edges detected by the Canny filter were kept as snowflake voids caused by blade tip vortices in the wake, while ones that did not were removed as noise (figure A.1g and h). As the last step, the snow voids induced by blade tip vortices were extracted from the binary image based on their characteristic size,

eccentricity, orientation, and location in the image. These parameters differentiated the tip vortex induced voids from the snow voids caused by other vortices in the near wake (e.g., vortices shed from the turbine hub) and in the ambient atmospheric flow passing through the wake.

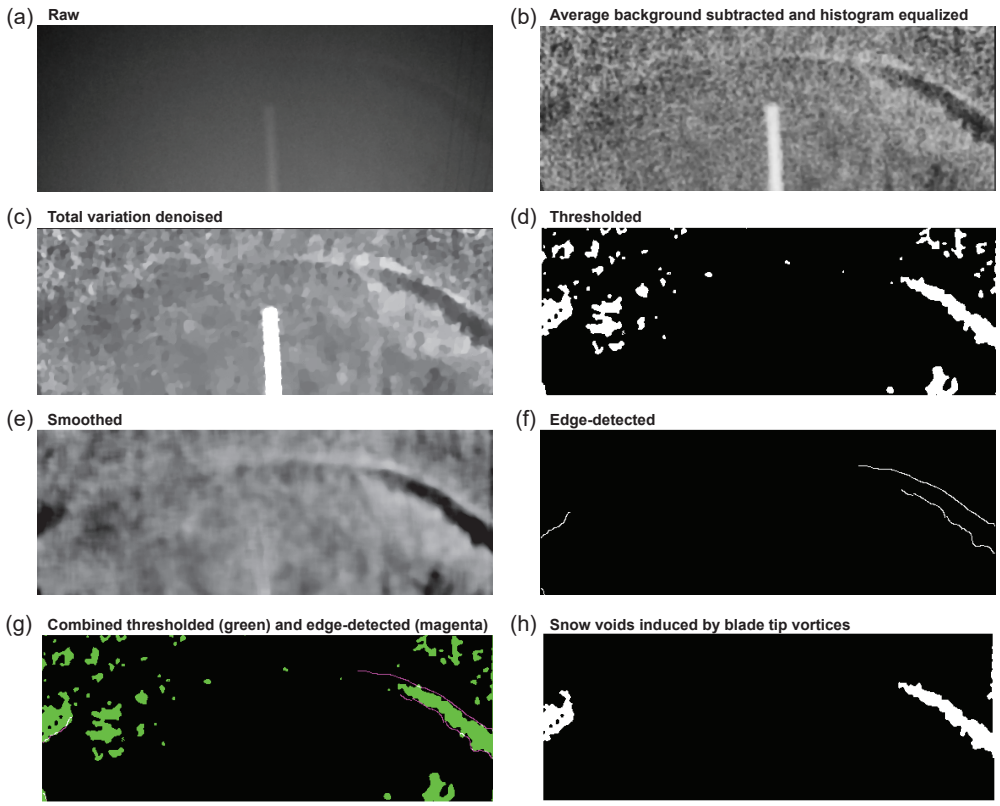

Figure A.1: (a) Raw image cropped to above hub height region. (b) Enhanced image after background subtraction, histogram equalization, and median filtering. (c) Total variation denoised image. (d) Threshold applied to image (c). (e) Blade removed and three-dimensional median filter applied to image (b). (f) Canny edge detection applied to image (d). (g) Images (e) in green and (f) in magenta, combined. (h) Regions of overlap between (e) and (f) preserved.

A.2 Wake envelope extraction

The blade tip vortices extracted from the images define the wake envelope that was used to calculate the wake deflection. The topmost tip vortex edge was detected and outliers more than three scaled median absolute deviations from the median were removed. The envelope was interpolated to a grid and smoothed using a mean filter of 20 s. This smoothing period was determined by dividing the characteristic length scale, D, by the minimum wake velocity to remove any fluctuations that were too small to accurately reflect changes in the whole wake. Each cross-section of the envelope was compared to the wake cross-section extracted from the SolidWorks model of the experimental setup. In the model, the cross-section was obtained by approximating the wake as a uniform cylinder emanating from the rotor and intersecting the light sheet. The cross-section changed when nacelle direction changed, but no changes in atmospheric conditions or the resulting expansion and deflection were accounted for in the model. Because the model cross-section is a cylinder intersecting a plane, it is elliptical by definition. The equation of the ellipse was obtained and the shift that provided the best nonlinear least squares fit to the ellipse was applied to the experimental wake cross-section. The components of the shift of this cross-section define the vertical and spanwise wake shifts $\delta_{w,z}$ and $\delta_{w,y}$.

A.3 Energy flux calculation and uncertainty quantification

The energy flux is calculated using the fluctuating velocities of the top and sides of the wake. The wake velocities are calculated by taking the temporal derivative of the wake deflection in the vertical and spanwise directions,

$$v_{w,z} = d\delta_{w,z}/dt, v_{w,y} = d\delta_{w,y}/dt. \tag{A.1}$$

The primary source of uncertainty in v_w is due to the image calibration, determined by the distance between the camera and the light sheet and the inclination angle of the camera. Uncertainty in the distance estimation is about 5 m (3%) and uncertainty in the inclination angle is about 0.5 degrees (2%), yielding a total uncertainty of 4% for each v_w component when combined using the root-sum-squared method [217].

These velocities are multiplied by the fluctuating component of the streamwise freestream velocity obtained from the speed recorded by the SCADA system. Note that the wind speed recorded at the hub is an approximation of the freestream, as it is within the induction zone of the rotor. However, because the flow data from the SCADA is available to turbine controllers, this data is used for our analysis. To account for the uncertainty caused by the induction zone, we refer to a recent study of the accuracy of the sonic anemometer at the turbine nacelle relative to the true incoming flow velocity conducted at the Eolos site [45]. This study shows the average velocity recorded at the nacelle is 0.94 times the true incoming velocity, with a standard deviation of 0.06. These values indicate the worst-case-scenario error caused by the induction effect is 12%. Additionally, note that the flux approximated in the current study underestimates the flux by using velocity data from within the induction zone. To account for the uncertainty caused by the height of the anemometer (at hub height rather than the wake interface), we use a log-law approximation of the incoming boundary layer flow:

$$u_x(z) = \frac{u_*}{\kappa} \ln\left(\frac{z}{z_0}\right). \tag{A.2}$$

Based on Dasari et al. [5], the surface roughness at the Eolos site is $z_0 = 0.53$ m. Using the mean velocity at hub height ($u(z = 80m) = 9.6$ m/s), the friction velocity can be calculated to be $u_* = 0.78$ m/s. This enables the calculation of the velocity at the top wake interface as $u(z = 130m) = 10.5$ m/s, which gives an uncertainty of 0.9 m/s or 9%. This value is combined with the 12% caused by the induction effect to yield a total uncertainty of 15% for u_x at the top wake interface. Again, note that this uncertainty leads to an underestimate of the calculated flux.

The wind speed is decomposed into streamwise and spanwise components (u_x and u_y, respectively) using the nacelle direction. A moving average streamwise velocity, $\overline{u}_x$, is calculated using a 30-minute window to account for changes in the atmospheric conditions. The fluctuating component is obtained by subtracting the moving average,

$$u'_x = u_x - \overline{u}_x. \tag{A.3}$$

The Reynolds shear stress caused by wake deformation is then defined as $\overline{u'_x v'_{w,z}}$ on the top surface and $\overline{u'_x v'_{w,y}}$ on the side surfaces. These Reynolds stresses contribute a

flux per unit area of

$$\Phi = \overline{u}_x \overline{u'_x v'_w} \tag{A.4}$$

on each surface, where the $\overline{u}_x$ values representing freestream velocity are taken from the SCADA and the $\overline{u}_x$ values representing the wake velocity are taken from the met tower (which stays within the turbine wake throughout the experiment). Combining the uncertainties of u_x and v_w, the total uncertainty of Φ is 16%. The maximum added flux due to dynamic wake modulation is still outside of this upper error margin, though based on the above analysis, the flux is likely larger than the value estimated in the current study.

A.4 Wake width definition

The need for the selection of the 91% confidence interval to define the wake width in the near wake rather than the 95% interval typically used for the far wake becomes clear by looking closely at the Gaussian fit for a sample timestep. In the near wake, the velocity deficit drops more sharply at the wake edges than the Gaussian function. A cross-section of the wake velocity profile and Gaussian fit at hub height is shown in figure A.2(a), along with lines indicating the location of the 95% confidence interval (1.96σ) and the 91% confidence interval (1.7σ). The 95% interval intersects the velocity profile outside of the region of the velocity deficit that defines the wake. On the other hand, the 91% interval intersects the velocity profile at the point of maximum velocity gradient, which demarcates the wake boundary. The specific value of 91% was selected by finding the point of maximum velocity gradient at multiple timesteps. The need for the shift in definition of the wake boundary is further clarified in figure A.2(b), which shows the near wake velocity cross-section with both confidence intervals superimposed. The outer is the 95% interval, which clearly overshoots the wake boundary, while the inner circle (91% interval) captures the wake edge much more accurately.

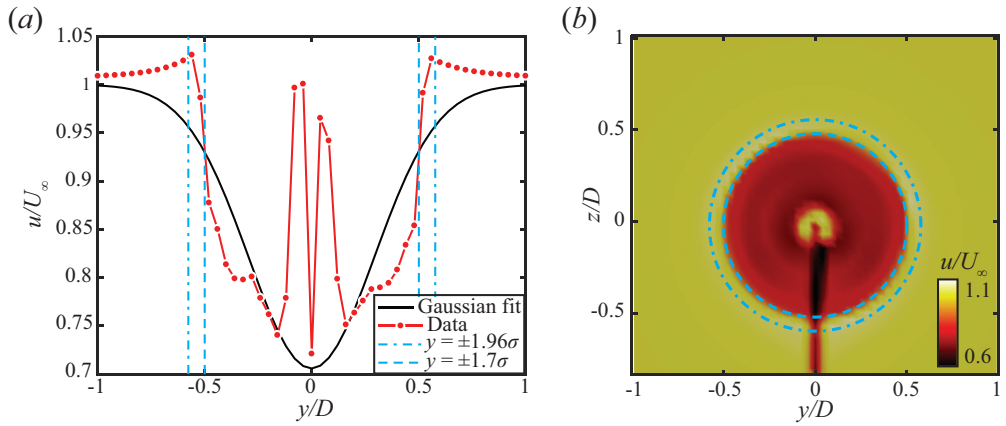

Figure A.2: (a) Cross-section at hub height of the wake velocity field for a sample simulation time step compared to the corresponding Gaussian fit. Note that the sharp velocity peaks in the middle are characteristic of flow acceleration around the turbine nacelle. The width of the 95% ($y = \pm 1.96\sigma$) and 91% ($y = \pm 1.7\sigma$) confidence intervals are also indicated as vertical lines. (b) Wake velocity field with 95% (dot-dashed circle) and 91% (dashed circle) confidence intervals superimposed.